Studying Biomolecular Structures and Their Interaction Using Atomic Force Microscopy

by

Subhadip Senapati

A Dissertation Presented in Partial Fulfillment
of the Requirements for the Degree
Doctor of Philosophy

Approved January 2015 by the
Graduate Supervisory Committee:

Stuart Lindsay, Co-Chair
Peiming Zhang, Co-Chair
Giovanna Ghirlanda
Ian Gould

ARIZONA STATE UNIVERSITY

May 2015

ABSTRACT

Atomic force microscopy (AFM) has become an important tool to characterize and image surfaces with nanoscale resolution. AFM imaging technique has been utilized to study a wide range of substances such as DNA, proteins, cells, silicon surfaces, nanowires etc. Hence AFM has become extremely important in the field of biochemistry, cell biology and material science. Functionalizing the AFM tip made it possible to detect molecules and their interaction using recognition imaging at single molecule level. Also the unbinding force of two molecules can be investigated based on AFM based single molecule force spectroscopy.

In the first study, a new chemical approach to functionalize the AFM tip in a simple and user-friendly way has been described. Copper-free click chemistry and a vinyl sulfone PEG linker have been utilized during the process. Using this technique, human α-thrombin and $\alpha_5\beta_1$-integrin were detected in separate experiments. Then a novel tri-arm linker with two recognition molecules on it was designed and two proteins (human α-thrombin and $\alpha_5\beta_1$-integrin) were detected simultaneously in the same experiment using recognition imaging. This technique can be applied to understand many multivalent interactions taking place in nature. Using the same tri-arm linker functionalized with two biotin molecules, the interaction of streptavidin with mono-biotin and bis-biotin ligands were investigated. The thermal stability of streptavidin-biotin complex was also studied using SDS-PAGE analysis.

In the final study, structure of native chromatin extracted from normal and cancer cell lines were analyzed using AFM imaging and agarose gel electrophoresis. Different salt fractions were used to extract chromatin region depending on their solubility. Mnase

sensitivity of the chromatin sample was used to understand the open and closed structures of chromatin from different sources. The amount of chromatin in different salt fractions could act as an indicator of amount of open and condensed chromatin in normal and cancer cells. Eventually this ratio of closed and open structure of chromatin could be an indicator of tumorigenic nature of particular cell lines.

DEDICATION

To my family

ACKNOWLEDGMENTS

I am deeply grateful to my mentors, Dr. Stuart Lindsay and Dr. Peiming Zhang for their constant guidance, encouragement and support. Thank you for your help and support during last few years and I sincerely appreciate that. I would like to thank my collaborators Dr. Robert Ros, Dr. Joshua LaBaer and Dr. Craig Peterson. I would like to thank my committee member Dr. Giovanna Ghirlanda and Dr. Ian Gould.

Next, I would like to thank Dr. Parminder Kaur. She not only taught me how to use the AFM and helped me during her time in the lab, but also answered all my stupid questions even after her graduation.

I would like to thank Brendan Sullivan. You have contributed more to the chromatin project than I could have ever asked for. You spent an incredible amount of time in this project with me despite being busy with your undergraduate courses, exams and other projects. Thanks a lot for working so hard.

I would also like to thank Anli Tang for helping us with the chromatin project during its initial days. I would also like to thank all other undergraduates who worked with me. Thank you Linsy Townsend, Jason Hanna, Cuong Nguyen.

I would also like to thank all my fellow labmates in Lindsay lab. Saikat Manna and Sudipta Biswas were integral part of my projects. Thank you for your hard work behind the synthesis of so many organic compounds. I would also like to thank Suman Sen, Sovan Biswas, Weisi Song, Brian Ashcroft for all your helps and suggestions. I would also like to thank all other lab mates.

My special thanks to Mike Dodson for helping me out with all the orders and helping me out with so many instruments. I also thank Margaret Black for her help with everything I needed.

I would like to thank Suratna, Palash, Anirban and Anasuya for all their help with my biochemistry and experiments. I would also thank Souvagya, Aritra, Sumit and Sriloy for all their help, support and suggestions.

Finally and most importantly I would like to thank my parents, brother and sister. Without your support I wouldn't be here. Thank you for everything.

TABLE OF CONTENTS

Page

CHAPTER Page

CHAPTER Page

CHAPTER Page

LIST OF TABLES

LIST OF FIGURES

Figure Page

CHAPTER 1

INTRODUCTION

Atomic Force Microscopy (AFM) is one of the most powerful techniques for single molecular study to investigate properties of a surface with nanoscale resolution (1–3). It is a type of scanning probe microscopy (SPM) that uses the interaction of the probe and the surface to produce an image of the surface. Scanning tunneling microscopy (STM), the earlier version of SPM was developed in 1981 by Gerd Binnig and Heinrich Rohrer, at the IBM, Zurich, winning them Nobel Prize in Physics in 1986 (4). But since, STM could image only conducting substances, the improved and advanced version AFM was developed by Gerd Bining and the experimental demonstration was published (5). The first commercial AFM was introduced three years later, 1989. Later, it was possible to image the surface using tapping mode and then in aqueous solution (6,7). Because of these two advancements, AFM became a very popular tool for studying biomolecules. In contact mode AFM, because of the physical contact, there was a finite possibility of damaging the biomolecules being studied. Also, physiological conditions play a critical part in evaluating the activities of biomolecules and AFM made it possible to study biomolecules in physiological condition. AFM force spectroscopy enabled us to determine the unbinding force of different systems, ligand-receptor, antigen-antibody, aptamer-protein, organic molecule-protein etc (8–10). Finally, the invention of TREC (simultaneous topography and recognition imaging) added an entirely new dimension to the AFM world. Using TREC, it has become possible to detect and map specific interactions at the nanoscale level (11–14).

We were interested in the structure and epigenetic modifications of chromatin in normal and cancer cells. Using AFM recognition imaging technique, we wanted to investigate multiple modifications in chromatin (DNA methylation, histone acetylation or other histone variants) in both cell types. So, first we designed a tri-arm linker and applied it to detect two proteins simultaneously. Our goal remains to use this technique to understand the relation between chromatin modification and cancer.

This thesis focuses on the structure and activity analysis of different biomolecular systems (DNA aptamer-protein, peptide-protein, chromatin) using AFM imaging, force spectroscopy and recognition imaging. It includes the following projects:

1. Development an alternative route to AFM tip modification using copper-free click chemistry
2. Detection of two proteins simultaneously using a tri-arm linker
3. Understanding the structures of chromatin extracted from normal and cancer cell lines

1.1. Chromatin structure and cancer

1.1.1 Gene, chromosome and chromatin

The gene is the molecular unit that carries heredity information in the cells. Chromosome is the structure made of nucleic acids and protein found in the nucleus of most living cells, carrying the genes. The DNA double helix is packaged by octameric histone proteins to form a condensed complex called chromatin. The chromatin further condenses to form the chromosome (15–19). These are present in all eukaryotic cells (yeast to human).

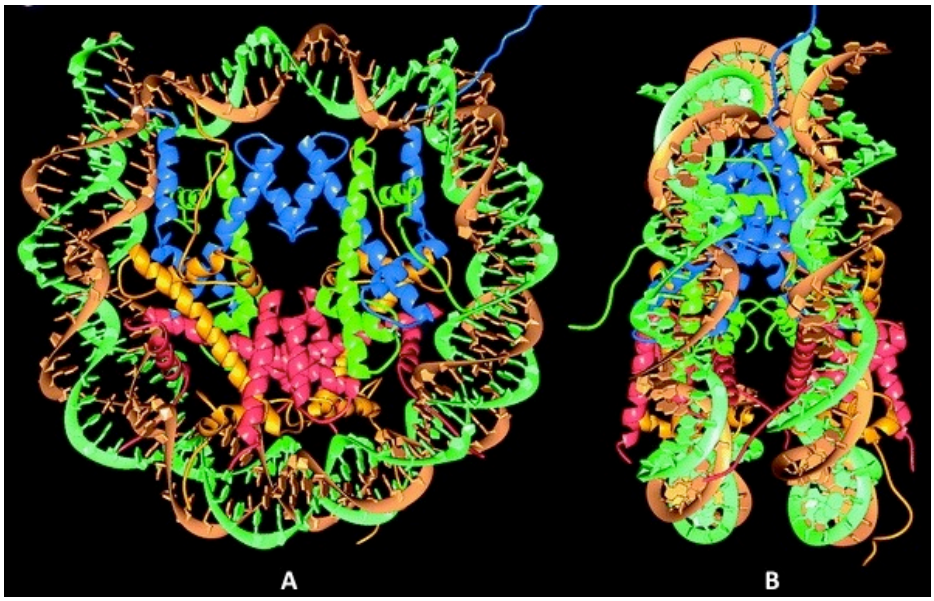

Figure 1. A) Crystal structure of nucleosomal unit consisting of H2A, H2B, H3, H4 and DNA wrapped around (along the DNA helix), B) same (perpendicular view). Adapted from reference (20)

The Nucleosome is the repeating unit in chromosome made up of DNA wrapped around the histones (Figure 1). Histone is an octameric protein that consists of eight subunits, two H2A and H2B dimer and a H3-H4 tetramer. H2A, H2B, H3 and H4 are known as core histones whereas H1 and H5 are known as linker histones (21,22). Nucleosomes help to manage the enormous length of the DNA and arrange it into a closely packed structure. For example, DNA wound on histones is about few μm but without histones, it would have been 2 meter of DNA (23).

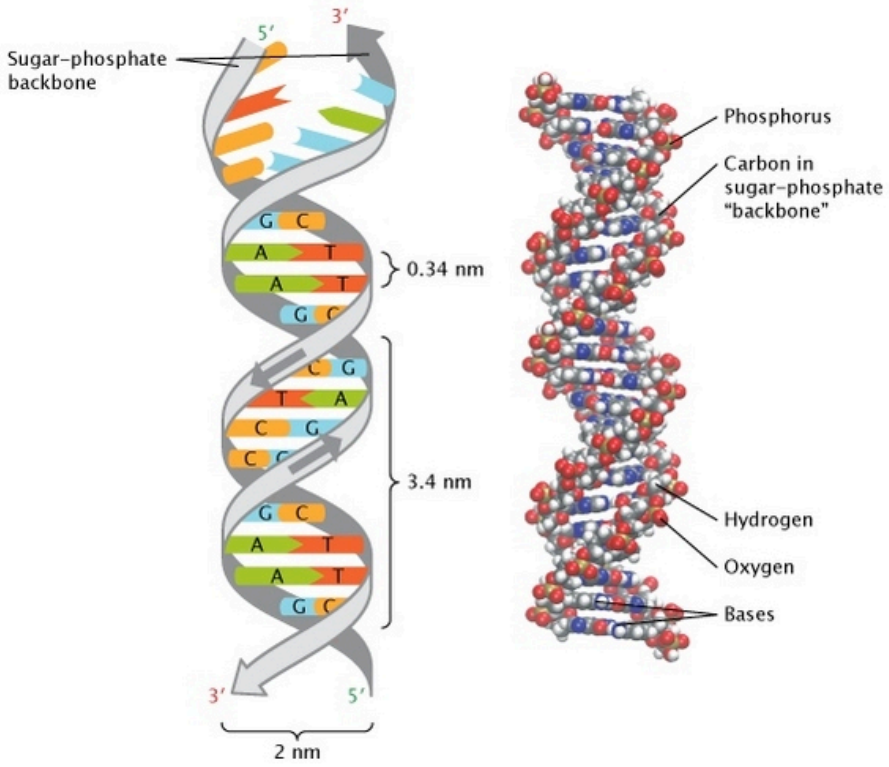

Figure 2. DNA double helical structure showing A-T and G-C base pair interaction. Adapted from reference (24)

The DNA is double stranded DNA (dsDNA) consisting of two helices where specific base pairs interact with each other. Adenine (A) forms a base pair with thymine (T) and guanine (G) forms a base pair with cytosine (C) (Figure 2) (24,25). The diameter of histone particle is about 65 Å and the DNA wrapped around this histone octamer 1.65 times in a left-handed super helical turn makes the diameter ~100Å. The entry and exit site of the DNA in the nucleosomes are connected by the linker histone H1 and the nucleosomes are connected with each other by short DNA called linker DNA (26,27). The nucleosomes connected with the linker DNA forms the nucleosomal arrays which condense to form the chromatin fibre and subsequently the chromosome.

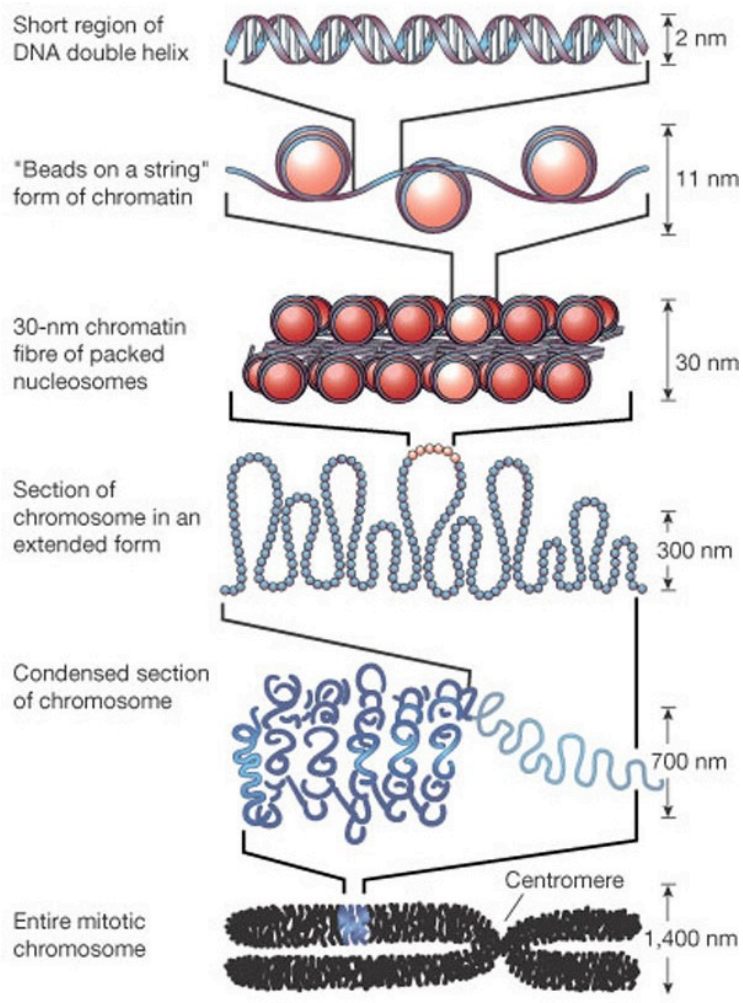

Figure 3. Structural units forming the chromosome inside the cell and their dimensions. Width of the dsDNA is abot ~2 nm. The dimension of beads-on-a-string structure and compact structures are ~11 nm and ~30 nm respectively. Adapted from reference (28)

Chromatin can be classified into two forms, euchromatin and heterochromatin. Euchromatin is the loosely arranged structure that consists of the active region of the gene that takes part in transcription. Because the nucleosomes are loosely connected with the DNA, it appears as 'beads-on-a-string' like structure. The heterochromatin is more densely packed form that provides the integrity to the chromosome structure (29–31). Heterochromatin can be classified into two categories: constitutive and facultative.

Based on the structure and dimension, the more loosely bound chromosome is called the '10 nm' structure and the condensed form is called the '30 nm'-structure (Figure 3). Even though the existence of the 30 nm structure is well known *in vitro*, its existence *in vivo* was seriously challenged in some recent studies (32–34).

Figure 4 shows the beads-on-a-string structure (A) and the condensed structures (B) of chromatin. The vast majority of DNA (>70%) in a cell is packaged into nucleosomes. X-ray diffraction studies showed chromatin was organized into highly compacted structure (30 nm structure, figure 4. B). But, some studies suggest that majority of the chromatin is packaged into a beads-on-string like structure with some folded areas exhibiting some cross-array structures (figure 4. C and D).

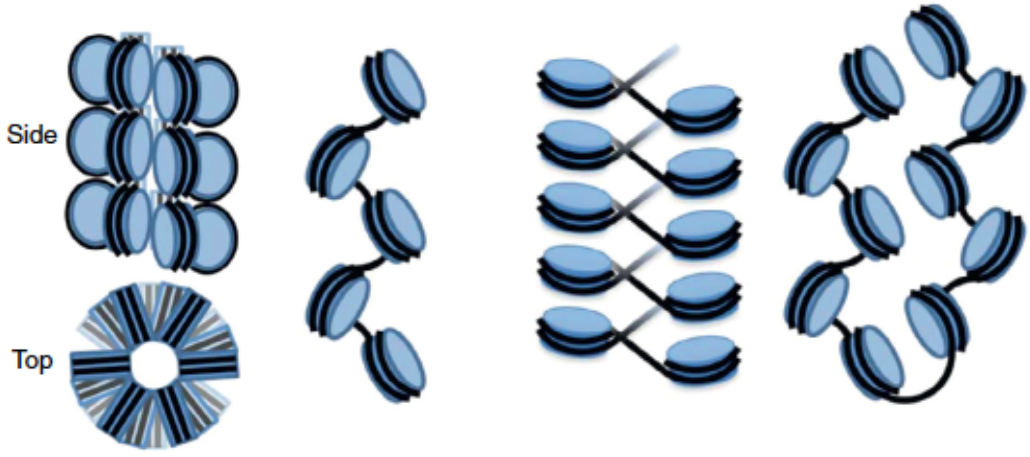

Figure 4. A) Condensed 30 nm structures of chromatin, B) beads-on-a-string (10 nm) structure, C) and D) other higher-ordered chromatin organization (35)

1.1.2 Epigenetics and cancer:

Epigenetics is the heritable changes in gene expression that occur without changing the DNA sequence. The epigenetic changes in cancer cells are termed as cancer

epigenetics (36,37). The genetic mutation (change in the DNA sequence) plays a very important part in tumorigenic behavior of a cell. The epigenetic changes also play a significant role to convert a normal cell to cancer cell. Epigenetic changes cause the silencing of tumor suppressor genes and activation of the oncogenes. Oncogenes are genes that have a potential to cause cancer and which are expressed in a large level in cancer cells (38). Tumor suppressor genes (also called anti-oncogene) are the genes that save a cell from developing cancer. So, if the tumor suppressor gene loses its activity, a cell can progress to cancer (39,40). The main epigenetic changes are methylation of DNA and acetylation of histones. Understanding the precise roles of these changes in cancer development can be extremely helpful in cancer detection, prevention and therapeutic uses (41,42). As for example, DNA methylation and histone deacetylation are known to induce cancer. The inhibitors of DNA methylation and histone deacetylation have shown clinical activities against some cancers caused by hypermethylation.

1.1.3 DNA methylation and cancer

There have been a lot of researches on the extent of methylation of the CpG island and the entire genome for normal and cancer cell. The CpG regions are the positions of DNA where a cytosine sits beside a guanine. The ‘p’ in the terminology stands for phosphate backbone connection and differentiates CpG from the CG terminology (cytosine-guanine base pairing). The cytosine in the CpG islands can be methylated to form 5-methyl cytosine and the enzyme responsible for this process is called DNA methyl transferase (DNMT).

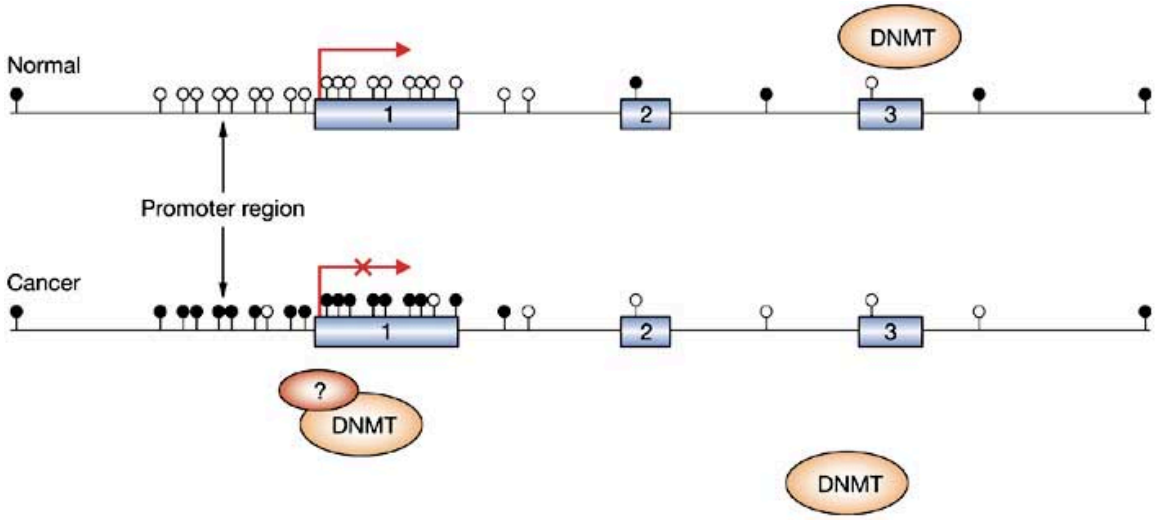

Figure 5. DNA methylation in normal and cancer cell. White circle: unmethylated, black circle: hypermethylated, 1, 2, 3 : exons; transcription in the promoter region in cancer cell is stopped (marked as 'X' sign). Adapted from reference (43)

DNA hypermethylation can cause transcriptional silencing of the tumor suppressor genes. The 5' carbon of the cytosine at CpG sites can be covalently methylated to form 5'-methylcytosine. These methyl groups are projected into the major groove and transcription is stopped. The CpG sites are found in less than the expected frequencies throughout the whole genome but in much higher frequencies in the promoter region. These small regions with CpG sites near the promoter region are termed as CpG islands. In normal cells, the CpG islands are almost unmethylated whereas rest of the genome is heavily methylated. But in cancer cells, the CpG islands are found to be heavily methylated (43–45). The addition of methyl group is controlled by the enzyme family DNMTs (DNA methyltransferases) (figure 5). In mammalian cells, DNMT1, DNMT3a, DNMT3b are commonly found DNMTs.

1.1.4 Histone modifications and cancer

Different modification of the histone tail is another epigenetic mark for cancer. The most common modifications are acetylation and methylation. It has been shown that DNA methylation is sometimes closely associated with histone hypoacetylation and hypermethylation. Histone acetylases (HAT) and Histone deacetylases (HDAC) are very important enzymes for controlling the acetylation status of histone lysine. When the promoter region CpG is hypermethylated, some proteins like MeCp2, HDAC are recruited to that area. Once HDAC is recruited, it causes the deacetylation of the histone lysine residues.(46–48) Deacetylated lysine residues interact strongly with the phosphate backbone because of the strong charge interaction between histone and DNA resulting in a compact chromatin structure and making the DNA inaccessible. As a result, transcriptional complexes can't access DNA and transcription stops (figure 6).

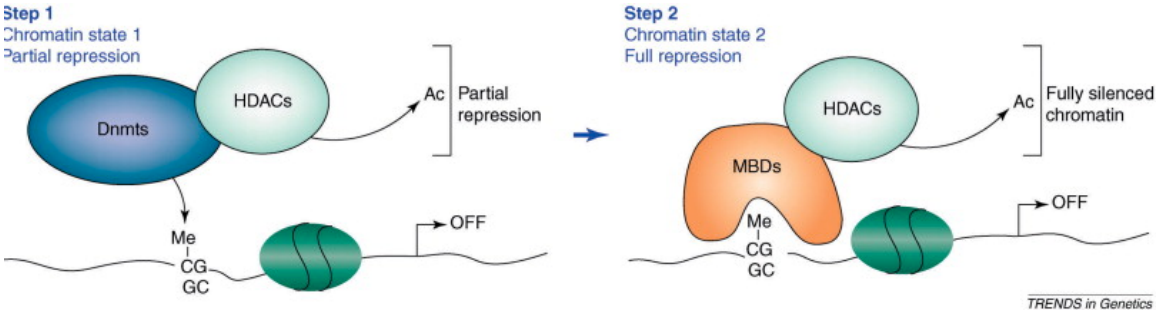

Figure 6. Histone deacetylation is induced by DNA methylation. MeCP2 binds with methylated DNA and recruits HDAC (which deacetylates histone lysines). Adapted from reference (49)

1.1.5 Epigenetic changes and structure of chromatin

The structure of the chromatin is also dependent on the extent of DNA methylation and histone modifications. If the DNA in promoter region is

hypermethylated, methyl binding protein MeCp2 comes to the promoter region and binds with methylated DNA. In turn, other protein complexes like HDAC also come to that region (50). As a result of that, the lysine tails of histones get deacetylated. When histones are deacetylated, the amine groups in the lysine get positively charged and interacts strongly with the negatively charged DNA phosphate backbone, resulting in the formation of a compacted chromatin structure (51,52). But when the histone is methylated, the lysine residues induce weak interaction with the phosphate backbone and as a result of that, a more open chromatin structure is observed.

1.1.6 AFM as an imaging tool

There have been a lot of studies involving reconstituted chromatin (*in vitro*) in recent years and their analysis using different microscopic techniques (SEM, AFM etc). Atomic force microscopy can play as a key tool in this study (53–55). But even though the experiments involving these reconstituted chromatins give us valuable information about their structure and properties, it is impossible to create the '*in vivo*' conditions. This is because chromatin is assembled by specific enzymes in vivo, and is much more densely packed with nucleosomes than is possible with equilibrium reconstitution (56). There have been recent advancements in this field involving AFM imaging of chromatin samples extracted directly from live cells. There is still huge potential to study the chromatin structure and properties of normal cells and cancer cells using AFM imaging and recognition imaging technique.

1.2 Atomic force microscopy

As described earlier, AFM has become a very important and powerful tool for surface analysis in material science, biochemistry and nanoscience. It has many

advantages over the other popular imaging techniques such as Scanning Electron Microscopy (SEM) or Transmission Electron Microscopy (TEM) or STM. For examples,

a) AFM can be used in air, vacuum or liquid but SEM or TEM can't be.
b) AFM can be used to image biomolecules in their native state, so imaging of living cell is even possible.
c) AFM has a better resolution than SEM.
d) AFM can image any type of surface unlike STM which need conducting surface.
e) AFM can generate three-dimensional image.

Although there are some disadvantages of AFM like slow scan speed or smaller scan area, it has become immensely popular in the field of nanotechnology. And force spectroscopy and recognition imaging have made AFM indispensible in the world of bio-nanotechnology. Also AFM can be used with fluorescent microscopy as a combination, further increasing its applicability.

1.2.1 Working Principle

AFM is special type of scanning probe microscopy. AFM uses a cantilever carrying a tip or probe that actually scans the surface. When the tip is brought too near to the surface, forces acting between the tip and surface come into play and the cantilever is deflected according to Hooke's law depending upon the spring constant of the cantilever (figure 7). Hooke's law states that, the force (F) needed to extend or compress a spring by a distance (x) is actually proportional to the spring constant or its stiffness (k).

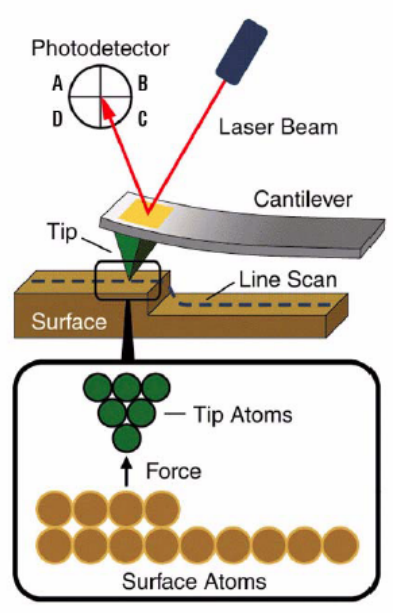

Figure 7. Working principle of atomic force microscopy (adapted from Agilent 5500 manual)

So, according to Hooke's law, $F = -kx$

(the negative sign indicates that the direction of the restoring force is actually opposite to the direction of the displacement).

1.2.2 Different parts of AFM:

Figure 8. An Agilent 5500 AFM instrument (image adapted from Agilent 5500 manual)

The following parts are integral to an atomic force microscopy.

a) AFM probe:

This actually consists of a holder plate (or, chip) that carries a cantilever with a sharp tip on it. The holder plate allows the operator to hold the plate (and hence the tip) with a sharp cantilever and place it on the scanner for measurements. The size of the holder plate is around 1.5 mm X 3.5 mm. The cantilever on it is about few micrometer and the radius of dimension of the tip is in the range of nanometer. Silicon or silicon nitride are two most common material used for the AFM tip. But there are some other tips such as carbon, diamond, quartz etc. In addition to that, there are some tips which are coated by gold, platinum/iridium, diamond, cobalt allow etc. The material of the tip is determined by the mode of AFM and also the sample under investigation. The shape of the AFM tips can also differ. For example: point probe, rotated, tetrahedral pyramid, square pyramid, rectangular based etc. The dimension of the holding chip is ~ 3.4 mm X 1.6 mm X 0.3 mm. And the length of the cantilever is around 15-30 μm (figure 9. A).

b) AFM scanner:

The scanner incorporates a piezoelectric material which elongates or contracts in presence of an electric field applied on the scanner (figure 9. B). The tip is placed on the scanner and it moves along the z-axis while rastering along the x and y-axis. This movement is controlled by the scanner.

C) Detector:

The laser spot is reflected from the back of the cantilever and goes to the photodiode detector (figure 9.C). The top and bottom half of the photodiode detect the deflection

signal and left and right halves detect the friction signal. The detector can be mounted on the scanner.

D) Sample plate:

This is the plate that holds the sample or surface to be analyzed (figure 9. D). Depending on the experimental needs, different sample plates are available (for example, in liquid imaging, MAC mode imaging, temperature controlled imaging etc).

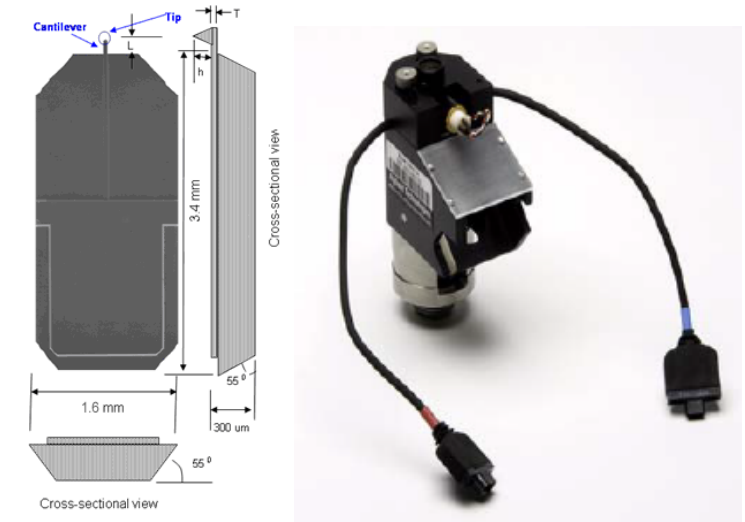

A B

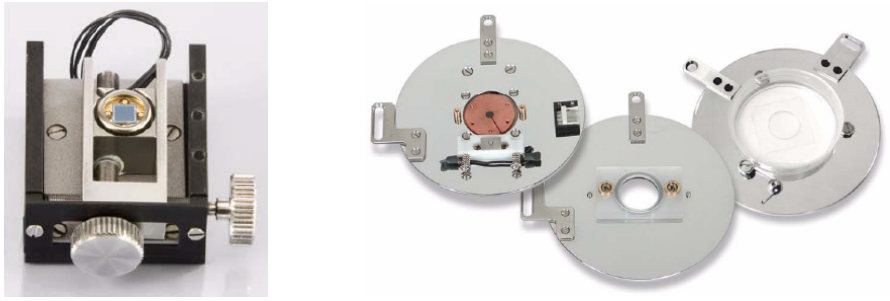

C D

Figure 9. A) Schematic diagram and dimensions of AFM probe consisting the cantilever and tip, B) AFM scanner, C) photodiode, D) sample plates (adapted from Agilent 5500 manual)

1.2.3. Modes of AFM:

AFM can mainly operate in three modes:

a) Contact mode

b) Non-contact mode

c) Tapping mode

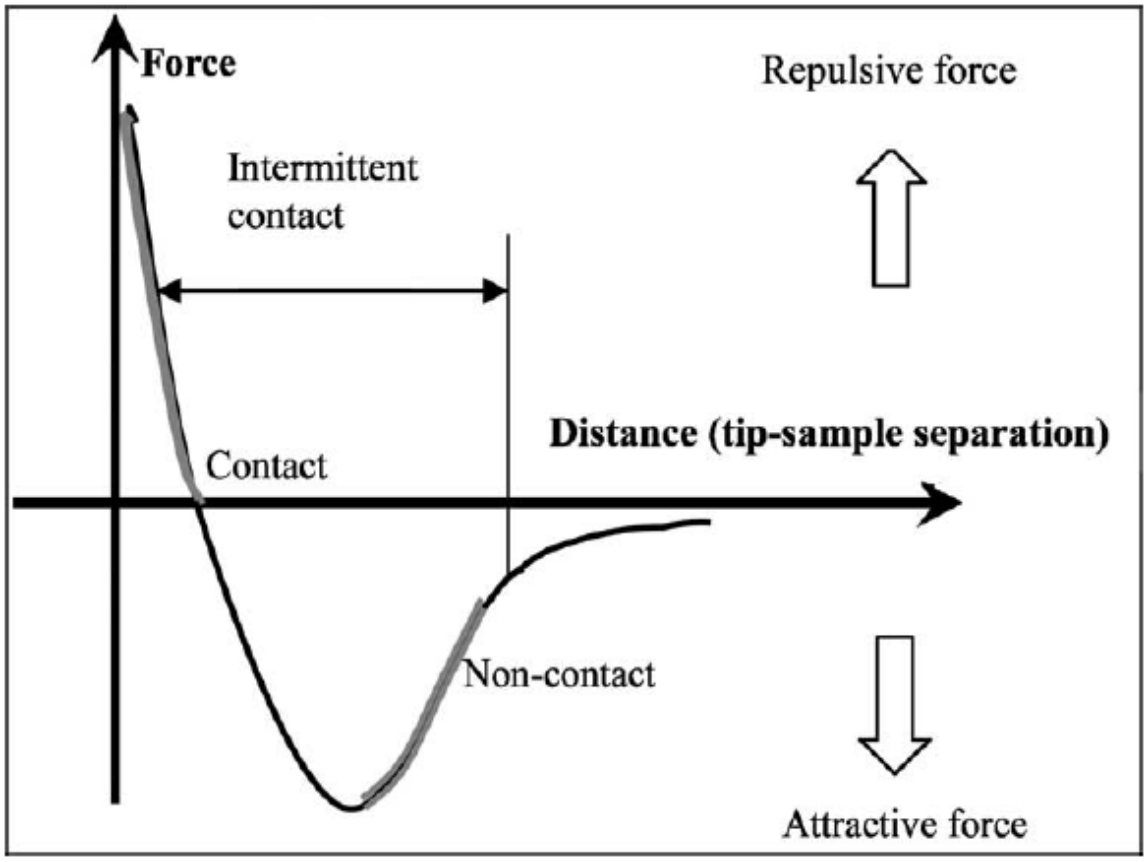

Figure 10. Interatomic force vs distance curves. The short-range force is repulsive in nature and the long-range force is attractive. Different modes of AFM operate in different region of the curve.

Contact mode:

In contact mode, the tip remains in close contact with the sample surface. The interaction between the tip and the surface is repulsive in nature (figure 10). Contact AFM can be done in two modes: *constant height* mode and *constant force* mode. But because the tip drags over the surface being in physical contact with the surface, the soft biological samples can be damaged and they are not suitable samples.

Non-contact mode:

As the name suggests, in non-contact mode, the tip doesn't touch the surface. Rather the cantilever oscillates near or at its resonance frequency being some distance away from the sample surface (50-150 Å). This mode acts in the attractive region of the force-distance graph (figure 10). Since the tip never touches the sample, 'soft' biological samples can be used. But the resolution of images in tapping mode is in generally low.

Tapping mode:

In tapping mode, the tip oscillates at or near its resonance frequency but also intermittently touches the surface. Tapping mode is a huge improvement in AFM scanning system. It gives high resolution AFM image without damaging soft samples. That's why it became hugely popular in the field of biological samples.

MAC mode:

MAC mode is an ideal mode to scan soft biological samples in liquid environment with high resolution and without damaging the sample. In other modes, the scanner drives the tip with a fixed oscillation. But in MAC mode, the tip is driven by the magnetic field generated by the solenoid placed under the sample plate holder (figure 11). Since the scanner doesn't vibrate in this case, the background noise is absent and the images become cleaner.

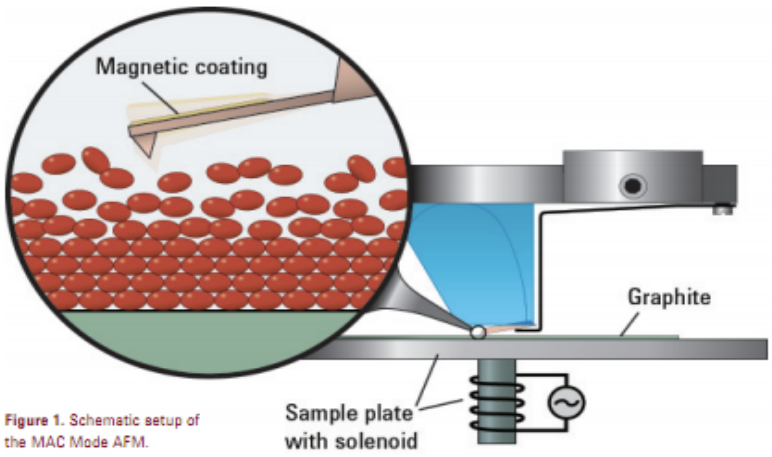

Figure 11. Schematics of MAC mode operation (image taken from Agilent 5500 manual)

1.2.4 Force spectroscopy

Even though AFM is widely known as on of the most powerful tool for imaging a surface with nanometer resolution, what makes it more important is its capability to extend its function to other forms of measurement and analysis. One such example is its ability to measure force of interactions with pico-newton precision.

In AFM force measurement experiments, the tip is functionalized with a molecule and corresponding cognate molecules (that binds with the molecule on the tip) are immobilized on the surface. Then during the measurement, the tip is brought near the surface so that the two molecules can bind and then tip is retracted to break the binding. This unbinding force can be measured by the AFM force-distance curves (figure 12).

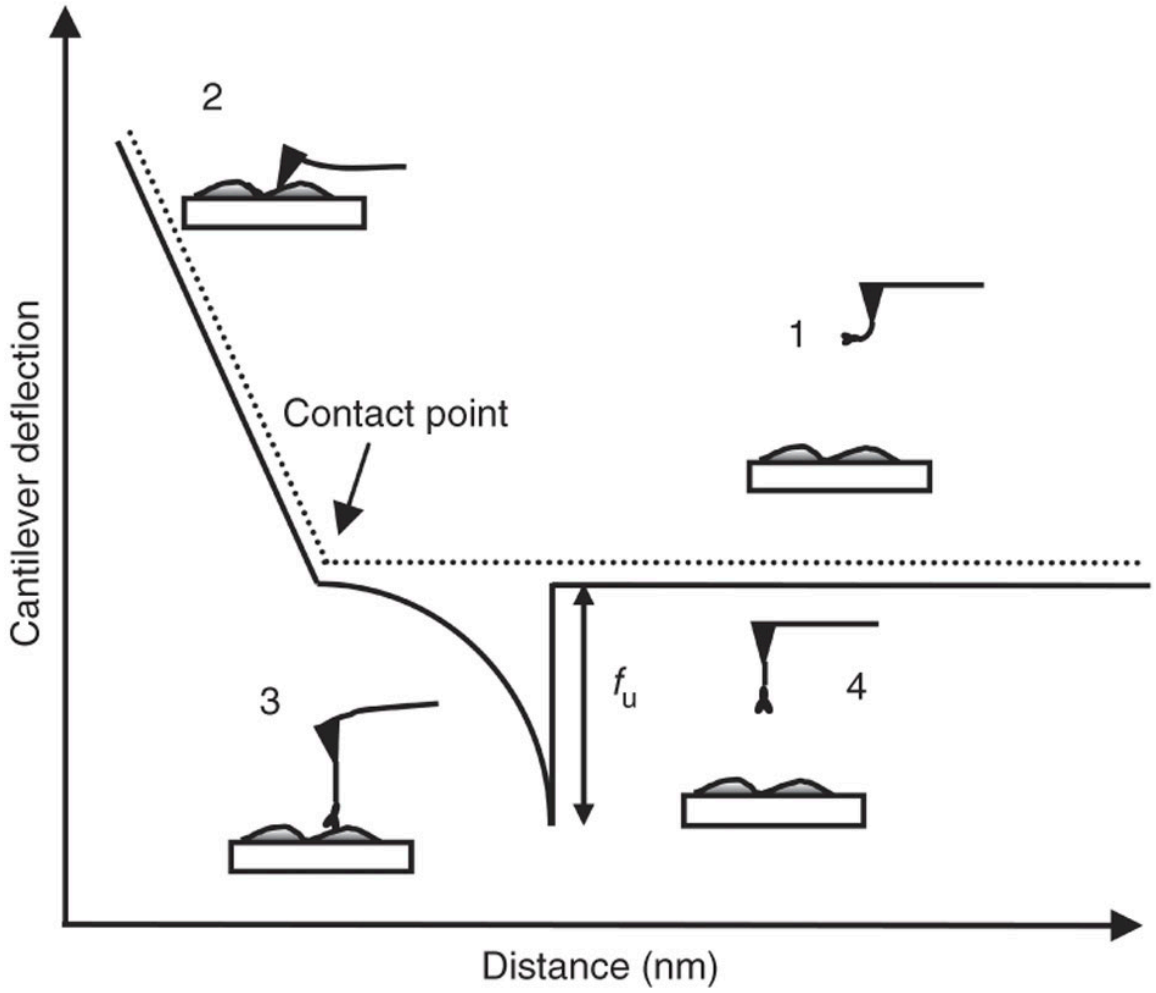

Figure 12. Schematic representation of a force-distance cycle (approach and retraction). The force is plotted against the traveling distance. Approach of the tip toward the surface is shown as the dotted line (1, 2) and subsequent retraction away from the surface is shown as the solid line. Adapted from reference (57)

This approach and retraction can be repeated in the same and different places to generate a statistical collection of force curves. From this collection, a histogram can be plotted resulting in the distribution of unbinding force (figure 13). In a standard AFM force curve, the x-axis denotes the distance between the tip and the substrate whereas the y-axis denotes the deflection of the cantilever.

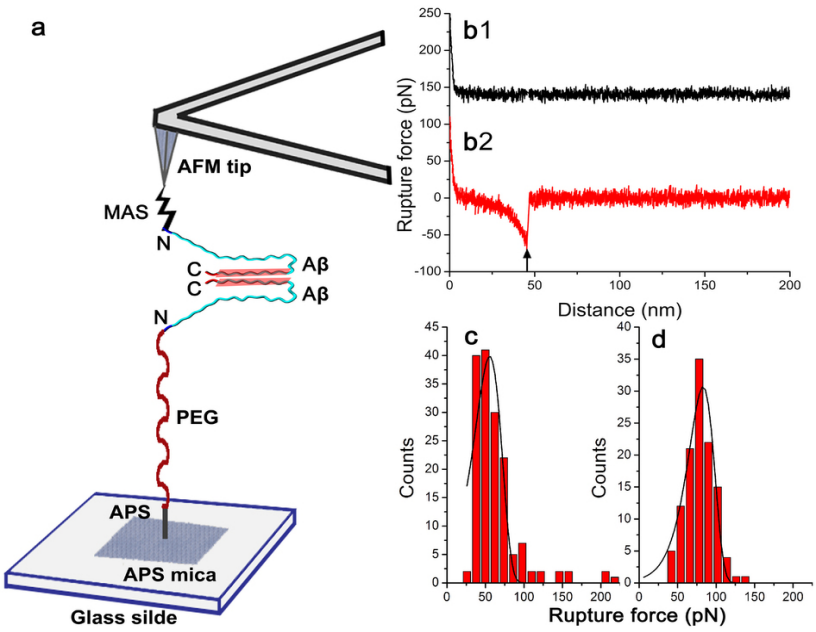

Figure 13. Force of interaction between two Aβ molecules measured by AFM force measurement, a) schematics of one Aβ molecule attached to the AFM tip and the other Aβ immobilized on APS-mica, b1) force-distance curve with no interaction, b2). Force-distance curve with specific interaction, c) force histograms for Aβ40 unbinding, d) force histograms for [VPV]Aβ40 unbinding. Adapted from reference (58)

1.2.5 Recognition imaging

To fully explore the power of atomic force microscopy, AFM was made capable of detecting specific interaction between two molecules while simultaneously acquiring a topographical image. This mapping of the specific interaction using AFM is termed as recognition imaging. Like the force spectroscopic measurements, here also the tip is functionalized with a molecule and the corresponding cognate molecules are immobilized on the surface. If the molecule on the tip binds with the molecule on the surface, a dark spot is observed corresponding to the immobilized molecule on the surface. If the binding doesn't take place, the dark spot doesn't show up.

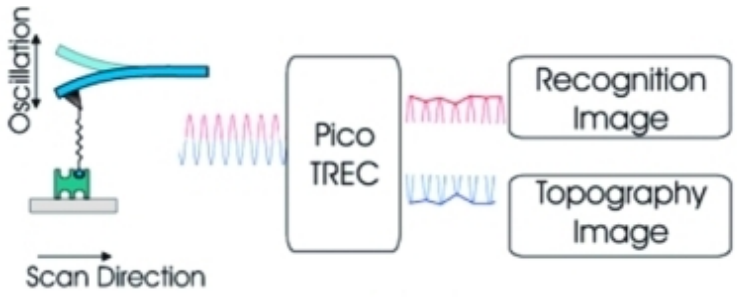

Figure 14. Working principle of recognition imaging. The change in the oscillation of the upper part (pink) and lower part (blue) of the signal get separated by the Pico TREC box and they give recognition image and topographic image respectively. Adapted from reference (59)

Figure 14 explains the working principle of the recognition imaging. The molecule on the tip is usually bound with the tip using a PEG linker. When there is a binding between the two molecules, there occurs a change in the upper part of the sinusoidal amplitude signal as the tether molecule is pulled on (reducing the top amplitude). Because of the interaction between the tip and the immobilized molecules, the bottom half of the signal gets dampened in the normal way. At the same time, the cantilever can't come back to its original position (when unbound) because now it's bound to the molecule on the surface via the PEG linker. Hence, the upper part of the oscillation also gets affected. This change in upper part and lower part of the oscillation can be detected and separated by Pico TREC. TREC stands for simultaneous topography and recognition. This change in the lower part produces the topography image and change in the upper part produces the corresponding recognition image.

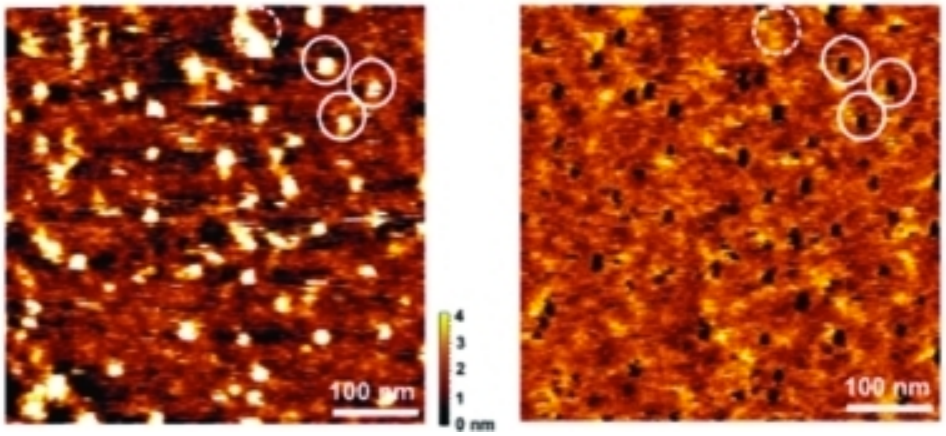

A B

Figure 15. A) Topographic image of the avidin molecules (white spots) immobilized on mica surface. B) recognition of avidin molecules (dark spots). Solid circled line represents the avidin molecule mapping whereas dotted circled line didn't produce any darks spot indicating the specific nature of the binding. Adapted from reference (59)

In the example given as figure 15, avidin was electrostatically immobilized on mica surface and the tip was functionalized with biotin. The yellow spots in left image represent the avidin protein. Corresponding black spots denote the recognition signal due to the binding of avidin and biotin. To test the specificity of these signals, 'blocking' experiment is performed. For example, in this case free avidin solution was passed into the flow cell. Now, the biotin on the tip binds with the free avidin. Hence, this 'avidin bound biotin' couldn't interact with the avidin on the surface. As a result, the recognition signal stopped establishing the specific nature of the interaction.

Similarly, using recognition imaging different proteins, protein modifications, DNA methylation etc. have been detected.

1.3 Applications of AFM in chromatin study

After application of AFM technology for different protein systems, AFM was

utilized in other biological systems as an obvious extension. AFM has been used in live cell imaging (60–62), recognition imaging in live cell (63), imaging and recognition of reconstituted and native chromatin arrays (extracted from cell lines) (64).

Similarly, in this study we are trying to address the structures, shapes and behavior of chromatin fractions extracted using different salt fractions and do a direct comparison between normal and cancer cell lines. AFM topographic and recognition imaging, DNA agarose gel and SDS-PAGE gels are the main techniques deployed for this study. To conduct the recognition imaging experiments, we first developed a method of functionalizing AFM tips in aqueous medium using a vinyl sulfone PEG linker. Then two different proteins (integrin and thrombin) were detected by recognition imaging using a novel tri-arm linker. Finally, native chromatin samples were analyzed using AFM and gel techniques.

CHAPTER 2

APPLICATION OF CATALYST FREE CLICK REACTIONS IN ATTACHING AFFINITY MOLECULES TO TIP OF AFM

2.1 Introduction

Atomic Force Microscopy (AFM) has been extensively used in studies of biological interactions. Particularly, AFM based force spectroscopy and recognition imaging can sense biomolecules on a single molecule level, having great potential to become a tool for molecular diagnostics in clinics. These techniques, however, require affinity molecules to be attached to AFM tips in order to specifically detect their targets. The attachment chemistry currently used on silicon tips involves multiple steps of reactions and moisture sensitive chemicals, such as (3-aminopropyl)triethoxysilane (APTES) and N-hydroxysuccinimide (NHS) ester, making the process difficult to operate in aqueous solutions. In the present study, we have developed a user-friendly protocol to functionalize the AFM tips with affinity molecules. A key feature of it is that all reactions are carried out in aqueous solutions. In summary, we first synthesized a molecular anchor composed of cyclooctyne and silatrane for introduction of a chemically reactive function to AFM tips and a bi-functional polyethylene glycol linker that harnesses two orthogonal click reactions, copper free alkyne-azide cycloaddition and thiol-vinylsulfone Michael addition, for attaching affinity molecules to AFM tips. The attachment chemistry was then validated by attaching anti-thrombin DNA aptamers and cyclo-RGD peptides to silicon nitride (SiN) tips respectively, and measuring forces of unbinding these affinity molecules from their protein cognates human α-thrombin and human $\alpha_5\beta_1$-integrin immobilized on mica surfaces. In turn, we used the same attachment chemistry to

functionalize silicon tips with the same affinity molecules for AFM based recognition imaging, showing that the disease-relevant biomarkers such as α-thrombin and $\alpha_5\beta_1$-integrin can be detected with high sensitivity and specificity by the single molecule technique. These studies demonstrate the feasibility of our attachment chemistry for the use in functionalization of AFM tips with affinity molecules.

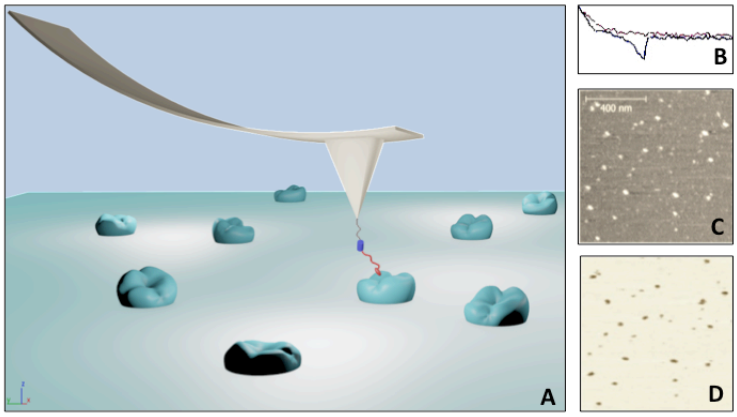

Figure 16. Illustration of an AFM tip with an affinity molecule tethered at its apex to specifically recognize its protein cognates immobilized on a substrate (A). Using contact mode, a force of the affinity molecule unbinding from its cognate can be determined by retracting the tip along the Z direction (B). By tapping the functionalized tip on the surface along the X to Y direction, topographic and recognition images can be generated (C, D). In general, the affinity molecule can be a ligand, an antibody, an aptamer, and so on.

The human proteome consists of millions of proteins, many of which occur in minute concentrations below limits of detection (LOD) of current technologies such as ELISA, mass spectrometry and protein microarrays (65). Therefore, there is a long felt need of a molecular tool capable of directly detecting those disease relevant protein biomarkers present in low abundance without any additional manipulation such as post-

assay signal amplification. AFM has been envisioned as a mean of nanodiagnostics due to its single molecule sensitivity (66). It has been demonstrated that in combination with irreversible binding, AFM can reach a concentration sensitivity limit of 10^{-17} M (67). While AFM has been exploited in the analysis of DNA, proteins and cells, its chemical sensibility has grown tremendously as well. As illustrated in Figure 16, AFM is capable of "seeing and counting" target molecules when its tip is equipped with an affinity molecule. The interactions between antibody and antigen, ligand and receptor, DNA probe and target etc. can be determined and characterized at a single molecule level by AFM force measurements, termed as Molecular Recognition Force Spectroscopy (MRFS) (68). Also, AFM has been enabled to scan individual proteins immobilized on a surface with an affinity molecule tethered to its tip, known as Recognition Imaging (RI) (69). It is conceivable to employ both MRFS and RI for identification and detection of protein biomarkers in a clinic setting. This requires that these techniques are robust, supported with well-designed chemistry and bioassays. Recent advances in automated AFM-based force spectroscopy should facilitate the instrument operation. One of our efforts has been directed towards developing simple attachment chemistry that works in aqueous solutions without any of organic solvents involved so that it can easily be adapted in biological laboratories and clinics.

A molecular linker is often employed to attach affinity molecules to AFM tips, which provides an advantage in distinguishing between specific and nonspecific interactions (70). The heterobifunctional poly[ethylene glycol] (PEG) has become a commonly used linker (71). In general, the attachment is a three-step process that begins with functionalizing an AFM tip with a chemically reactive group, tethers the PEG linker

to the AFM tip, and then reacts with an affinity reagent. (3-Aminopropyl)triethoxysilane (APTES) is a choice reagent for amination of silicon tips (72,73), but it is notoriously problematic for forming uniform monolayers, especially when the reaction is carried out in a liquid phase (74,75). APTES should be freshly redistilled before use in order to achieve reproducible results. Chemical vapor deposition of APTES has been developed to improve the outcome (72), but the process is tedious, requiring a thorough purge of the deposition chamber with argon to remove trace of moisture. Without developing an automated apparatus, it is difficult to be scaled up. The reaction of amine with NHS (N-Hydroxysuccinimide) ester has been one of the most commonly used methods for tethering carboxylated PEG linkers to AFM tips (76–78). The NHS ester is sensitive to moisture, and prone to rapid hydrolysis with increase in pH (a half-life time of 4-5 hours at pH 7 and one hour at pH 8) (79). On the other hand, the amine exists in an aminium form at the neutral pH, requiring a basic condition to be deprotonated for its nucleophilic activity. These caveats make it difficult to handle the NHS ester reaction in aqueous solutions and one has to fine tune pH, reaction time in order to achieve optimal outcomes.

Here, we report on a new scheme of attaching affinity molecules to AFM tips based on click chemistry (Figure 17). Chen *et al* have employed a copper-catalyzed alkyne-azide reaction to attach antibodies to a gold coated AFM tip through an azido-PEG-thiol linker (80). To take it further, we implement two orthogonal catalyst-free click reactions for the attachment of affinity molecules to silicon tips. First, we have synthesized a molecular anchor composed of cyclooctyne and silatrane for the introduction of an alkyne function to the silicon tip. In aqueous solution, the silatrane moiety reacts with silanol on silicon surfaces to form a monolayer. It has been known that

silatrane is less reactive than alkoxysilanes and extremely resistant to polymerization at a neutral pH (81). Gruber and Lyubchenko *et al* have employed 1-(3-aminopropyl)silatrane (APS) as a substitute of APTES in functionalization of AFM tips and mica surfaces (82–84). Thus, we expected that the new anchoring molecule would form a uniform cyclooctyne monolayer on the silicon tips. The ring strained cyclooctyne promotes the alkyne-azide reaction without the copper catalyst (85). In addition, we have synthesized a new class of molecular linkers, azido-PEG-vinyl sulfone with defined lengths, for connection of affinity molecules to AFM tips. In the present study, we have focused on attaching thiolated oligonucleotide aptamers and affinity peptides to AFM tips because they are rapidly growing areas in molecular diagnostics (86). The reaction of vinyl sulfone with thiol in aqueous solution comprises another category of click chemistry in bioconjugation (87), being used for the labeling of proteins (88), and proteomes (89). We adapt it as a first click reaction to connect thiolated affinity molecules to the PEG linker as illustrated in Figure 17. The second click (azide to alkyne) finishes the process of the attachment. These two click reactions are orthogonal so that there are no cross talks between each other.

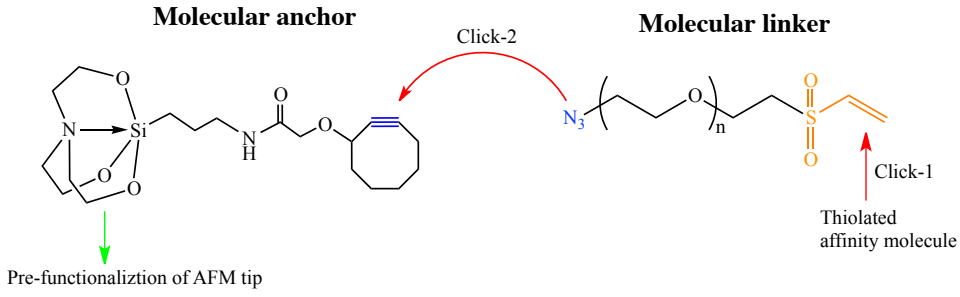

Figure 17. New chemical scheme to attach affinity molecules to AFM tip using two click reactions

2.2. Materials and Methods

2.2.1 General information

All chemicals were purchased from commercial suppliers (Sigma-Aldrich, Fluka, Santa Cruz Biotechnology, Alfa Aesar). Anhydrous organic solvents were Sure/Seal™ from Aldrich. Thrombin aptamers were custom synthesized by IDT (Integrated DNA Technologies) and human α thrombin was purchased from Abcam, Azido-dPEG®$_{36}$-alcohol was purchased from Quanta Biodesign, human $\alpha_5\beta_1$ integrin from YO Proteins AB (Sweden), cylco(RGDfK) and cyclo(RGDfC) from Peptides international. All the synthetic reactions were carried out under nitrogen atmosphere. Thin layer chromatography (TLC) was used to monitor progress of organic reactions. An automated flash chromatography system (CombiFlash Rf, Teledyne Isco, Inc.) was used to separate the organic compounds with silica gel columns. FTIR data were collected using Thermo Scientific Nicolet™ 6700 FT-IR spectrometer. The HPLC purification was carried out in Agilent 1100 series equipped with a UV detector and a fraction collector. All the proton NMR (^{1}H) spectra were recorded on a Varian 400 MHz instrument. ^{1}H chemical shifts were referenced relative to the residual solvent peak (such as $CDCl_3$: δ_H = 7.24 ppm). MALDI-TOF analysis was performed on Voyager-DE STR instrument. We used water from Millipore's Milli-Q water purification system with a real time monitor of total of carbon (TOC) connected to a BioPak Polisher to remove biological contaminates. TOC level was strictly maintained below 5 ppb.

2.2.2 Synthesis

N-(3-(silatranyl)propyl)-2-(cyclooct-2-yn-1-yloxy)acetamide (3):

EDC (115 mg, 0.6 mmol) was added to a solution of 2-(cyclooct-2-yn-1-yloxy)acetic acid (100 mg, 0.5 mmol) in anhydrous dichloromethane (2 mL). The solution was stirred for 30 minutes, followed by the addition of APS (140 mg, 0.6 mmol). After 3 hours, the reaction was stopped by rotary evaporation to remove the solvent. The crude product was purified by flash chromatography in a silica gel column using a gradient of methanol (0-5% over 3 h) in dichloromethane to give a white solid (130 mg, 60%). ^{1}H NMR (400 MHz, $CDCl_3$): δ = 0.4 - 0.44 (m, 2 H), 1.15 - 2.25 (m, 10 H), 1.58 - 1.64 (m, 2 H), 2.79 (t, 6 H, J= 6 Hz), 3.24 (m, 2 H), 3.74 (t, 6 H, J = 6 Hz), 3.81 (d, 1 H, J = 15.2 Hz), 4.0 (d, 1 H, J = 15.2 Hz), 4.2 (t, 1 H), 6.65 (s, 1 H, broad); ^{13}C NMR (50 MHz, $CDCl_3$): δ = 13.2, 20.6, 24.9, 26.2, 29.6, 34.2, 41.8, 42.1, 51.1, 57.7, 68.5, 73.0, 91.5, 101.3, 169.1. HRMS (FAB): *m/z* (M+H) calculated for $C_{19}H_{32+1}N_2O_5Si$: 397.2158; found: 397.2159.

Special note on nomenclature: To avoid excessive use of a long series of numbers, the mathematical shorthand for expressing arithmetic progressions is used to denote the positions of oxygen atoms in the elongated PEG chains, as proposed by Hii and coworkers.[1]

35-azido-3n$_{33}^{3}$-undecaoxapentatriacontan-1-ol (5):

Sodium hydride (0.71g, 29.5mmol) was added to a solution of hexaethylene glycol (6.42g, 22.7 mmol) in anhydrous tetrahydrofuran (THF) (40 mL) with stirring at 0 °C. After 1 hour, to the mixture a solution of compound **4** (3.5g, 7.5mmol) in anhydrous THF (20 mL) was added. The mixture was allowed to warm to room temperature, stirred for another 15 hours, to which methanol (5 mL) was added dropwise to stop the reaction. After removing the solvent, the crude product was purified in a silica gel column by flash

chromatography using a gradient of methanol (0-5% over 4 h) in dichloromethane. Compound **5** was obtained as a colourless liquid (3.1g, 71%). ^{1}H NMR (400 MHz, CDCl3): δ = 2.7 (s, 1 H, broad), 3.34 (t, 2 H, J = 4.8 Hz), 3.55-3.69 (m, 46 H); HRMS (APCI): *m/z* (M+H) calculated for $C_{24}H_{49+1}N_3O_{12}$: 572.3395; found: 572.3391.

1-Azido-35-(2-(vinylsulfonyl)ethoxy)-3n$_{33}$^{3}-undecaoxapentatriacontane (6a):

To a solution of **5** (100 mg, 0.18 mmol) in anhydrous THF (2 mL), divinyl sulfone (180 μL, 1.8 mmol) was added with stirring, followed by the addition of potassium t-butoxide (23 mg, 0.2 mmol). The reaction was monitored by thin layer chromatography (TLC). Within one hour, the starting material **5** was consumed and a less polar spot observed on the TLC plate. The reaction mixture was filtered, concentrated, and purified in a silica gel column by flash chromatography using 0-4% gradient (over 4 hours) of methanol in dichloromethane to furnish compound **6a** as a colorless liquid (77 mg, 64%). FTIR (cm^{-1})**:** 1102 (S=O symmetric stretch), 1313 (S=O asymmetric stretch), 1605 (C=C stretch), 2101 (N=N=N stretch), 3056 and 3097 (sp^{2} C-H stretch); ^{1}H NMR (400 MHz, $CDCl_3$): δ = 3.24 (t, 2 H, J = 5.2 Hz), 3.36 (t, 2 H, J = 5.2 Hz), 3.6-3.87 (m, 46 H), 3.88 (t, 2 H, J = 5.2 Hz), 6.06 (d, 1 H, J = 9.6 Hz), 6.37 (d, 1 H, J = 16.8 Hz), 6.8 (dd, 1 H, J = 16.8 Hz and 10 Hz); ^{13}C NMR (50 MHz, $CDCl_3$): characteristic peaks for PEG were observed. Two characteristic peaks for carbon atoms of vinyl sulfone was observed at δ = 126.68, 137.99; HRMS **(**APCI**):** *m/z* (M+H) calculated for $C_{28}H_{55+1}N_3O_{12}S$: 690.3483; found: 690.3469.

1-Azido-35-(2-(vinylsulfonyl)ethoxy)-3n$_{105}$^{3}-pentatricontaoxaheptahectane (6b):

To a solution of Azido-dPEG®36-alcohol (50 mg, 0.03 mmol) in anhydrous THF (1 mL), divinyl sulfone (36 mg, 0.3 mmol) was added with stirring, followed by the

addition of potassium t-butoxide (4 mg, 0.035 mmol). The reaction was monitored by thin layer chromatography (TLC). Within one hour, the starting material was consumed and a less polar spot observed on the TLC plate. The reaction mixture was filtered, concentrated, and purified in a silica gel column by flash chromatography using 0-4% gradient of methanol in dichloromethane. The product **6b** was separated as a white solid (33 mg, 61%). FTIR **(**cm^{-1}): 1104 (S=O symmetric stretch), 1315 (S=O asymmetric stretch), 1600 (C=C stretch), 2100 (N=N=N stretch), 3060 and 3100 (sp^2 C-H stretch); ^1H NMR (400 MHz, CDCl3): δ = 3.26 (t, 2 H, J = 5.6 Hz), 3.39 (t, 2 H, J = 5.6 Hz), 3.5 - 3.7 (m, 142 H), 3.9 (t, 2 H, J = 5.6 Hz), 6.09 (d, 1 H, J = 10 Hz), 6.39 (d, 1 H, J = 16.4 Hz), 6.82 (dd, 1 H, J = 10 Hz and 16.4 Hz); ^{13}C NMR (50 MHz, CDCl3): characteristic peaks for PEG were observed. Two characteristic peaks for carbon atoms of vinyl sulfone was observed at δ = 128.7, 137.9; MALDI-MS: m/z (M-H+Na) calculated for $C_{76}H_{151}N_3O_{38}SNa$: 1769.0651; found: 1769.2117.

2.2.3 Reactions of DNA Aptamers with molecular linkers

A solution (20 μL, 10 mM) of Thrombin-binding DNA aptamer 5'-GGTTGGTGTGGTTGG with a disulfide linker at 3'-end (IDT code: 3ThioMC3-D) in 0.1 M phosphate buffer (pH 8.0) was treated with TCEP (5 μL, 170 mM in 0.1 M TEAA buffer, pH 7.0). After 3 h, the reaction mixture was passed through a size-exclusion G-25 column (GE Healthcare) to remove small thiol molecules. The G-25 column was prepared following the protocol described by the manufacturers. First, the storage buffer was removed by centrifugation (1 min, 735 x g). Then the column was rehydrated again with double distilled water, followed by centrifugation (1 min, 735 x g). Finally, the reaction mixture was added to the column, followed by centrifugation (2 min, 735 x g).

The eluted solution containing thiol-functionalized aptamers (~25 μL) was then added to a solution of PEG linker **6a** in 0.1 M phosphate buffer, pH 8.0 (20 μL, 50 mM). The reaction was finished in three hours, monitored by MALDI-TOF mass spectrometry. The product **D-1a** was purified using reverse phase HPLC with a Zorbax Eclipse Plus C18 column (4.6 x 150 mm, particle size 5 μm) with a gradient of 0% to 70% over a period of 25 mins (solvent A: a 0.1 M TEAA buffer, pH 7.0; solvent B: acetonitrile). The product has retention time of 17.4 min (with ~95% conversion). MALDI-TOF Mass: m/z (M+H) calculated for **D-1a**: 5570.51; found: 5571.63. After collecting the product using HPLC, the fraction was lyophilized to get the pure product.

D-1b was synthesized in the same way and purified by HPLC with retention time of 17.1 min (with conversion ~89%). MALDI-MS: m/z (M + H) calculated for **D-1b**: 6649.23; found: 6650.37. After HPLC purification, the collected fraction was lyophilized.

2.2.4 Reaction of cyclo-RGD with molecular linkers

A solution of cyclo(RGDfC) (4 mM , 10 μL) in a phosphate buffer (0.1 M, pH 8.0) is mixed with **6b** (4 mM, 10 μL) dissolved in phosphate buffer (0.1 M, pH 8.0). The reaction was stirred for three hours at room temperature, monitored by MALDI mass spectrometry for its completion. The conversion was 99.5%, determined by HPLC analysis. The product was purified by HPLC using a Zorbax Eclipse Plus C18 column (4.6 x 150 mm, particle size 5 μm) under a gradient of 20% to 70% over a period of 25 mins (Solvent A: 0.1% trifluoroacetic acid in de-ionized water; Solvent B: 0.09% trifluoroacetic acid in 80:20 acetonitrile: De-ionized Water; injection volume: 14 μL), monitored with a UV detector at a wavelength of 230 nm. The conjugate **P-1b** was eluted

out at retention time of 17 min. MALDI-MS: *m/z* (M+H) calculated for **P-1b**: 2325.72; found: 2325.81.

P-1a was prepared in the same way as did **P-1b**, purified by RP-HPLC, and characterized by MALDI-MS. MALDI-MS: *m/z* (M + H) calculated for **P-1a**: 1268.57; found: 1268.49. The conversion of peptide to its conjugate was quantitative. Both **P-1a** and **P-1b** fractions were lyophilized after HPLC purification.

2.2.5 Functionalization of silicon substrates

Reactions i-a and i-b in Scheme 3: A silicon substrate (1 x 1 cm^2) was cleaned thoroughly with ethanol, dried by nitrogen, and then treated with oxygen plasma for two minutes using Harrick Plasma Cleaner (medium power). APTES was deposited on the substrate using a vapor deposition method.[2] The aminated substrate was immersed in a solution of compound **2** (1 mg/mL), NHS/EDC (1 mg each) and triethyl amine (5 μL) in dry dicholoromethane. After three hours, the substrates were taken out and rinsed with dry dichloromethane (twice) followed by ethanol (twice) and dried with argon.

Reaction ii in Scheme 3: A silicon substrate (1 x 1 cm^2) was cleaned as mentioned above, and then immersed in an aq. solution of silatrane derivative **3 (**50 mM). After one hour, the substrates were taken out and rinsed five times with deionized water and dried with argon.

2.2.6 Characterization of the monolayers

Contact angles were measured using Kruss EasyDrop. For the measurement, 2 μL of water droplets were deposited on different positions of a substrate placed on the sample plate and contact angles were measured in the video window of manufacturer's DSA software.

Thicknesses of the monolayers were measured using Gaertner Scientific Corporation ellipsometer. For the thickness calculation, the refractive indices of both silicon oxide layers and organic layers were assumed to be 1.46.[3] Five different arbitrary positions on the substrate were chosen and the average value was taken. The thickness of the monolayer was determined by subtracting the silicon oxide thickness from the measured one.

2.3 Results and discussion

2.3.1 Synthesis

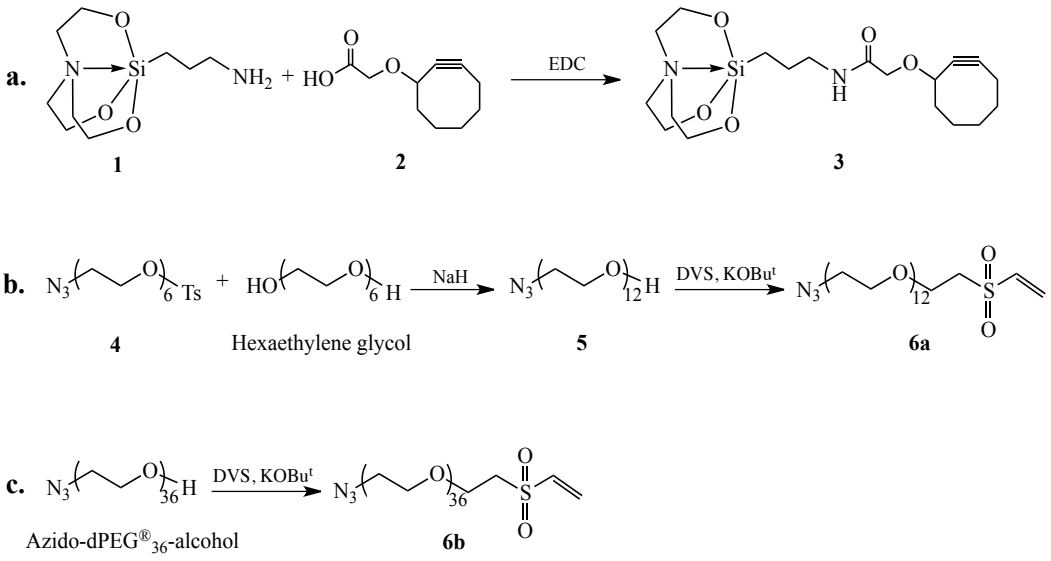

Scheme 1. Schematic diagram of chemical syntheses

The molecular anchor (**3**) was synthesized simply by reacting APS (**1**) (83) with 2-(cyclooct-2-yn-1-yloxy)acetic acid (**2**) (85) in the presence of 1-ethyl-3-(3-dimethylaminopropyl)carbodiimide (EDC, Scheme 1-a). The desired product was separated as a white solid by silica gel chromatography with a yield of 60% (see Supporting Information for details). The molecular linker for RI (**6a**, Scheme 1-b) was

synthesized starting from hexaethylene glycol. First, azido-$(CH_2CH_2O)_6$-Ts (**4**, Ts = tosyl) was synthesized in a multi-gram scale following a method reported in literature.(90,91) The azido-$(CH_2CH_2O)_{12}$-H (**5**) was prepared in a 71% yield by reacting **4** with sodium hexaethylene glycoxide (3 times excess) that was generated *in situ* by treating hexaethylene glycol with sodium hydride. In presence of potassium *t*-butoxide, **5** reacted with divinyl sulfone to furnish the desired product **6a** in a fairly good yield (64%). In the same manner, the linker azido-$(CH_2CH_2O)_{36}$-vinyl sulfone (**6b**) was synthesized by reacting azido-dPEG$^{®}_{36}$-alcohol with divinyl sulfone in a yield close to that of **6a** (Scheme 1-c). These two products were characterized with FTIR, NMR, and mass spectroscopy (see supporting information). Although it has been reported that vinyl sulfones react with azides in presence of $CuSO_4$ and sodium ascorbate (92), we found by NMR monitoring that **6a** and **6b** were stable both in its pure form and in chloroform at room temperature at least for two days. They have been stored at -78°C already for one year and no degradation has been observed. Maleimide is another widely used reactive group that functions similarly to vinyl sulfone in bioconjugation (93), but it may not be amenable to coexisting with azide because a [3 + 2] cycloaddition could spontaneously take place between these two functions in some circumstances (94). In addition, maleimide can undergo the thiol exchanges and ring hydrolysis (above pH 8) (95,96), which would complicate outcomes of the conjugating reaction. It is also a reason why we chose vinyl sulfone as a Michael addition receptor of thiols in our attachment chemistry (88).

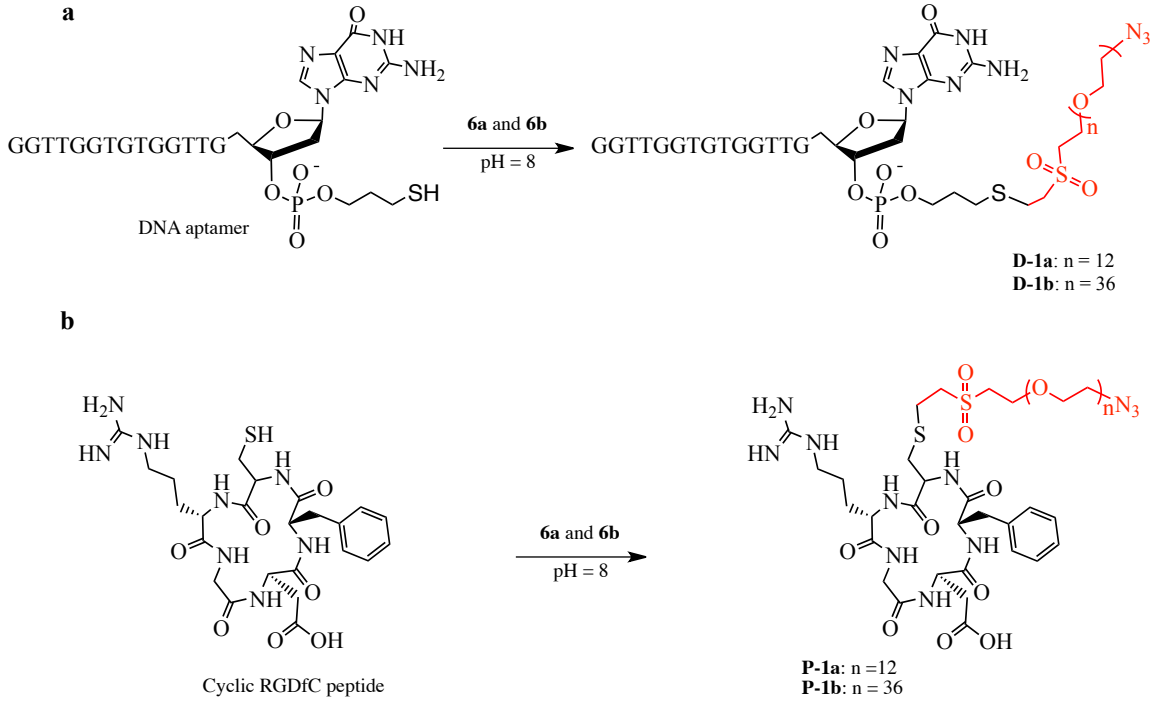

2.3.2 Click 1: Attaching molecular linkers to affinity molecules:

Scheme 2. Scheme for attaching linear linkers to affinity molecules

Two affinity molecules, thrombin-binding DNA aptamer (TBA) (97) and cyclic RGDfC peptide containing a RGD motif that binds to integrin receptors such as $\alpha_5\beta_1$ (98), were chosen to study the attachment chemistry. First, the disulfide at the 3'-end of the DNA aptamer from custom synthesis was reduced to thiol using tris(2-carboxyethyl)phosphine (TCEP), which then reacted with linker **6a** and **6b** at pH 8.0 in phosphate buffered aqueous solutions, respectively. Through the Michael addition of thiol to vinyl sulfone (Scheme 2-a), the DNA aptamer was converted to azido-PEGylated products **D-1a** with a 95% yield and **D-1b** with 89% yield, based on HPLC analysis (see Supporting Information). The disulfide DNA was used as a negative control and it did not react with

6a and **6b,** implying that the vinyl sulfone is specific to thiol under the current conditions. Also, we observed that the reaction between the vinyl sulfone and the thiolated DNA at pH 7 – 7.5 was very slow and did not complete even after one day. The thiol reaction is driven by the thiolate that is a much stronger nucleophile than its conjugate acid thiol. Since the alkylthiol is fairly acidic with pK_a of about 10 to 11, the increase of pH surely increases existence of the thiolate anion, resulting in an increased reaction rate. This is consistent with what has been reported in literature (99). Under the similar conditions, the thiolated RGDfC was converted to products **P-1a** and **P-1b** quantitatively (Scheme 2-b). We did not observe any side products by MALDI mass spectrometer and reverse phase HPLC analysis. In addition, no apparent time differences between reacting with **6a** and **6b** were observed. In sum, all these reactions were completed within three hours when starting with DNA or peptides in a range of millimolar concentrations.

It should be noted that the vinyl sulfone also reacts with alkyl amines under basic conditions (100). In our case, the amine functionalized aptamer and the cyclic RGDfK reacted with both **6a** and **6b** in phosphate buffered solutions at pH 8.8, but the reactions were very slow and not completed even after ten hours. This shows that the vinyl sulfone can specifically react with thiol in the presence of amino function with well-tuned pH.

2.3.3 Click 2: Tethering affinity molecules to AFM tips

At present, there is no effective way to directly monitor chemical reactions and characterize their products on AFM tips. To have insights into our new attachment chemistry, we first carried out a pilot study on planar thermally oxidized silicon substrates, presumably the surface of which has a chemical reactivity similar to that of silicon AFM tips.

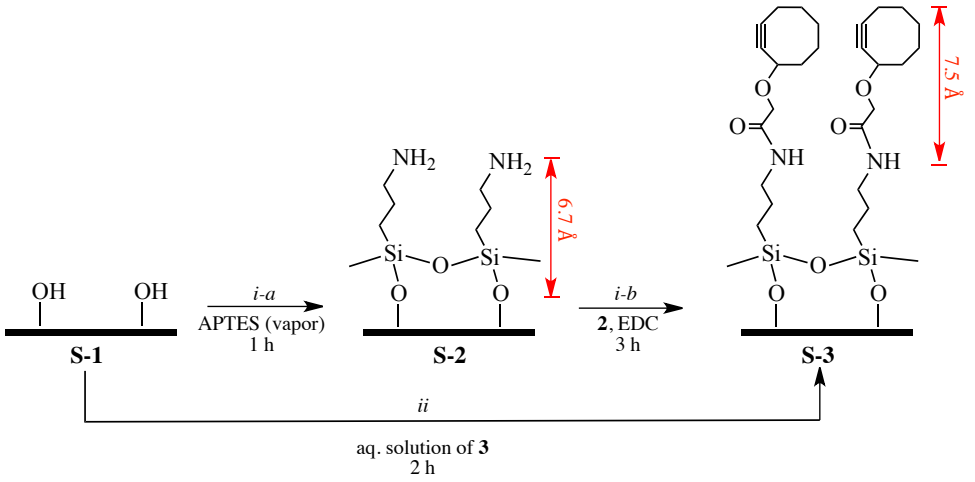

Scheme 3. Functionalization of SiO_2 surface. i-a) vapor deposition of APTES, i-b) coupling of compound 2 to the APTES surface in DCM, ii) reacting with compound 3 in aqueous solution. The numbers in red are estimated molecular length from ChemDraw 3D modeling

We found that compound **3** formed a monolayer with its physical properties close to those of the monolayer generated by reacting cyclooctynyloxy-acetic acid **2** with the APTES functionalized silicon substrate. As illustrated in Scheme 3, when APTES was deposited on a silicon oxide surface by chemical vapor deposition (route i-a), it changed the contact angle of water on the surface from 0° to ~ 46° (Table 1), a value that is consistent to data reported in literature (101). The measured thickness of the organic layer was about 7.3 Å, slightly larger than the calculated distance from nitrogen to oxygen of APTES (see S-2 in Scheme 3), indicating formation of a monolayer (See Supporting Information for details about contact angle and thickness measurement). Treating the APTES monolayer with compound **2** in the presence of EDC increased the contact angle to ~76° and thickness to ~15.9 Å, close to the expected value (see S-3 in Scheme 3).

When the same silicon substrates were treated directly with an aqueous solution of compound **3** (route ii in Scheme 3), the measured contact angle and thickness were ~78° and 15.3 Å, respectively, well matching with those data just mentioned above. This indicates that compound **3** may form a monolayer with a structure as suggested in S-3. In turn, we treated the cyclooctyne surface with a solution of fluorescent TBA containing an azide at its 3'-end and it became highly fluorescent after one hour incubation, whereas the same surface treated with the fluorescent aptamer containing disulfide at the 3'-end (negative control) had negligible fluorescence. Note that we had confirmed that the azide functionalized TBA and cyclo-peptides reacted with the cyclooctyne effectively in the liquid phase (monitored by MALDI mass) before applying them to silicon substrates or tips.

Table 1. Physical properties of surfaces derivatized with chemical functions

	Contact Angle (°)	Thickness (Å)
S-2 (Route i-a)	45.8±0.9	7.3±0.3
S-3 (Route i-b)	75.8±0.8	15.9±0.5
S-3 (Route ii)	77.9±1.2	15.3±0.3

Based on the study above-mentioned, we have developed a two-step protocol for the attachment. As illustrated in Figure 18, a bare AFM tip is first functionalized with the molecular anchor **3** in aqueous solution, followed by reacting with the azide functionalized affinity molecules under physiological conditions (see Experimental Section). It is worth noting that all the reactions were carried out in aqueous solutions without using any of organic solvents. The reaction between cyclooctyne and azide may

yield two regioisomeric triazoles (102), but it will be challenging for us to confirm their existence on the AFM tip with currently available analytical tools. However, we have not observed any apparent regioisomeric effects on the following AFM measurements. The attachment chemistry has worked well on two different AFM tip materials: SiN tipped probes (from Olympus and Bruker) and silicon probes (from NanoWorld). Before the chemical functionalization, these tips were cleaned sequentially with UV-ozone and oxygen plasma to increase the silanol density on the silicon surface for the silanization reaction.

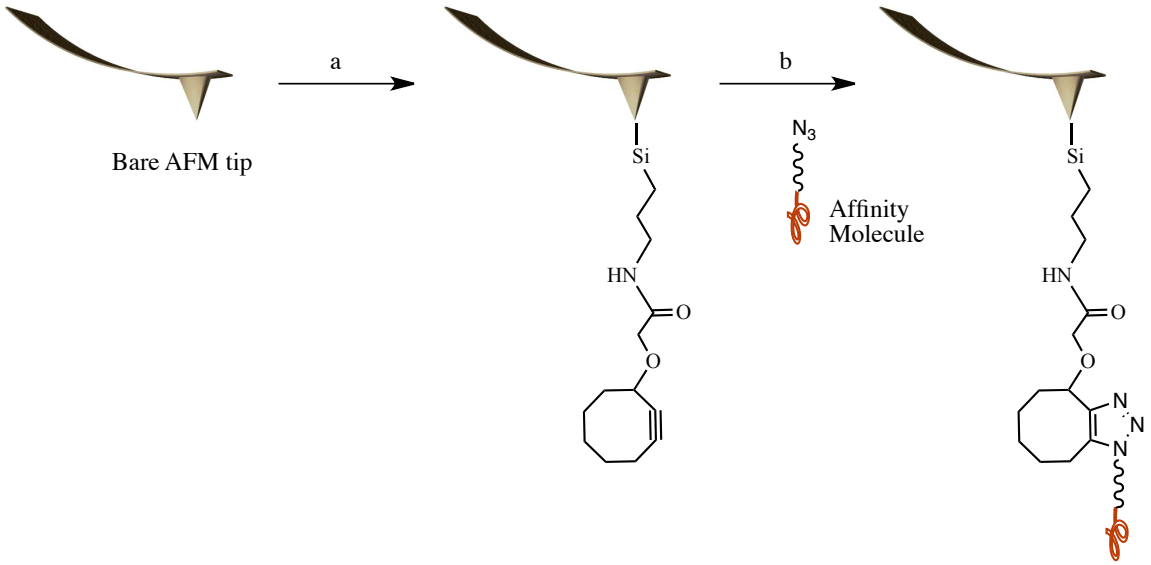

Figure 18. Process of functionalization of AFM tip with affinity molecules. a) coupling cyclooctyne to an AFM tip through silanization, b) tethering affinity molecules to an AFM tips through an alkyne-azide click reaction

2.3.4 Force Measurement

The attachment chemistry was validated by measuring forces of affinity molecules tethered to SiN tips unbinding from their protein cognates. The protein samples were immobilized on APS-modified mica substrates using glutaraldehyde as a

crosslinker according to a procedure reported in literature (54). Initially, we collected about 1000 force-distance curves from each of measurement experiments with either **D-1b** against thrombin or **P-1b** against integrin $\alpha_5\beta_1$.

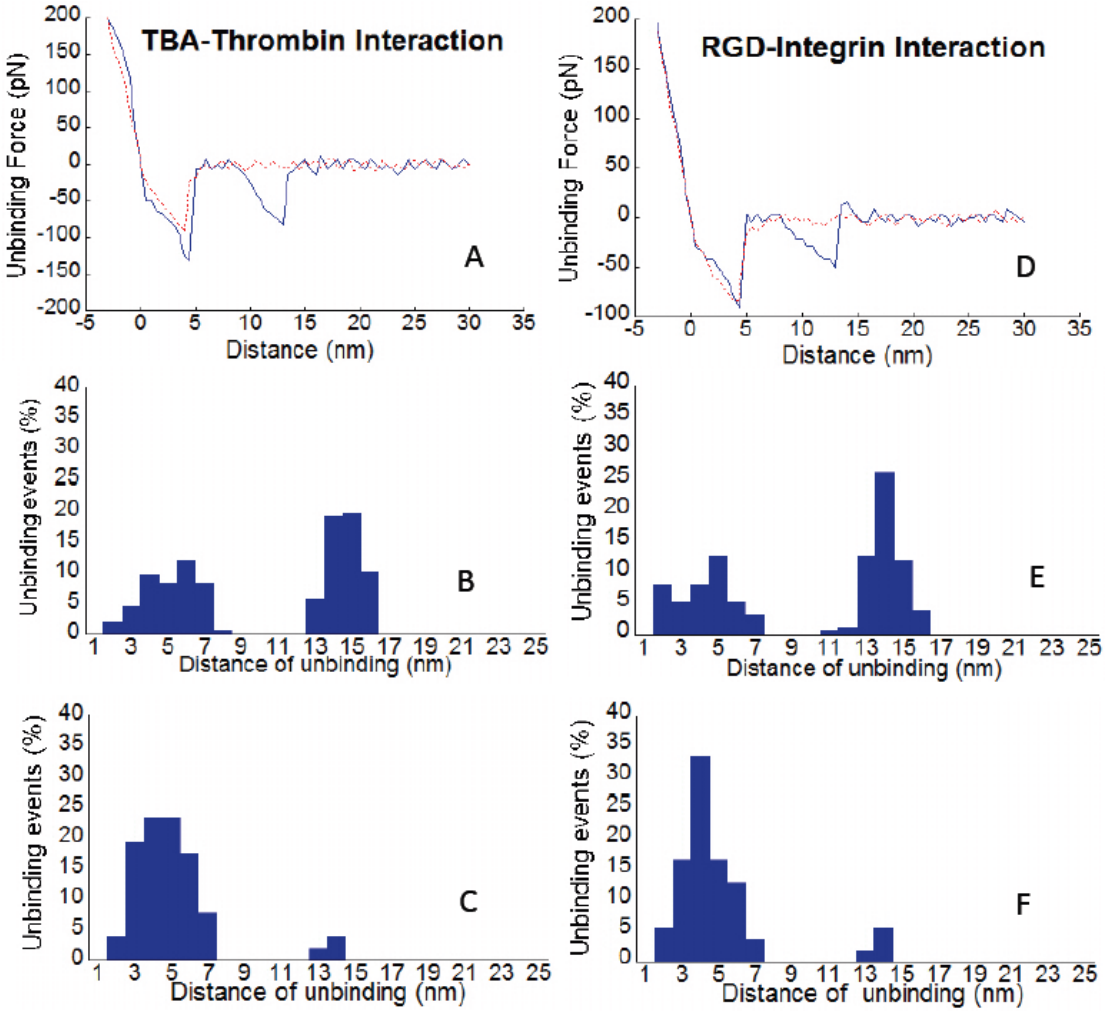

Figure 19. (A) Force distance curve for TBA aptamer-thrombin unbinding; (B) A distance histogram of the ruptures for thrombin; (C) distance histogram of the ruptures after blocking the TBA tip with thrombin; (D) Force distance curve for RGDfC peptide-integrin unbinding (E) A distance histogram of the ruptures taking place with the RGD functionalized tip retracting from the surface; (F) A distance histogram of the ruptures taking place after blocking the RGD tip with integrin.

The blue solid lines in Panel A and D of Figure 19 show typical retracting force-distance curves we used for data analysis, which accounts for more than one forth of the collections. The selection was based on an assumption that a rupture directly related to unbinding of an affinity molecule from its protein cognate is likely to take place around the distance corresponding to the stretched length of a PEG linker (~ 13.5 nm in our case). A distance histogram was created from each data set (Panel B and E of Figure 19). They show that the unbinding events were mainly distributed in the regions of 2-7 nm and 13-16 nm. Ratios of the rupture events between these two regions were 1 : 1.2 for the TBA tip against the thrombin and 1 : 1.3 for the RGD tip against the integrin respectively. After finishing each of the initial measurements, a thrombin or integrin solution was injected to the flow cell accordingly, and then another set of force curves were collected to determine the specificity of unbinding (103). We expected disappearance of the specific unbinding ruptures from the force-distance curves because the interactions of the affinity molecule tethered to the tip with its cognates on the substrate were blocked by protein from the solution. In fact, we obtained force-distance curves appearing like those red dotted lines in Panel A and D of Figure 19. Overall, the ruptures around the longer distances were reduced to a great extent and those around the shorter distances remained (Panel C and F of Figure 19) in comparison with those prior to blocking. The rupture ratios between these two regions were changed to 12.3 : 1 for the TBA tip against the thrombin modified surface and 12 : 1 for the RGD tip against the integrin modified surface. To best interpret these results shown in Panel B and E of Figure 19, we assigned the rupture events occurring at the distance around ~ 13.5 nm as specific unbinding of the affinity molecule from its protein cognate and those events in

the range of 2 to 7 nm are a consequence of multi-molecular interactions and unraveling that do not involve stretching of the PEG linker between the surface and the tip.

In total, there were 26.5 % of force-distance curves containing the specific ruptures of TBA unbinding from thrombin in the initial collection. They were plotted as a force histogram and fitted into a Gaussian function, yielding a curve with the peak at ~ 80 piconewton (pN) (Panel A of Figure 20). Similarly, 29.4 % of the initial force-distance curves showed the specific unbinding ruptures for the RGD-integrin interactions, which results in a Gaussian curve with the peak at ~ 48 pN (Panel B of Figure 20). These unbinding force data were comparable with those reported in literature (104,105).

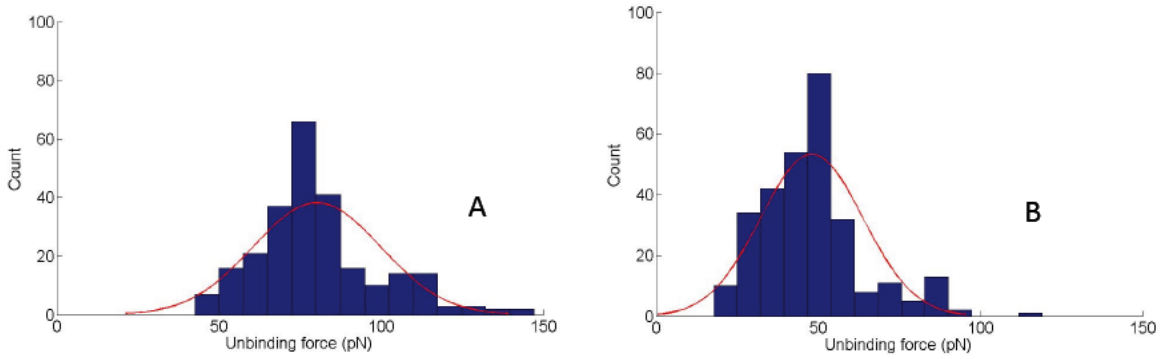

Figure 20. (A) A force histogram of TBA unbinding from thrombin immobilized on the mica surface; (B) A force histogram of RGD unbinding from integrin immobilized on the mica surface.

We further examined the non-specific interactions between functionalized AFM tips with both bare and bovine serum albumin (BSA) immobilized mica substrates. The results are given in Table 2. In summary, the functionalized AFM tips generally formed featureless force-distance curves on these surfaces. Only 6.1% of collected curves show

unbinding ruptures from the nonspecific TBA-BSA interaction (median force 14.4 pN) and 5.6% from the nonspecific RGD-BSA interaction (median force 15.3 pN) around the expected distance, respectively. The functionalized tips interacted with the bare mica surfaces with even lower statistics and smaller unbinding forces. All of non-specific unbinding forces we measured were significantly smaller than those specific ones. These data demonstrate that our attachment chemistry has effectively tethered affinity molecules to AFM tips as well as maintained their specificity.

Table 2. Statistical data of functionalized AFM tips interacting with varied surfaces based on force-distance curves

On the tip	On the substrate	Unbinding events (%)*	Unbinding force (pN)
TBA	Thrombin	26.5	80.2±34.5
TBA (blocked)	Thrombin	7.0	15.6±12.9
TBA	BSA	6.1	14.4±9.4
TBA	Bare mica	3.0	6.9 ±3.8
RGD	Integrin	29.4	48.0 ± 27.8
RGD (blocked)	Integrin	6.7	11.1±10.7
RGD	BSA	5.6	15.3±14.4
RGD	Bare mica	2.5	6.7±4.0

* The percentage of ruptures taking place around the specific unbinding distance over total collected force curves.

2.3.5 Recognition Imaging (RI)

The AFM based recognition imaging has great potential to be an effective tool for clinical diagnostics. It is important for us to confirm that our chemistry works with the RI technique. Unexpectedly, the recognition imaging of clinically relevant proteins thrombin and integrin has not been reported. It has been demonstrated that a PEG linker with 12 ethyleneoxy (CH_2CH_2O) units can effectively produce quality recognition images (69). Linker **6a** was tailored for RI. Its conjugate **D-1a** or **P-1a** was attached to Ni-coated MacMode tips (from Nanoworld) following the same protocol above mentioned. The protein samples (thrombin or $\alpha_5\beta_1$ integrin) were deposited on mica using the same glutaraldehyde chemistry. However, the optimal protein concentration (50 pg/μL in 1X PBS buffer, pH 7.4) for the RI was 20 times lower than that for the force measurements, which was pre-determined by imaging the surface with bare AFM tips in the air mode, ensuring that the protein molecules were well distributed in a predefined area. For one measurement, only 2-3 μL of protein sample is needed in the current setup. Thus, a few femtomoles of proteins can readily be detected by the AFM based recognition imaging. Figure 21 shows the images obtained from our RI experiments. In general, RI simultaneously produces both topographic and recognition images. Each bright round spot in the topographic image presumably represents a protein molecule (thrombin in Panel A and integrin in panel D of Figure 21). This can be verified by examining the recognition images (Panel B and E of Figure 21) where the dark spots represent recognition of those bright ones within the corresponding locations in the topographic image as expected protein molecules. We obtained about 77% recognition of thrombin

and 84% recognition of integrin by comparison between their topography and recognition images. The recognition was further confirmed by the same blocking experiments as in the force measurements. After injecting a protein (thrombin or integrin) solution to the flow cell, most of the dark spots disappeared from the recognition images (Panel C and F of Figure 21). These experiments demonstrate that our attachment chemistry works effectively for RI as well.

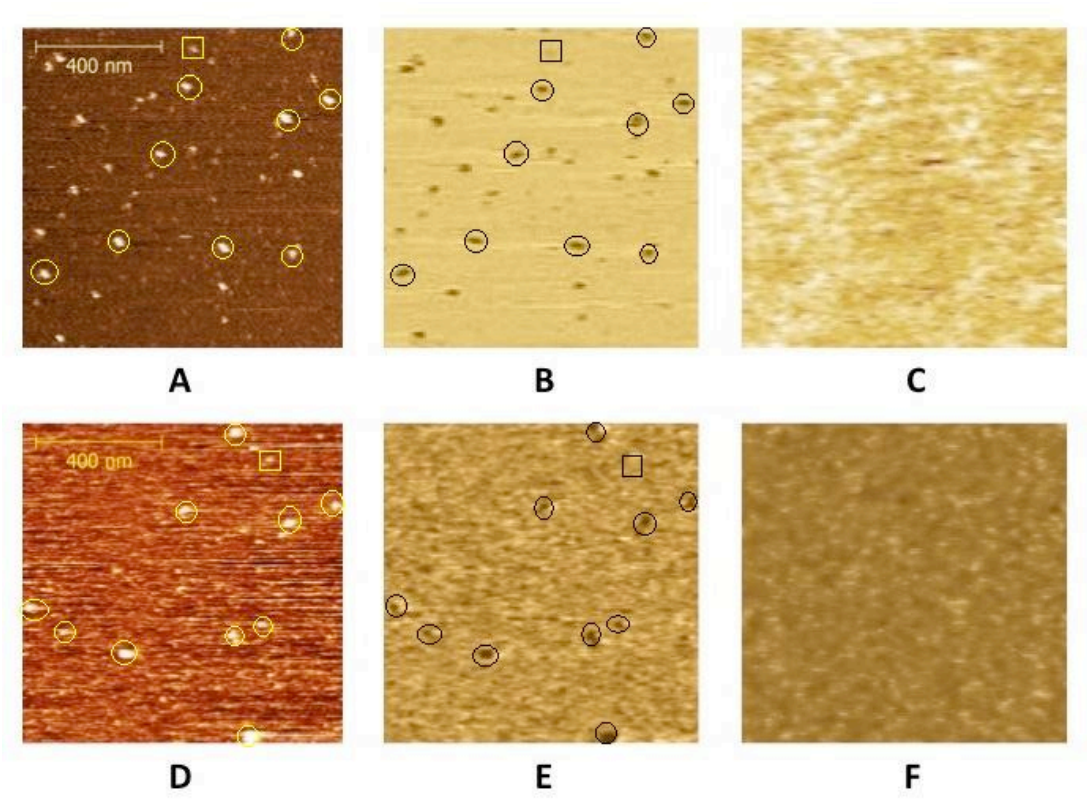

Figure 21. (A) Topographic image of thrombin proteins on mica; (B) Corresponding recognition image of A; (C) a recognition image from using a thrombin solution to block the TBA tip; (D) Topographic of integrin proteins on mica; (E) Corresponding recognition imaging of D; (F) a recognition image from using a integrin solution to block the RGD tip; (the circles in the images indicate those protein molecules that were recognized whereas the square indicates the protein that was not recognized)

2.4 Conclusion

We have developed a new scheme to attach affinity molecules to AFM tips for force spectroscopy and recognition imaging, based on two orthogonal click chemistries: catalyst free azide-alkyne cycloaddition and thiol-vinyl sulfone Michael addition. All the reactions can be carried out in aqueous solutions without the use of organic solvents. We synthesized two new reagents for this implementation. The first one is an APS derivative of cyclooctyne for introduction of a chemically reactive group to AFM tips. The silatrane chemistry allows for the formation of a uniform monolayer in aqueous solution, which is particularly useful when the chemical is not volatile and the vapor deposition would not work. The operation is more convenient compared to the vapor deposition technique and the resulting surface is highly reproducible. The second one is a class of heterobifunctional linkers with a form of "azido-PEG-vinyl sulfone". Our data show that it works for both AFM based force measurement and recognition imaging. The attachment process is easy to follow since there are no special requirements for the chemical reactions. With an increasing number of affinity oligonucleotides and peptides, more and more proteins will be detected with these synthetic materials. Incorporating thiol to peptides and oligonucleotides has become a routine process in custom synthesis. Hence, our attachment method should be applicable to a broad range of affinity molecules.

CHAPTER 3

DUAL RECOGNITION IMAGING USING AN AFM TIP FUNCTIONALIZED WITH A TRI-ARM LINKER

3.1 Introduction:

Atomic force microscopy **(**AFM) can be used to identify proteins or other biomolecules immobilized on a surface using its tips functionalized with affinity molecules with high resolution. However, many events in biochemistry need to determine the co-location of multiple factors, and this is not possible with only one type of affinity molecule on an AFM probe. To apply the AFM technique to simultaneous detection of multiple analytes, we designed a three-arm scaffold for connecting two different affinity molecules for their attachment to an AFM tip. In this study, we synthesized a tri-arm linker carrying and an aptamer and cyclic peptide. The molecule was attached to AFM tips through a catalyst-free click reaction. Our imaging results show that the molecular duo specifically recognized its respective cognates during AFM scanning. The AFM method is sensitive, needing only 2-3 μL of protein solution with a concentration of ~ 2 ng/mL for each experiment. The ratio of two proteins on the surface determined by the AFM method is close to one in the sample solution. Thus this new approach has the potential to be a single molecule, label-free detection system particularly for those low abundance protein biomarkers.

AFM—a surface imaging tool with nanometer spatial resolution—has being evolved into a molecular nano-biotechniques (106), used in imaging of proteins on solid surfaces and on living cells (107,108), supramolecular assembly (109), and hydrogen bonding complexes (110,111), as well as in measurement of interacting forces between

proteins (112,113), protein and DNA (114), and between ligand and receptor (115,116) at a single molecule level in a physiological environment. With high speed AFM (117), antibodies walking on bacterial surfaces can be monitored on a time scale of 0.01–1 s/step (118). Thus, AFM provides a unique means of detecting proteins with potential applications in proteomics (119) and diagnostics of cancer (120). Meanwhile, chemical sensing by AFM continues to improve with better methods of tip functionalization. For example, when an antibody attached to an AFM tip through a polyethylene glycol (PEG) linker is brought to scan a surface, it will generate a map of the location of antigens because of the specific intermolecular interactions, a technique known as Recognition Imaging, which has been extended to epigenomics for determination of DNA methylation patterns (121). In this regard, a flexible linker increases the recognition efficiency and reduces non-specific interactions. One can conceive of using the recognition imaging for detection of low abundance proteins in a biological sample. Compared to fluorescence microscopy, however, the AFM based recognition imaging lacks a multiplex capacity to measure multiple analytes in a single test. The multiplexities have become increasingly important for molecular diagnostics of diseases in clinics (122).

Figure 22. Functionalization of the AFM with two different antibodies using a 1:1 mixture of the antibodies. Adapted from reference (123)

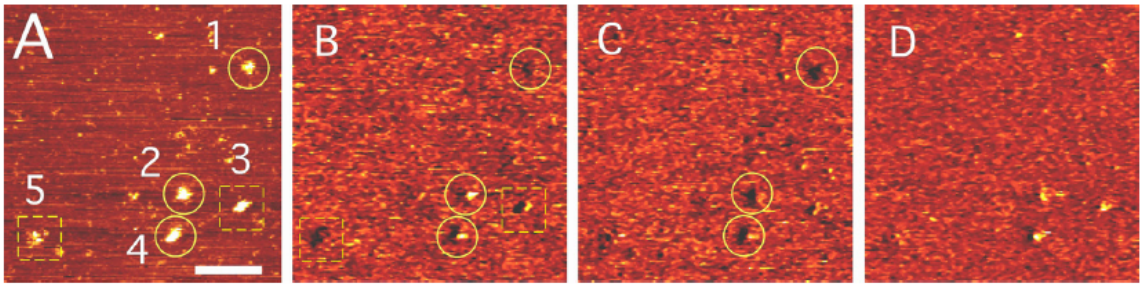

Figure 23. hSwi-Snf complex was deposited on mica and scanned with AFM tip containing anti-BRG1 and anti-β-actin antibodies. A) Initial topographic image, B) recognition events without any blocking peptide, C) recognition after blocking with anti-β-actin antibodies, D) recognition in presence of both anti-BRG1 and anti-β-actin antibodies. Similar studies were performed using a 1:1 mixture of anti-H2A and anti-H2B antibodies. Adapted from reference (123)

Wang *et al* reported that an AFM tip functionalized with a mixed solution of two different antibodies could recognize multiple analytes by first scanning to generate a map of both targets, followed by second scanning of the same area with one of the antibodies blocked; by comparing these two scans, the location of each type of protein can be determined (figure 22 and 23) (123). Nonetheless, this approach is very difficult to be reproducible, relying on the chance functionalization of the apex of an AFM tip by two different antibodies. Here, we address the issue of ensuring that two different affinity molecules are equally attached to the AFM tip in terms of their numbers and positions so that they can contact their respective cognates with an equal probability. To do this, we have developed a linkage chemistry to form a complex we refer to as "molecular duo", which is composed of two affinity molecules that are connected together by a three-arm linker, for tethering two different types of molecules to the AFM probe. As illustrated in

Figure 24, when the AFM tip carrying a molecular duo scans across a surface covered with proteins, the two affinity molecules will be bought to interact with their respective cognates so that a recognition image of both targets can be generated. A second scan over the same area, made after blocking one of the recognition molecules will allow us to distinguish between the two targets.

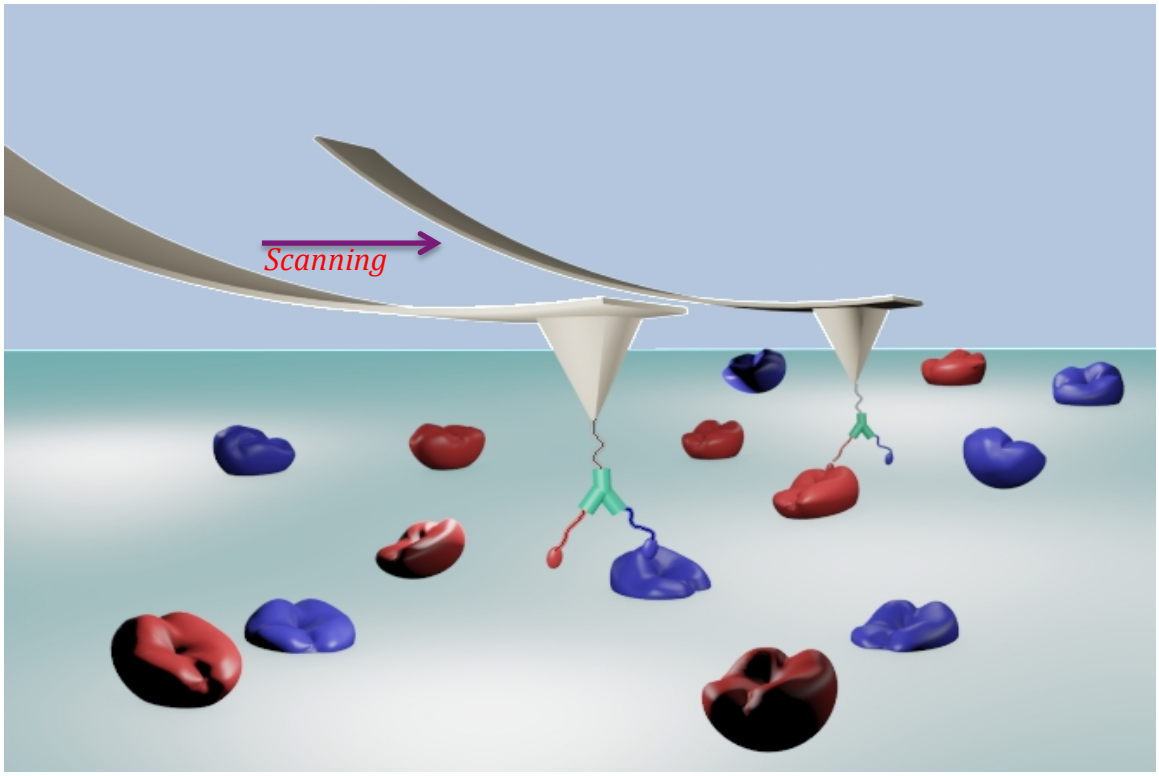

Figure 24. Illustration of multiplex recognition imaging with an AFM tip functionalized with two affinity molecules through a three-arm linker (molecular duo).

3.2 Materials and Methods

3.2.1 General information

All reagents and solvents were purchased from commercial suppliers (Sigma-Aldrich, Alfa Aesar, Fluka, TCI America) and used as received unless otherwise noted. All experiments requiring anhydrous conditions were performed in flame-dried glassware

under nitrogen atmosphere. Reactions were monitored by thin layer chromatography (TLC) using glass plates precoated with silica gel (resource). ^{1}H NMR and ^{13}C NMR spectra were recorded on either Varian INOVA 400 (400 MHz) or Varian INOVA 500 (500 MHz) spectrometers at 25°C. Chemical shifts (δ) are given in parts per million (ppm) and referenced to the residual solvent peak ($CDCl_3$: δ_H = 7.26 ppm, CD_3OD: δ_H = 3.31 ppm, DMSO-d_6: δ_H = 2.50 ppm). Coupling constants (J) are expressed in hertz (Hz) and the values are rounded to the nearest 0.1 Hz. Splitting patterns are reported as follows: br, broad; s, singlet; d, doublet; dd, doublet of doublets; t, triplet; dt, doublet of triplets; q, quartet and m, multiplet. High resolution mass spectra (HRMS) were acquired at the Arizona State University CLAS High Resolution Mass Spectrometry Facility. Flash chromatography was performed in an automated flash chromatography system (CombiFlash R_f, Teledyne Isco, Inc.) with silica gel columns (60-120 mesh). RP-HPLC analysis and separation were performed with a Zorbax C-18 column (4.6 x 150 mm, particle size 5 μm) in an Agilent 1100 HPLC equipped with UV monitor and fraction collector.

Integrin was bought from Yo proteins AB (Sweden), a lyophilized product from a solution containing 0.26 mg/mL $\alpha_5\beta_1$, 20 mM Tris-HCl pH 7.5, 150 mM NaCl, 2 mM MgCl2, 0.2% Triton X-100. They were reconstituted by dissolving in water before use according to manufacture recommendation.

Recognition imaging was performed on Agilent's MacMode AFM equipped with a PicoTREC system. Silicon Tips purchased from NanoWorld were used for recognition imaging. The cantilever was made having length of 125 μm, width 35 μm and thickness

800 nm with a force constant of 0.14 N/m. Its backside was coated with 1 nm Ti/40 nm Ni.

3.2.2 Synthesis

1-Azido-35-tosyloxy-3n$_{33}^{3}$-undecaoxapentatriacontane (S2): Tosyl Chloride (TsCl, 1.67g, 8.76mmol) is added to a solution of 35-azido-3n$_{33}^{3}$-undecaoxapentatriacontan-1-ol (2.5g, 4.38 mmol) and triethylamine (Et_3N, 3 mL, 21.53 mmol) in anhydrous dicholoromethane (DCM, 15 mL) under nitrogen. The reaction mixture was stirred at room temperature for 12 h. The solvent was removed by rotary evaporation. The residue was purified by silica gel column chromatography using a gradient of 3.5% methanol in Dichloromethane to give the product as a colorless liquid (2.86g, 90% yield). ^{1}H NMR (400 MHz, $CDCl_3$): δ 2.97 (s, 3 H); 3.37 (t, 2 H, J = 5.2 Hz); 3.575-3.3.689 (m, 44 H); 4.505 (t, 2 H, J = 4.8 Hz); 7.35(d, 2H, J = 8 Hz); 7.79(d, 2 H, J = 8 Hz); **^{13}C NMR** (100MHz, $CDCl_3$): δ 144.71, 132.920, 129.756, 127.851, 70.605-70.404, 69.920, 69.206, 68.543, 50.568, 21.539, HRMS: m/z (M+H) Found 726.33 (M+H); Calc. 725.23 (M);

1-Azido-35-((4-iodobenzyl)oxy)-3n$_{33}^{3}$-undecaoxapentatriacontane (8). Potassium-*tert*-butoxide (KO^tBu, 482.5 mg, 4.3 mmol) was added to a solution of **S2** (2 g, 2.76 mmol) and *p*-iodobenzylalcohol (0.84 g, 3.59 mmol) in anhydrous tetrahydrofuran (4 mL) under nitrogen. The mixture was stirred at room temperature for 2 h, cooled down in an ice bath, and quenched by the addition of methanol (2 mL). The compound was purified using a gradient of 3.5% methanol in dichloromethane to obtain compound 1g as yellowish oil (1.85g, 85% yield). ^{1}H NMR (400 MHz, $CDCl_3$): δ 3.301 (t, 2H, J = 5.2 Hz); 3.565-3.582 (m, 46H); 4.423 (s, 2H); 7.02 (d, 2H, J = 8Hz); 7.57 (d, 2H, J = 8.4 Hz); ^{13}C NMR (100MHz, $CDCl_3$): δ 138.004, 137.259, 129.451, 92.838, 72.317, 70.538-

70.404, 69.905, 69.496, 50.538; MALDI-MS: Found 788.84 (M+H), 810.58 (M+Na), 826.55 (M+K); Calc. 787.68 (M).

1,3,5-tris{[4-(1-azido-3n$_{36}^{3}$-dodecoxaheptatriacontyl)phenyl]ethynyl]}benzene (9). 1,3,5-Triethynylbenzene (**1**, 62 mg, 0.41 mmol) and Compound **2** (1.0 g, 1.27 mmol)were mixed with anhydrous tetrahydrofuran (7.5 ml) and triethylamine (7.5 ml) under nitrogen. The solution was degassed by slowly bubbling nitrogen for 10 min, to which bis(triphenylphosphine)palladium(II)dichloride (14.4 mg, 0.02 mmol) and copper(I) iodide (3.9 mg, 0.02 mmol) were added. The mixture was refluxing for 48 h, cooled to room temperature, and filtered. The solvent was removed by rotary evaporation. The residue was separated by silica gel column chromatography with a gradient of 4% methanol in dichloromethane (gradient time). The product **9** was obtained as a yellowish oil (307 mg, 35%). ^{1}H NMR (400 MHz, $CDCl_3$): δ 3.36 (t, J = 5.2 Hz, 6H, N_3CH_2); 3.62-3.68 (m, 138H, OCH_2CH_2O); 4.58 (s, 6H, $ArCH_2$); 7.33 (d, J = 8.4 Hz, 6H, ArH); 7.49 (d, J = 8.4 Hz, 6H, ArH); 7.62 (s, 3H, Ar'H); ^{13}C NMR (100 MHz, $CDCl_3$): δ = 139.03, 133.97, 131.68, 127.58, 124.02, 121.90, 90.43, 87.75, 72.79, 70.68-70.56, 70.01, 69.66, 50.67. MALDI-MS: Found: m/z 2151.75 (M+Na), 2167.65 (M+K), Calculated: 2128.14.

Synthesis of tri-arm linker (11). A solution of **9** in water (1.0 mM, 30 μL) was added to a solution of ADIBO-cycloRGD in water (0.2 mM, 30 μL). The solution was injected into the HPLC after 1 min. RP-HPLC analysis indicated that the peptide was completely consumed and a new peak appeared at retention time of 25.1 min in the chromatogram under a linear gradient of 20-70% acetonitrile-TEAA buffer (10 mM, pH 7) in 25 min. The mono-addition product **10** was separated using the same gradient as for the HPLC analysis and characterized with MALDI-mass spectrometry. Found: m/z 3050.2 (M + H);

Calculated for formula: 3048.1. **10** (100 μM, 15 μL) was mixed with ADIBO-anti-thrombin (80 μM, 15μL) in water. The reaction was stirred at room temperature for 30 min. The compound **11** was separated by HPLC with a linear gradient of 20-70% acetonitrile-TEAA (10 mM, pH 7). The product had a retention time of 15.1 min and was characterized by MALDI-mass spectrometry. Found: m/z 8349.2 (M + H); Calculated for formula: 8353.9.

3.2.3 Procedure for functionalization of aptamers with ADIBO.

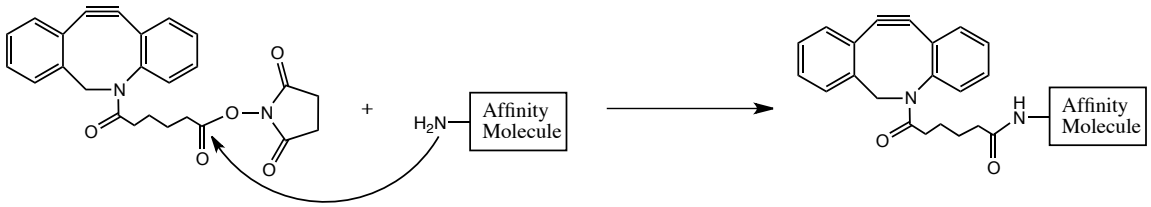

The ADIBO derivatives of aptamers were synthesized by a reaction described in the scheme. In detail, a stock solution of 5'-dodecylamine-modified DNA aptamer in water (1.0 mM, 10 μL) was diluted with a 100 mM phosphate buffer, pH 8.5 (30 μL). The final pH measured 8.4. To the DNA aptamer solution, a DMSO solution of ADIBO-NHS ester (80 μL, 10 mM) was added. The mixed solution was vortexed for 15 min at room temperature and lyophilized. The solid residue was re-dissolved in water (120 μL) and centrifuged. The supernatant that contained the product was separated from the ADIBO precipitate. RP-HPLC analysis indicated that the aptamer was quantitatively converted to its ADIBO derivative. The product was purified using RP HPLC with an eluting system composed of (A) TEAA buffer (10 mM, pH 7) and (B) acetonitrile. The mobile phase started at 90% eluent A and 10% eluent B, linearly increasing to 60% eluent B in 25 min, followed by increasing the eluent B to 100% in 5 min. The retention time for the ADIBO derivative of anti-Thrombin aptamer (ADIBO-anti-Thrombin) was 11.6 min. The

collected fractions of the product were lyophilized, reanalyzed with and characterized by MALDI-mass spectrometry: ADIBO-anti-Thrombin MALDI m/z: Found 5307.29; Calculated for $C_{183}H_{230+1}N_{59}O_{99}P_{15:}$ 5305.7

3.2.4 Synthesis of ADIBO derivative of cyclo-RGD

A solution of cyclo-RGDfK peptide in water (1.0 mM, 10 μL) was diluted with a 100 mM phosphate buffer, pH 8.5 (30 μL). To the solution, a DMSO solution of ADIBO-NHS ester (80 μL, 10 mM) was added. The mixed solution was vortexed for 15 min at room temperature, and lyophilized. The solid residue was re-dissolved in water (50 μL) and centrifuged. The supernatant was separated from the ADIBO precipitate. RP-HPLC analysis indicated that the peptide was quantitatively converted to its ADIBO derivative. The retention time in RP HPLC was 12.9 min with a mobile phase started at 80% eluent A and 20% eluent B, linearly increasing to 70% eluent B in 25 min, followed by increasing the eluent B to 100% in 5 min. The ADIBO-RGD derivative was characterized by MALDI-mass and used without any further purification. MALDI-mass m/z: Found 919.8; Calculated for $C_{48}H_{58+1}N_{10}O_9$: 920.0

3.2.5 Attaching molecular duos to AFM tips

AFM tips (a batch of four) were first soaked in ethanol in a petri dish for five minutes, dried with nitrogen, and then treated with oxygen plasma (medium power) for 2 minutes in a Harrick Plasma Cleaner and then with ultraviolet-ozone in a Boekel UV cleaner for 5 minutes. These tips were immersed in an aqueous solution of N-(3-(silatranyl)propyl)-2-(cyclooct-2-yn-1-yloxy)acetamide (**3**, 50 mM) in a petri dish. After one hour, the tips were taken out, rinsed with water thrice, and dried gently with a nitrogen flow. In a humid surrounding, the cyclooctyne functionalized tips were placed in

a petri dish and a molecular duo solution (10 μM, 20 μl) in 1X PBS buffer (pH 7.4) was added to cover all the tips. After one hour, the tips were rinsed thrice with the same buffer and used immediately for AFM measurements.

3.2.6 Protein immobilization

A mica surface was first functionalized following an APTES/glutaraldehyde procedure developed in our laboratory. In general, a protein solution (3 μL) was added to the glutraldehyde-coated mica in a humid chamber, incubated for 30 min, rinsed with a phosphate buffer three times, and used immediately for the AFM studies. For example, a mixed solution (3 μL) of thrombin and integrin (0.01 ng/μL each) was pipetted on the glutraldehyde-coated mica, incubated at room temperature for 30 min, rinsed with a phosphate buffer, and immediately placed on the AFM stage for use.

3.2.7. Recognition imaging

AFM images were obtained by PicoTrec using magnetically (Ni) coated cantilevers in AC (MAC) mode operation. After initial scanning, blocking was done by passing a protein solution ($\alpha_5\beta_1$ integrin, 50 μL, 10 pg/μL in 1X PBS buffer, pH 7.4) through the flow cell and the surface was imaged again after a period of 10 minutes, following by passing second protein (Thrombin, 50 μL, 10 pg/μL in 1X PBS buffer, pH 7.4) through the flow cell. The surface was scanned again after a period of ten minutes.

3.3 Results and Discussion

3.3.1 Synthesis of the three-arm linker

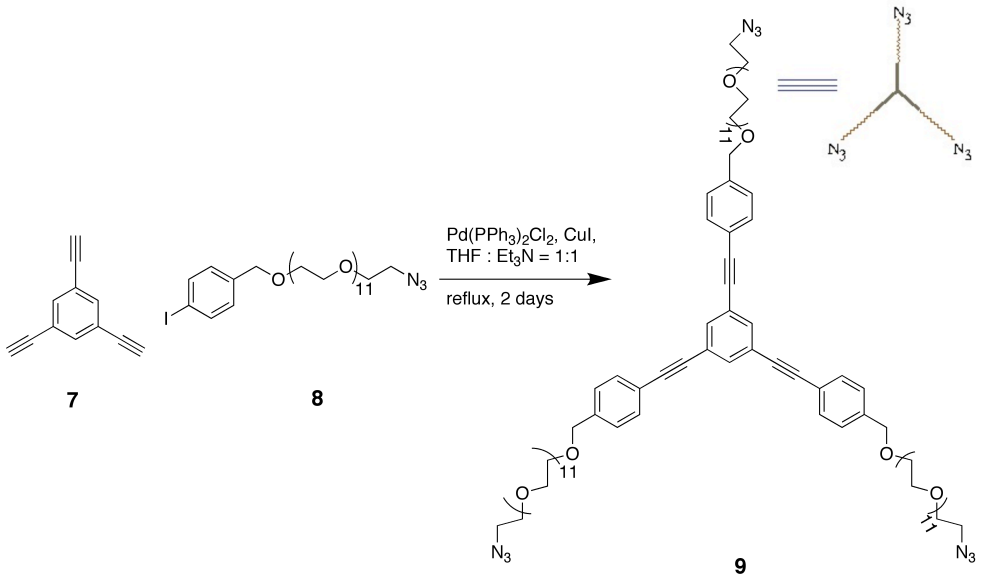

Scheme 5. Reaction for synthesis of the three-arm linker

We designed a C_3 symmetrical linking molecule (**9**, Scheme 5) with azides at its ends. Two of the azide groups were functionalized with two affinity molecules and the third was used for attachment to the AFM tip. Although heterotrifucntional linkers are advantageous for orthogonal bioconjugation (124,125), a homotrifunctional linker has the advantages of simplified synthesis and reduced structural variations in the linkage sites. Compound **9** was synthesized by reacting 1,3,5-Triethynylbenzene (**7**) with 1-azido-37-(4-iodophenyl)-3n_{36}^3-dodecaoxaheptatriacontane (**8**) (126). The product yield was 35% (characterized with NMR, Mass spectrometry and FTIR). The three arm linker is featured by a rigid core (made up of benzene and carbon-carbon triple bond linkages) flanked by three flexible poly[ethylene glycol] (PEG) chains. We used two of its arms to form a molecular duo (affinity molecules) and the third one for its attachment to AFM tips. The azide function was employed for the bioconjugation and attachment through click reactions.

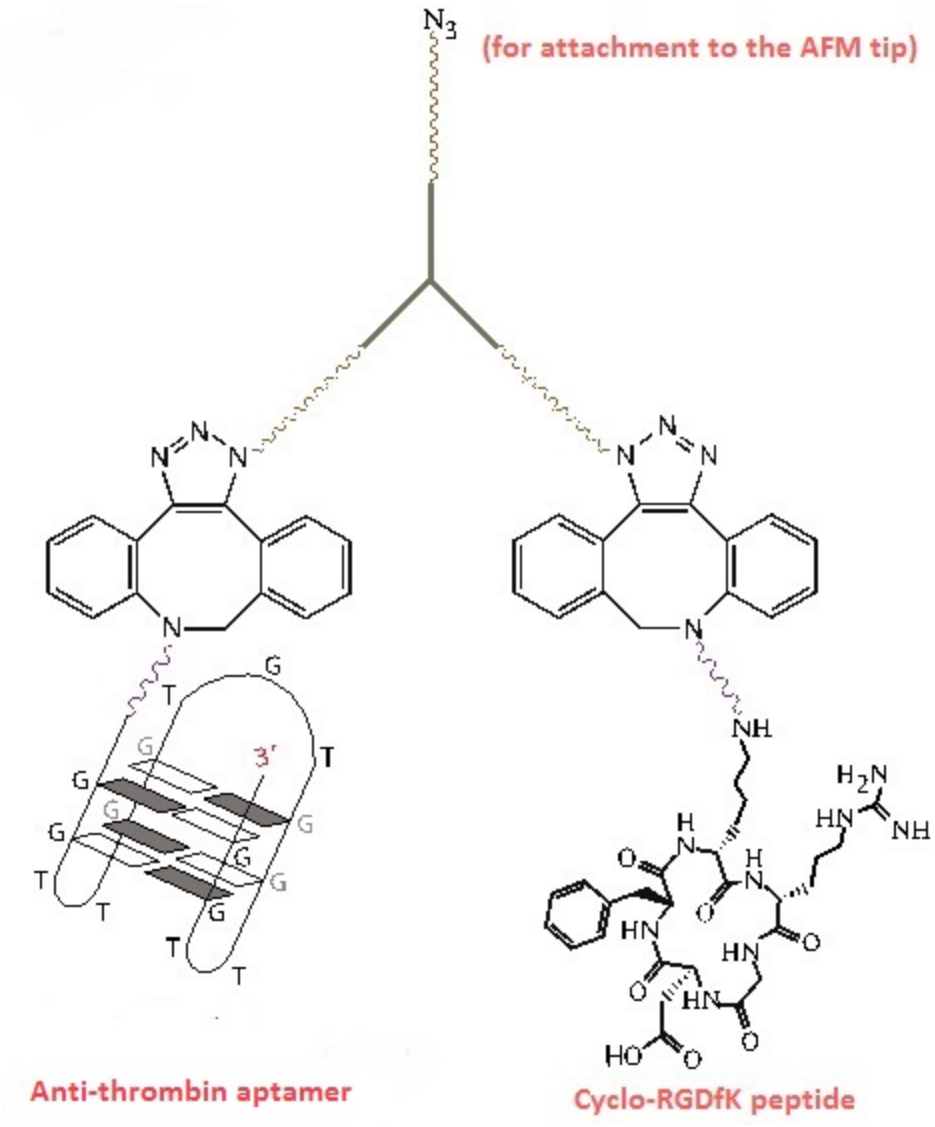

Figure 25. The tri-arm linker (**11**) consisting of two affinity molecules, antithrombin aptamer and cyclo-RGDfK peptide. anti-thrombin aptamer forms a unimolecular quadruplex structure in solution

Recognition imaging normally requires a flexible linker, through which the affinity molecule is tethered to an AFM tip, to keep the AFM tip away from the substrate for most of the measurement period. In general, a PEG chain with 12-18 units of ethylene glycol works effectively in terms of accurately localizing the binding site in a recognition

image (127). In our design, the three arm linker includes both flexible and rigid moieties. We employ tris(phenylethynyl)benzene as a hard core in the center of the linker primarily to avoid the possible collision between two affinity molecules by pointing them to different directions. In addition, the sizable π conjugate increases rigidity of the linker, which should reduce the loss of conformational and rotational entropy caused by binding to the target molecule(s) immobilized on the surface (128). To make it soluble enough in aqueous solutions for bioconjugation, we found that 12-unit PEG chains were required to make the linker more water soluble, and the 6-unit PEG would not be sufficient.

3.3.2 Attachment of affinity molecules

By means of the compound (**9**), we have constructed the tri-arm linker composed of anti-thrombin aptamer (97) and cyclo-RGDfK that binds to integrin receptors (129) (figure 25). These aptamers bind to their respective protein cognates with nanomolar affinities (240 ± 16 for anti-thrombin (130). The cyclo-RGDfK binds to both intergrin $\alpha_5\beta_1$ and $\alpha_v\beta_3$ with IC_{50} of 133 and 2.6 nM, respectively (131). We have demonstrated that both cyclo-RGDfK and antithrombin aptamer can effectively generate recognition images of its cognate protein when attached to AFM tips through a linear linker (132). Compared to antibodies, these affinity molecules are smaller in size and chemically more robust, making them ideal candidates for attachment to tri-arm linker as the molecular duos. We obtained these DNA aptamers containing a dodecylamino chain at their 5'-ends and the cyclo-peptide from commercial sources, and then derivatized them with aza-dibenzocyclooctyne (ADIBO) by reacting with ADIBO-*N*-hydroxysuccinimidyl ester. These products were purified with HPLC and characterized with MALDI mass spectrometry, designated as ADIBO-anti-thrombin, and ADIBO-cyclo-RGD. The

ADIBO group spontaneously reacts with the azide group in aqueous solution known as catalyst-free click addition (133,134), and we used it to anchor the affinity molecules to **9** for formation of the molecular duo.

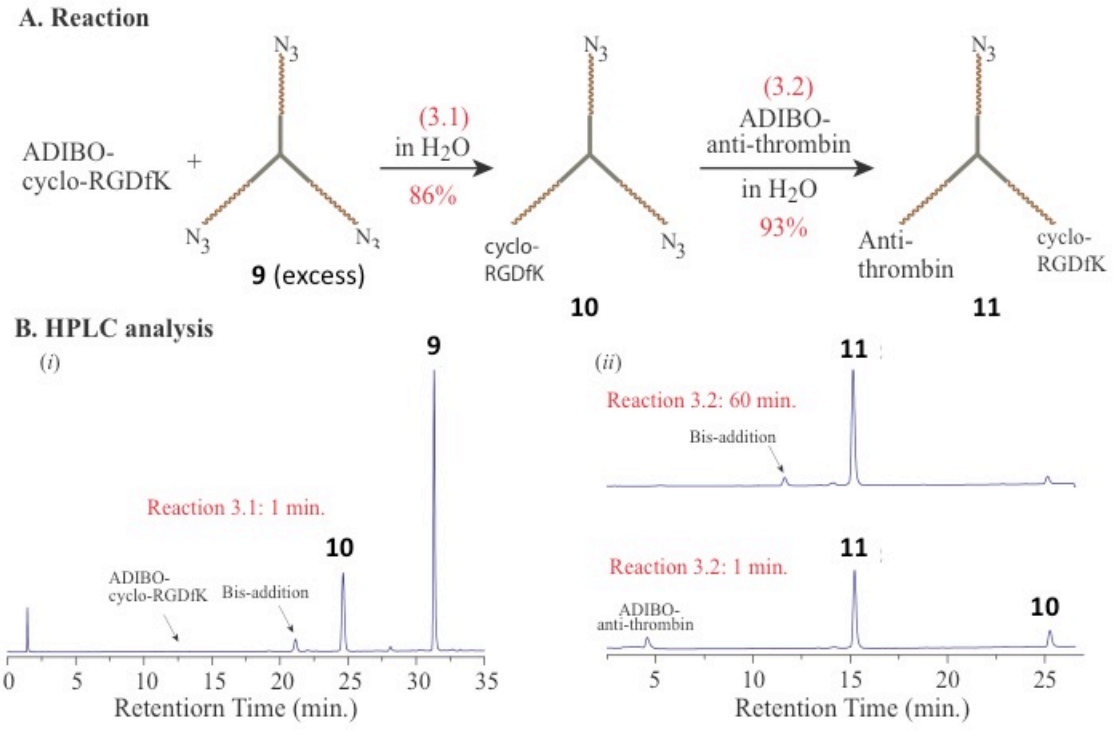

Figure 26. (A) Synthetic route to compound **11**; (B) RP HPLC chromatography of reaction mixtures with time, recorded by a UV detector at 280 nm for reaction 3.1 and 254 nm for reaction 3.2.

For synthesis of compound **11**, we took a route of starting from first attaching ADIBO-cyclo-RGD and then ADIBO-anti-thrombin aptamer to **9** (Figure 26. A). This strategy offered some advantages in controlling the reactions and separating the products over the other way around. Reaction 3.1 can easily be controlled at the mono-addition by

applying an excess amount of **9**. We used a 5 : 1 ratio between Ar3 and ADIBO-cyclo-RGD for the reaction. HPLC analysis indicated that soon after these two starting materials were mixed in water, ADIBO-cyclo-RGD was consumed right away, resulting in two products with a ratio of 86% to 14% (Figure 26. B-*i*). MALDI mass spectrometry identified that the major product was from one addition of ADIBO-cyclo-RGD to **9** (compound **10**) and the minor was resultant from the bis-addition. We carried out the reaction 3.2 in water as well with a 25% excess of **10**. As shown in Figure 26-B-*ii*, most of ADIBO-anti-thrombin was consumed in a minute. Extending the reaction to one hour resulted in **11** with a 93% yield and a small amount of bisadditon byproduct (~ 7%).

In this section, we present a facile method to synthesize a DNA–organic molecule–DNA (peptide) hybrid with a high yield and reaction rate by means of click chemistry. Lee *et al* reported that a three day reaction of amino functionalized DNA with N-hydroxysuccinimide (NHS) ester of 1,3,5- benzenetricarboxylic acid in DMSO/water only produced the desired product with a 10% yield (135). Such a low yield was probably a consequence of steric hindrance and electrostatic repulsion between DNA molecules. Interestingly, Seela and coworkers reported that a DNA containing a tripropargylamino side chain readily reacted with azido-functionalized oligonucleotides in the presence of a copper catalyst (136). Since the reaction was accelerated significantly in the presence of benzoic acid, we believe that reduction of the electrostatic repulsion may be a key factor for production of DNA-organic molecule–DNA hybrids with high yields.

Here, we demonstrated how to control the degree of charged molecules reacting with an entity containing multiple reaction sides simply by changing the solution conditions. It should be noted that the ADIBO-azide reaction normally results in a

regioisomeric mixture of the triazole connection. In our case, the affinity molecules were connected to **9** through either N-1 or N-3 of the triazole ring (see Figure 25). However, we have not observed that the subtle difference in structure exerts significant effects on the recognition imaging.

3.3.3 Attachment of molecular duos to AFM tips

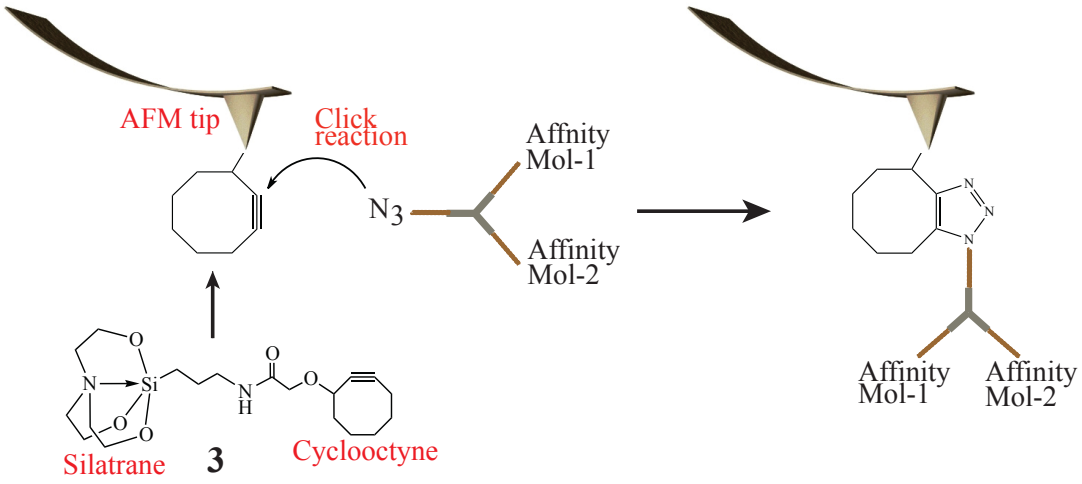

Figure 27. Illustration of attaching the tri-arm linker to an AFM tip using a catalyst free alkyne-azide reaction.

We previously developed a method for attachment of affinity molecules through a linear linker to AFM tips using a catalyst-free click reaction (132). We adopted this method for attachment of these molecular duos to AFM tips. As illustrated in Figure 27, a Ni-coated silicon tips (from Nanoworld particularly for recognition imaging) was first functionalized with cyclooctyne by reacting with a cyclooctyne derivative of 1-(3′-

amino)propylsilatrane (**3**) in the aqueous solution, and then subjected to reacting with a molecular duo solution (see experimental section for details).

3.3.4 Multiplex recognition imaging (RI)

We tested the recognition capability of the tri-arm linker (**11**) with a 1:1 mixed solution of thrombin and integrin $\alpha_5\beta_1$ deposited on the mica surface. The molecule **9** yielded a recognition image with 80% of proteins in the topographic image recognized (figure 28. A and B). After initial scanning, a step-wise blocking procedure was adapted to test the specificity of binding and to identify both the proteins in the mixture.

The initial blocking was done by passing $\alpha_5\beta_1$-integrin solution (50 µL, 10 pg/µL in 1X PBS buffer, pH 7.4) through the flow cell. The surface was imaged again after a period of 10 minutes. It was observed that number of recognition signal decreased and only 43% of the molecules were being recognized (figure 28. C). The free integrin in the solution blocked the RGD-peptide on the tip and hence the recognition of integrin stopped. All the recognized spots at this point were the thrombin molecules as the anti-thrombin aptamer attached to the tri-arm linker **11** was still active. Then we passed thrombin solution (50 µL, 10 pg/µL in 1X PBS buffer, pH 7.4) through the flow cell and the surface was scanned again after a period of ten minutes. Interestingly, the remaining recognition signal also almost disappeared (figure 28. D). This not only proved the specific nature of the recognition, but also it helped us to detect two proteins from a mixture using AFM recognition imaging. If we superimpose the first recognition image with the second one, we would be able to identify the thrombin and integrin molecules individually. In this way, using the synthesized tri-arm linker we could sequentially recognize two proteins.

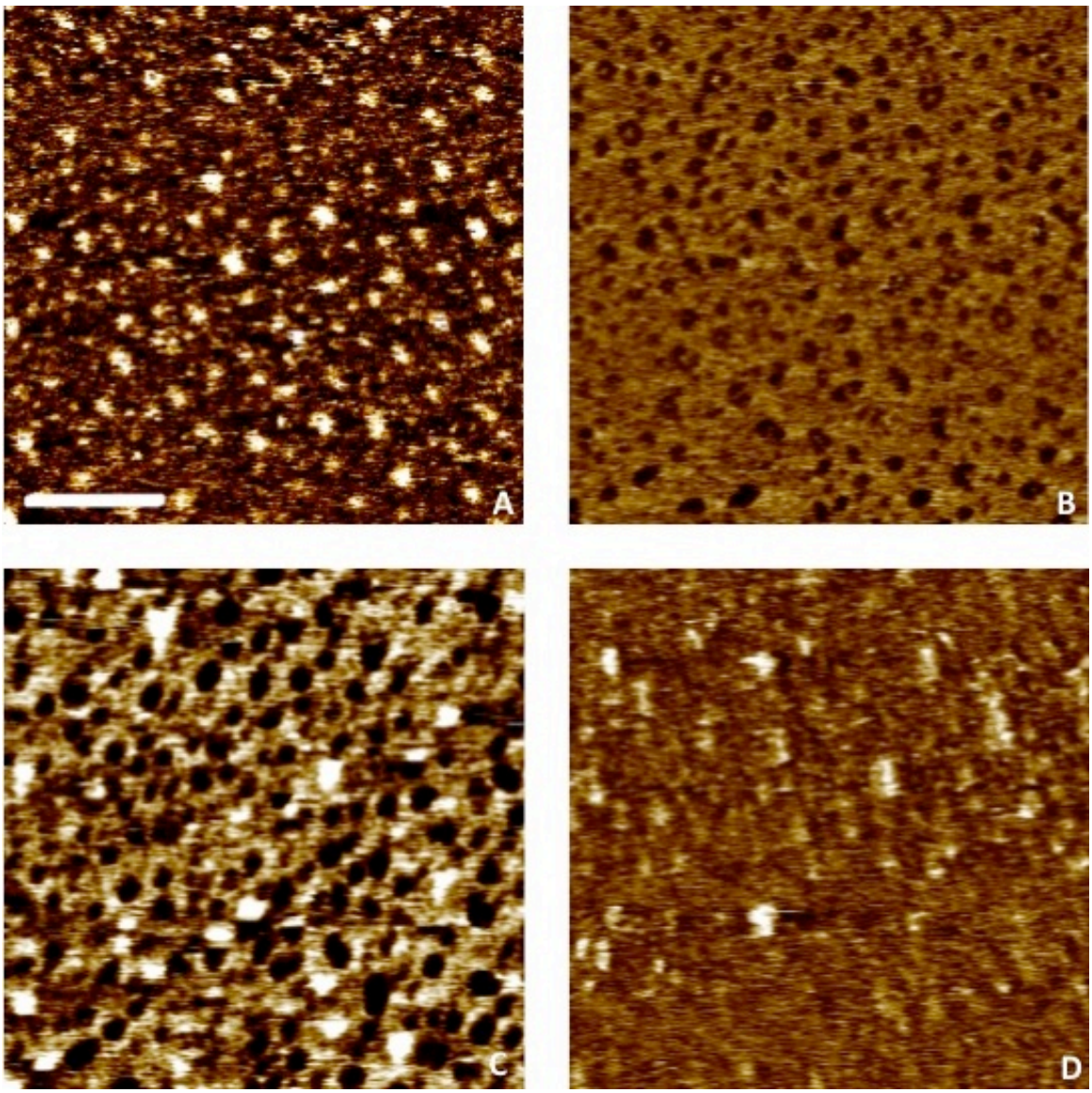

Figure 28. A) Topographic images for both thrombin and integrin, B) corresponding recognition image using the molecular duo **11** show the presence of both the proteins, C) after blocking RGD on the tip, recognition percentage decreased to 43%. At this point only thrombin molecules are being recognized. D) After blocking the anti-thrombin aptamer, recognition almost stopped.

3.4 Conclusion

Here, we demonstrated that a molecular duo tethered to an AFM tip can specifically detect multiple proteins immobilized on a surface. The multiplex recognition imaging is based on a hypothesis that two affinity molecules connected by a well-spaced linker can effectively interact with their respective target molecules. Our data show that affinity components in the molecular duos can work independently and equally, allowing us to determine the relative concentration of two proteins. In the current setup, it only needs 2-3 μL of protein solution with a concentration of ~ 0.02 ng/μL for each imaging experiment. Thus, an immediate application of the multiplex recognition imaging we would like to have is to measure ratios of free prostate-specific antigen (fPSA) and complexed prostate-specific antigen (cPSA) using a molecular duo composed of anti fPSA and cPSA antibodies for distinguishing between benign prostatic hyperplasia (BPH) and prostate cancer when the total PSA is in a "grey zone" range of 4 to 10 ng/ml (137). If free PSA is less than 25%, the man's high total PSA suggests that he may have the cancer. In contrast to conventional immunoassays (138), the multiplex recognition imaging is a digital method that has no need of calibration curves for the measurements. Furthermore, given its single molecule detection and nanometer resolution, AFM based multiplex recognition should be useful in analysis of proteins in multi-subunit complexes, such as nucleosomes. A nucleosome is composed of eight histones—typically two histone (H2A/H2B) dimers and a histone $(H3/H4)_2$ tetramer—wrapped with DNA. We can use the multiplex recognition imaging to detect the H2A/H2B dimer and its H2A.Z/H2B variant in nucleosomes (139). With a goal of applying the multiplex recognition imaging to biological research and clinical diagnostics, we developed a

scalable method suitable for manufacture of the molecule duo, including one-step synthesis of the tri-arm linker and high-yielded conjugation of aptamers. For proof of the molecular duo concept, we have taken advantages of nucleic acid and peptide aptamers, which have smaller sizes compared to antibodies, and are rapidly available by custom-synthesis as well as can be modified easily. As stated earlier, we would like to extend and apply this method to different biological modifications (DNA and histone modifications) taking place in nature, giving it a broader application.

CHAPTER 4

INVESTIGATING STRUCTURES AND PROPERTIES OF CHROMATIN EXTRACTED FROM NORMAL AND CANCER CELL LINES

4.1 Introduction

Epigenetic changes are the modifications to the genome without involving changes in the nucleotide sequences. These changes are believed to play an integral part in transforming a normal cell to tumor and can alter the accessibility of chromatin to transcriptional regulation (by inducing changes in chromatin structures) (41). The role and mechanism of epigenetic changes in the development of cancer has been a topic of much debate and still no consensus has been reached. Many mechanisms for repressing gene transcription have been proposed. Different modifications at different sites of the chromatin result in closed structure of the chromatin that limits access of the transcription factors to the gene. As a result, transcription stops. DNA methylation (140) and histone acetylation are most common epigenetic changes believed to be responsible for the silencing of tumor suppressor genes and activation of oncogenes. First, methyl CpG binding protein (MeCp2) binds with the hypermethylated DNA, which recruits protein complexes such as HDAC. HDAC deacetylates the lysine and as a result of that more compact structure of chromatin is formed because of the interaction between positively charged lysine residues and negatively charged DNA backbone. This compact structure blocks the regions of the genome from access to the transcription factors leading to gene silencing (141). Some studies revealed that MeCp2 also recruits transcription repressor Sin3A along with HDAC. Sin3A also plays a key role in gene silencing (Figure 29) (142,143).

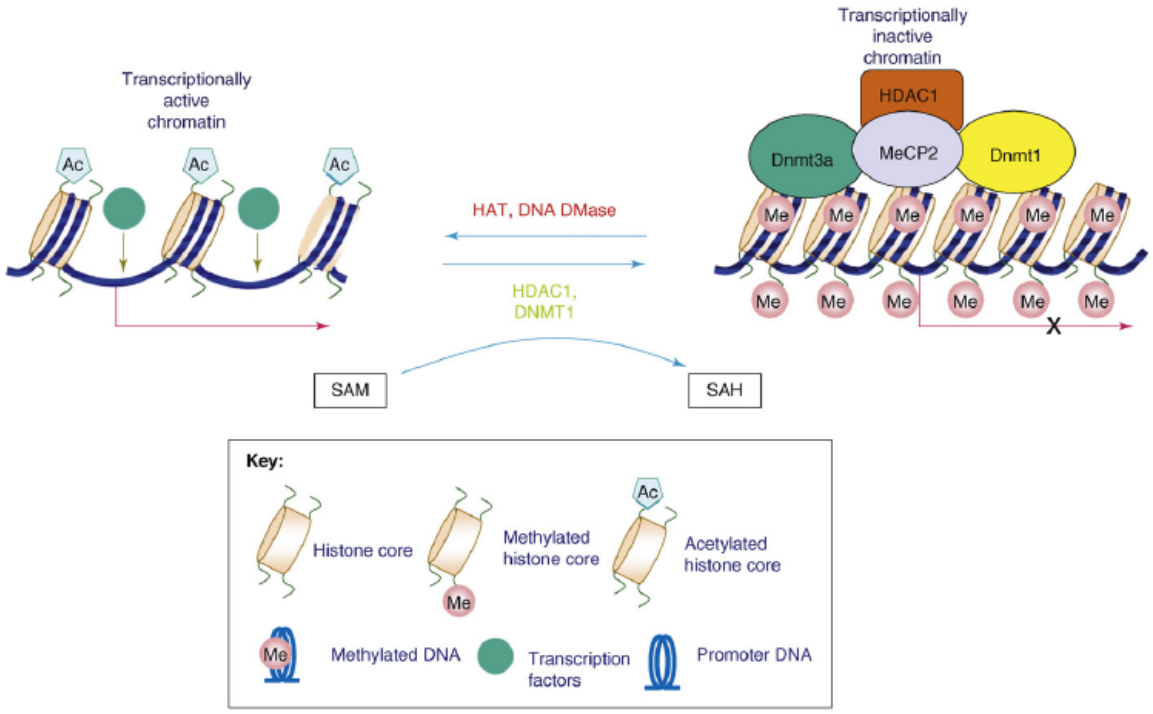

Figure 29. Interaction of MeCp2 with methylated DNA and subsequent incorporation of complexes such as HDAC. Adapted from reference (142)

In order to understand the role of the structural changes of chromatin in normal and cancer cells, we extracted chromatin from both types of cell lines using different salt fractions and then studied their structures and behavior using AFM imaging, recognition imaging other biophysical techniques such as DNA agarose gel and protein gel.

4.2 Methods of Chromatin preparation

Different methods of chromatin preparation and profiling have been adopted throughout the last few decades. The popular methods are chromatin immunoprecipitation (ChIP) (144,145) and using cleavage reagent such as deoxyribonuclease I (Dnase I) or micrococcal nuclease (Mnase) (146,147). We have followed another technique that involved different salt fractions to isolate chromatin from

cell nuclei. It was first reported in 1978 by Sanders (148). Successive use of different salt fractions enabled us to extract different chromatin fractions from Mnase treated nuclei depending on their solubility. Henikoff et al used this method for the extraction of chromatin from Drosophila S2 cells (149). Low salt fraction (LS) solubilized the easily accessible chromatin (open, beads-on-a-string) whereas high salt fraction (HS) solubilized the more condensed chromatin. Basically, gradual increase in salt concentration in the buffer helps to dissolve different parts of the genome. Finally, using TNE buffer, the insoluble part of the chromatin was extracted (150). The recovery of chromatin was almost quantitative and genome-wide profiling showed that the chromatin in LS and TNE fraction was active whereas that in HS fraction was inactive. We have used the same protocol to understand the chromatin distribution, shape, compactness and activities for four human cell lines, two normal (EPC2 and FHC) and two healthy (CP-D and RKO). We wanted to investigate these properties between normal and cancer cell lines and address the differences in behavior and structures from an epigenetic point of view.

4.3 Application of AFM in chromatin study

Imaging the chromatin arrays in air and aqueous medium can give us important information about the structure and compactness of the arrays. Moreover, other characteristic data such as nucleosomal height, diameter, volume, internucleosomal distances can be extracted at the single molecule level. On the other hand, using suitable protein or antibodies tethered to the AFM tip, presence or absence of particular protein component in the chromatin arrays can be investigated. Wang et al detected the immunoprecipitated CenH3 in chromatin extracted from Drosophila S2 cells using anti-

CenH3 as the probe molecule on the tip (64). Using the same anti-CenH3 functionalized tip, no recognition signal was detected for the bulk chromatin. They also showed height of the CenH3 was 1-2 nm indicating their tetrameric structure (Figure 30).

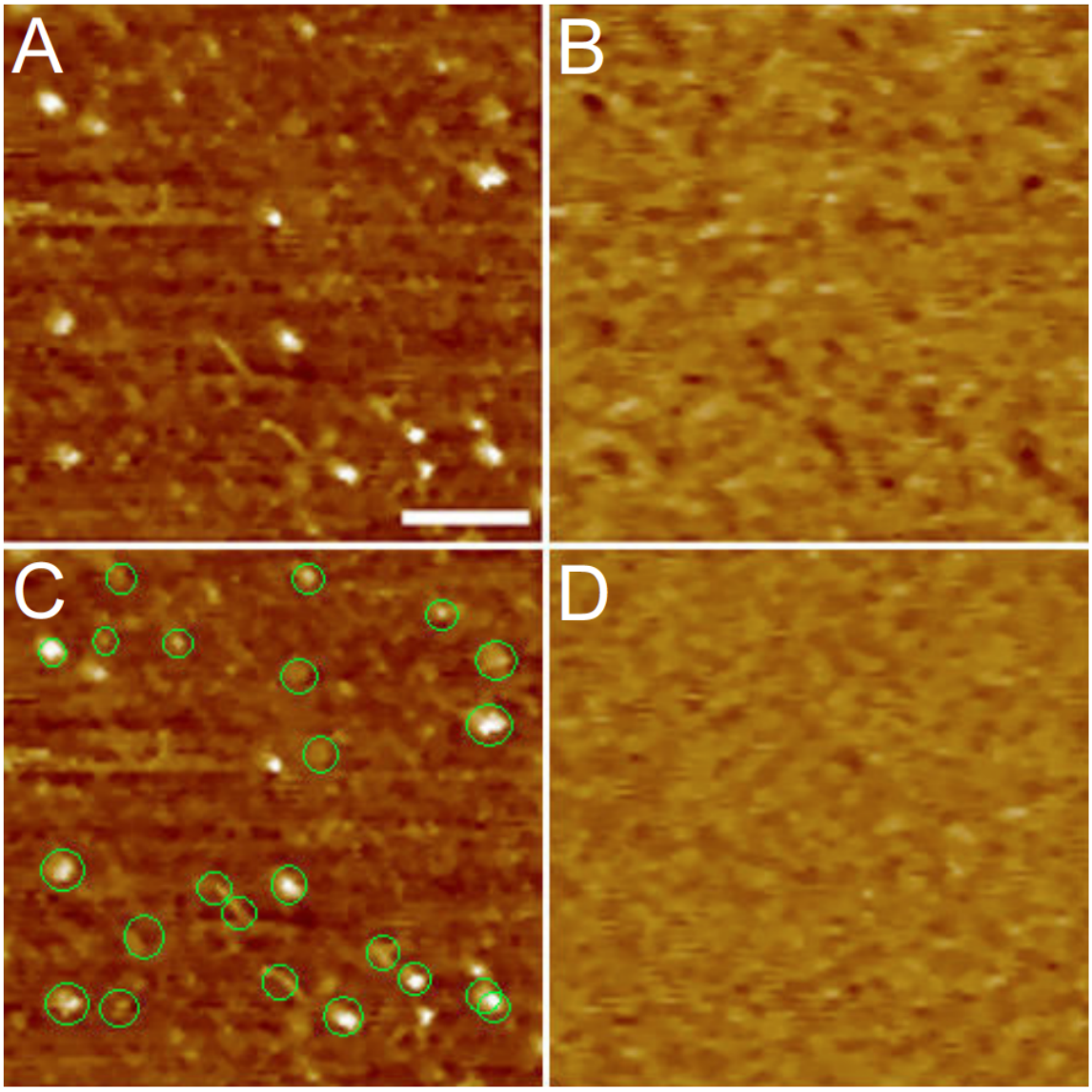

Figure 30. Recognition imaging of native CenH3 complex. A) Visualization of the CenH3 nucleosomes on mica, B) recognition of the CenH3 using an anti-CenH3 antibody, C) Overlay of the first two images and recognition spots are circled by green line, D) after blocking the tip with a peptide that binds with anti-CenH3 antibody,

recognition stopped indicating the specific nature of the binding. Adapted from (64)

Later, Dimitriadis et al extracted chromatin from human HeLa and HEK cell lines and used AFM topographic imaging to visualize the shape of the nucleosomal arrays and compare the nucleosomal height between CenH3 and bulk chromatin (151). They found height of the CENP-A nucleosomes were about half of that of bulk chromatin nucleosomes and they concluded that the CENPA nucleosomes are tetrameric whereas the bulk chromatin nucleosomes are octameric in nature (Figure 31).

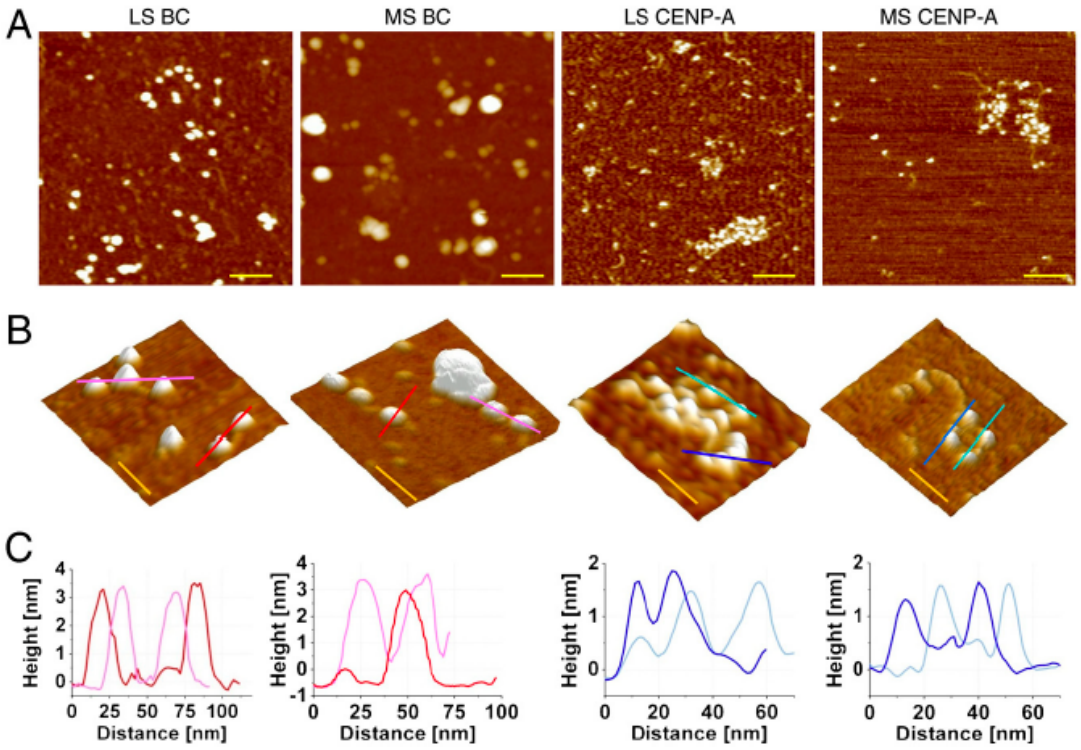

Figure 31. A) Low salt bulk chromatin, medium salt bulk chromatin, low salt CENP-A and medium salt CENP-A fraction immobilized on mica surface, B) corresponding 3D representation, C) height distribution data of the nucleosomes present in different fractions. Adapted from reference (151)

Using AFM recognition imaging, Stroh et al detected the presence of histone H3

in reconstituted nucleosomal arrays containing the mouse mammary tumor virus (MMTV) (152). In this case, polyclonal anti-histone anti H3 antibody was attached to the tip and the MMTV arrays were immobilized on APTES-mica (Figure 32). When the suitable blocking peptide was added that binds with the anti-histone H3 antibody on the tip, the tip was blocked and recognition stopped. Following similar method, changes in H2A were detected in MMTV nucleosomal arrays using anti H2A antibody (153). Later, acetylation of histone H4 was detected using an aptamer attached to the AFM tip (154). But almost all these experiments were done with reconstituted chromatin. The obvious next step was studying chromatin extracted from cell lines. Apart from the AFM topographical analysis, we were interested in the extent of DNA methylation of native chromatin fractions using recognition imaging using MeCp2 protein tethered tip.

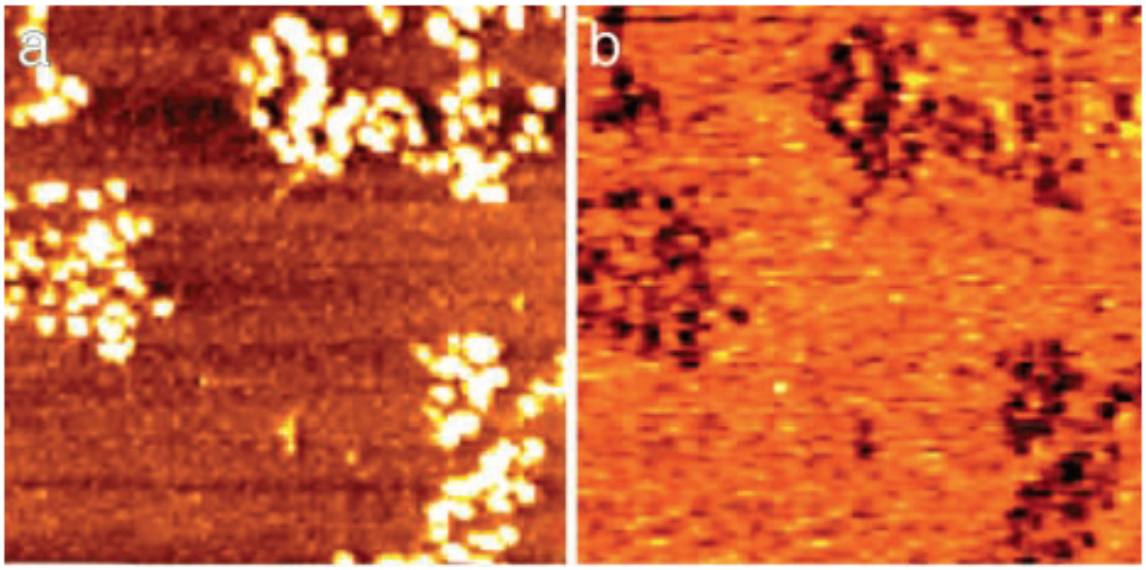

Figure 32. a) Topographic image of MMTV nucleosomal arrays, b) recognition of histone H3 using anti-histone H3 antibody tethered to the tip. Adapted from reference (152)

We tried to take this forward extracting chromatin from normal and cancer cell lines from two different sources of the human body. We chose EPC2 (normal) and CPD

(dysplasia) from esophagus and FHC (normal) and RKO (cancer) from colon and investigated the chromatin shape, compactness and structure from AFM imaging and DNA agarose gel.

4.4 Materials and Methods

4.4.1 Cell culture

EPC2, CP-D and RKO cell lines were supplied by Dr. Deirdre Meldrum lab (Biodesign Institute, ASU) and FHC cell line was bought from ATCC. Different media were used depending on the cell lines. For EPC2 and CPD cell lines, keratinocyte media (serum free) was used. FHC cells were cultured in DMEM:F12 media (with the added components suggested by ATCC). RKO cells were cultured in DMEM in media. 1% streptomycin was added to all the media. Cell culture media was changed every 3-4 days for all these cell lines. The details of these cell lines are given in table 3.

Table 3. Description of the cell lines used in this study

Name	Source	Morphology	Disease
EPC2	Esophagus	Epithelial	Normal
CP-D	Esophagus	Epithelial	High dysplasia
FHC	Colon	Epithelial	Normal
RKO	Colon	Epithelial	Carcinoma

4.4.2 Chromatin extraction

Trypsinized cells were centrifuged at 1000 rpm for 3 minutes and the supernatant was discarded. To the pellet, 2-4 million media was added. After spinning down (1000 rpm, 5 mins) the cells again at 4 °C, the media (supernatant) was discarded. The pellet

was washed by 1X PBS and spun down at 1000 rpm for 5 minutes at 4 °C. It was followed by a wash with 1X PBS with 0.1% tween-20. Tween-20 is a detergent that helps to disrupt the cell membrane. In the next step, 10 mL of 0.5% NP-40 in TM2 buffer with 0.5 mM PMSF was added to the pellet. NP-40 is a commercially available detergent nonyl phenoxypolyethoxylethanol that can break the cytoplasmic membrane, but not the nuclear membrane. PMSF is phenylmethylsulfonyl fluoride that blocks serine proteases like trypsin and chymotrypsin. After vortexing the cells slightly, the cells were set on ice for 2 minutes. Then the cells were spun down again at 4 °C at 1000 rpm for 10 minutes and the supernatant was discarded. The pellet was washed with 10 mL of TM2 buffer with 0.5 mM PMSF and again centrifuged at 4 °C at 1000 rpm for 10 minutes. The nuclei were suspended in 1 mL TE with 0.5 mM PMSF and incubated at 37 °C for 5 minutes. Then 15 µL of 100 mM $CaCl_2$ was added to the eppendorf followed by 2 µL of Mnase (concentration 0.2 units/µL) and the mixture was incubated for different time periods (2, 4, 8 and 16 mins). After respective Mnase incubation period, the solution was transferred to an eppendorf in ice and 20 µL of 0.5 mM EGTA was used to stop Mnase activity. Mnase needs Ca^{2+} for its digestive function. EGTA binds with free Ca^{2+} ion to form chelate complex. As a result of lack of free Ca^{2+}, Mnase stops working. The mixture was spun down again at 1600 rpm for 10 minutes. After removing the supernatant, the pellet was suspended again in low salt buffer (75 mM NaCl) and placed on the rocker for 4-6 hours. After that the supernatant was collected in an eppendorf (low salt fraction). Then the pellet was again suspended in high salt buffer (600 mM NaCl) and placed on the rocker for 4-6 hours. The supernatant was again collected (high salt fraction).

4.4.3 AFM imaging

All the chromatin samples were diluted in 1X PBS buffer before imaging (for a final concentration of ~0.3-0.5 ng/μL). Chromatin samples were cross-linked with 0.5% glutaraldehyde for 15 minutes and then placed on APTES-modified mica. After 5 minutes, the mica surface was washed with 1X PBS buffer thrice and dried before imaging.

AFM topographic images were taken in AAC mode using an Agilent 5500 AFM instrument (with inverted light microscope). The cantilever used for topographic imaging had a length of 125 μm, width 35 μm, and thickness 800 nm and resonant frequency of ~350 kHz. Images were taken with 4% drive and set point around 6V. In general, 1X1 μm^2 and 2X2 μm^2. Images were processed with Gwyddion software.

4.4.4 Agarose gel

DNA gel was done in 0.8% agarose gel. At first DNA was isolated from the chromatin using the standard techniques. DNA was removed from proteins using SDS, Rnase and proteinase. DNA was purified from this mixture using phenol:isoamyl alcohol:chroloform solution followed by ethanol precipitation. Concentration of DNA was measured using Nanodrop (Thermo Scientific). Then using 6X DNA loading dye, DNA was loaded in the gel and run for 2 hrs at 60 V using 1X TAE as running buffer.

For DNA sequencing experiments, the 200 bp bands were excised and centrifuged at 8000 rcf for 10 minutes using G-25 columns. The resulting solution had DNA in TAE buffer. Using ethanol precipitation method, pure DNA was isolated and diluted in water.

High molecular weight bands were cut and processed in the same way but were sonicated before constructing the library needed for sequencing.

4.5 Result and discussion

4.5.1 Mnase Sensitivities of chromatin

Micrococcal nuclease (or, Mnase) is an enzyme that digests the single-stranded DNA, double stranded DNA or RNA. The molecular weight of the enzyme is ~16.9 kD. It is obtained from *Staphylococcus aureus*. Ca^{++} is absolutely essential for the activity of Mnase. Hence the Mnase can be easily inactivated using EGTA. As EGTA has very high affinity for Ca^{++} binding, the Mnase stops working in absence of free Ca^{++}. The enzyme works best at 37 ºC.

We wanted to investigate the structure and the compactness of the chromatin extracted from different cell lines (both normal and tumor). So the nuclei extracted from different cell lines were subjected to Mnase treatment for different period of time (2 min, 4 min, 8 min and 16 min) at 37 ºC in presence of Ca^{++}. After the required time periods, EGTA was added to the Mnase treated nuclei to stop the Mnase digestion. From these nuclei different chromatin fragments were extracted using the low salt buffer, high salt buffer and TNE buffer (detailed protocol is described in section). From these chromatin fractions, DNA was extracted and sizes of these DNA fragments were analyzed using the agarose gel. Finally all these chromatin fractions were imaged using the AFM to investigate the size and shape of the nucleosomal arrays.

DNA was extracted from all these chromatin fragments carefully and the sizes of the DNA fragments were analyzed using the agarose gel in TAE buffer. The shorter DNA fragments will travel more distance and longer will travel less. We wanted to investigate

if Mnase has any particular trend in its sensitivity towards the normal and cancer cells or Mnase sensitivity is entirely cell line dependent. The trend in Mnase sensitivity indicates the compact nature or the open structure of chromatin.

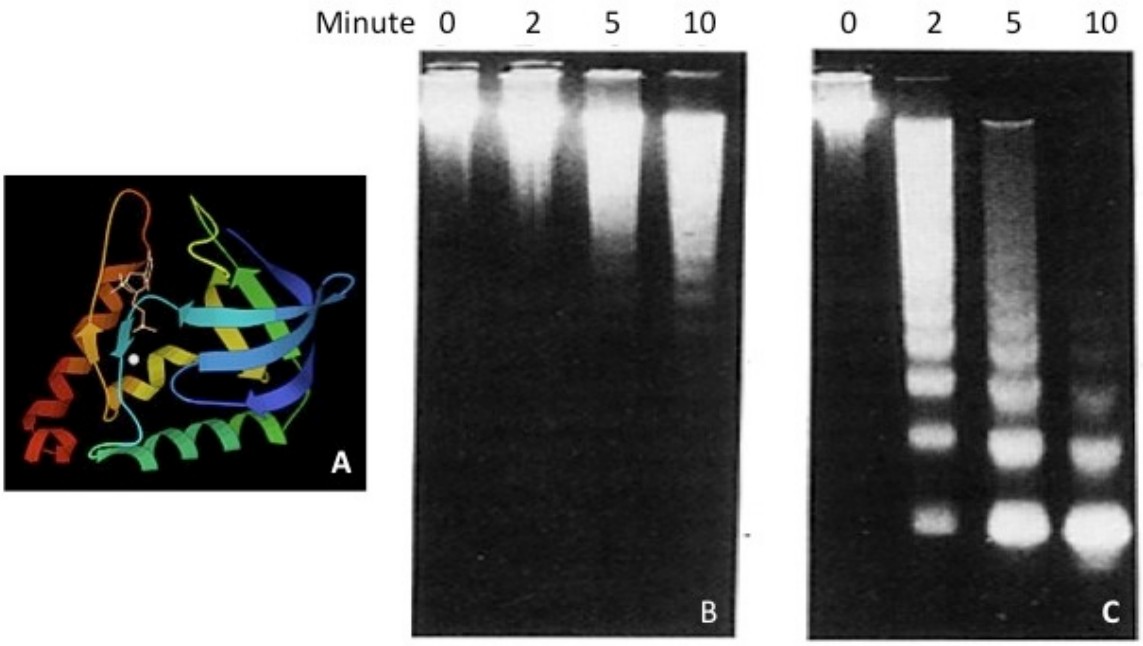

Figure 33. A) Ribbon schematic structure of Mnase, B) Mnase digestion pattern for bulk chromatin from normal fibroblast cells, C) Mnase digestion pattern for bulk chromatin from c-Ha-ras $^{Val\ 12}$ oncogene transformed NIH-3T3 fibroblast cells. Adapted from (155)

Laitnen et al tested the Mnase sensitivities of the normal fibroblast (N1) and c-Ha-ras $^{Val\ 12}$ oncogene transformed NIH-3T3 fibroblast cells (E4) and found out the E4 cells were more sensitive to Mnase digestion (Figure 33) (155) . When we did Mnase digestion time course study on all four cell lines, we found the similar trend for the esophageal cell lines, but not for the colon cell lines. The CPD chromatin was easily digested compared to the EPC2 chromatin by Mnase (Figure 34). This indicates much more open structured chromatin fragments of the CPD cell lines and compact structured chromatin arrays in EPC2. So the DNA regions are more accessible to Mnase in case of

CPD than EPC2. At the same time, it was observed that the high salt fractions were difficult to digest compared to the low salt fractions of the same cell line. That means the high salt fraction of any cell line contains more condensed chromatin arrays and the low salt contains more open structure. This trend was earlier seen in case of Drosophila fly.

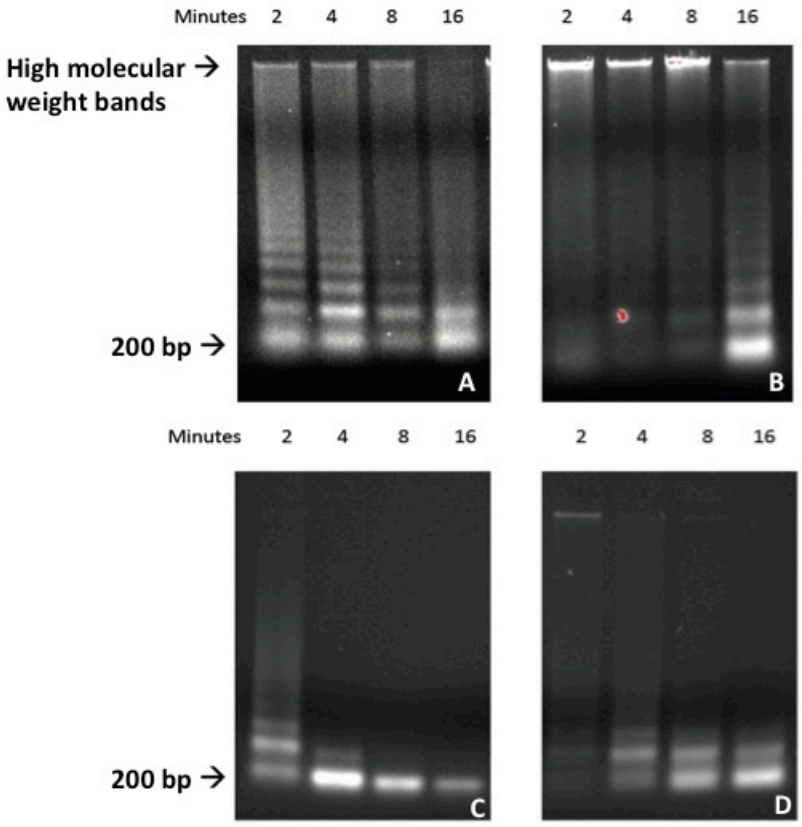

Figure 34. Mnase digestion pattern as a function of time (2, 4, 8 and 16 minutes). Mnase digestion of A) EPC2 LS fraction, B) EPC2 HS fraction, C) CP-D LS fraction and D) CP-D HS fraction

Same Mnase time course study was performed for the normal colon (FHC) and cancer (RKO) cell line also (Figure 35). There was not much difference in between the pattern of digestion for those two cell lines. Low salt and high salt fractions for the two cell lines were very similar. But the high salt for both FHC and RKO were exhibiting

higher molecular weight bands compared to their low salt fractions. This clearly shows lack of accessible sites for Mnase in case of high salt fractions for both FHC and RKO indicating compact structures for high salt arrays and more open structures for low salt arrays. This assumption was further supported by the atomic force microscopy images of the arrays extracted from low and high salt fractions. More experiments are needed for FHC cell line.

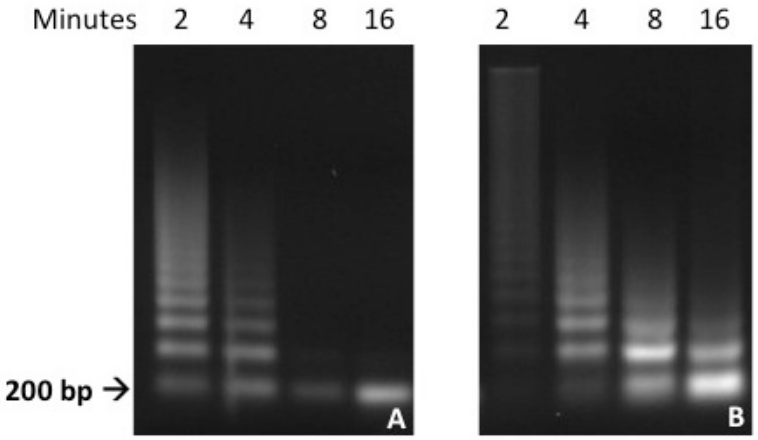

Figure 35. Mnase digestion pattern as a function of time (2, 4, 8 and 16 minutes). (A) RKO LS fraction, (B) RKO HS fraction

4.5.2 AFM imaging

AFM imaging was a key tool for the investigation of the structure and shape of different chromatin arrays extracted using different salt fractions. As stated earlier, chromatin samples were diluted (to obtain a final concentration of ~0.3-0.5 ng/µL) and immobilized on APTES mica substrate using glutaraldehyde chemistry. The difference between the low and high salt fractions of chromatin was evident between all the cell lines. Arrays in high salt were clearly more condensed and compacted than that in low salt fractions.

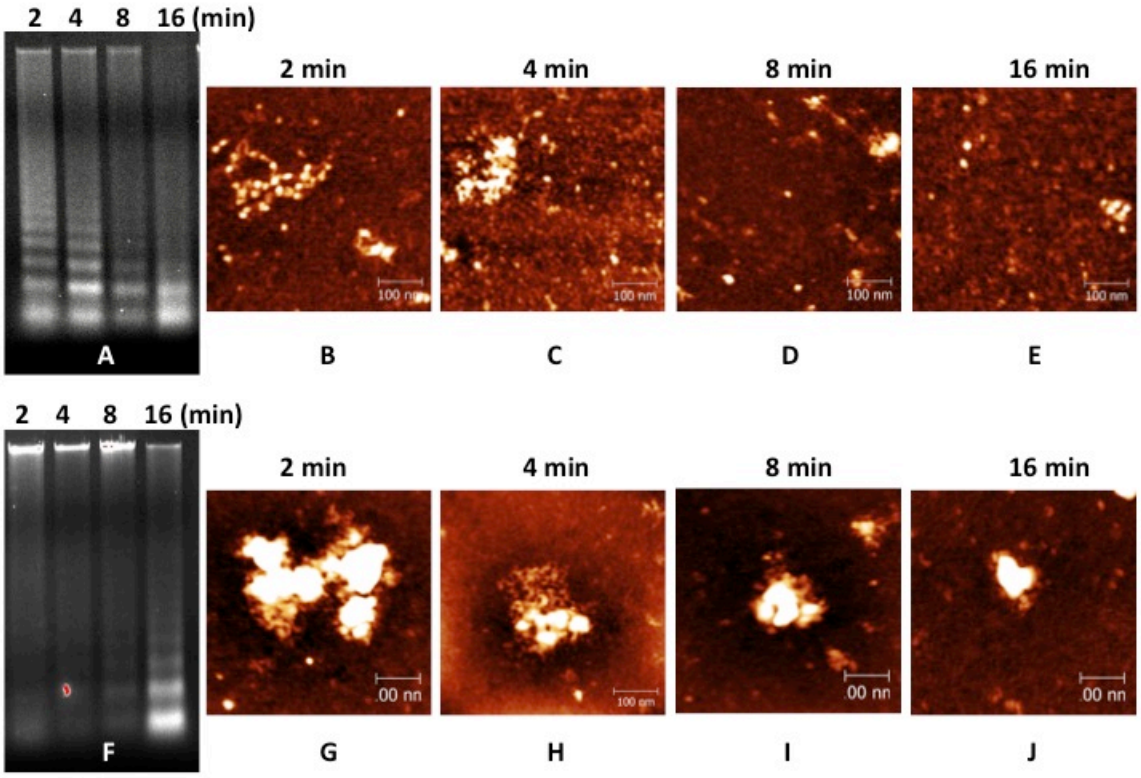

Figure 36. (A) Mnase digestion pattern for LS fraction for EPC2 cells, (B, C, D, E) the chromatin fractions, from which the DNA was isolated for the gel, were imaged using AFM for different time of digestion. (F) Mnase digestion pattern for HS fraction for EPC2 cells, (G, H, I, J) corresponding chromatin fractions were imaged using AFM for different time of digestion. The LS fraction was digested easily with time but condensed arrays in HS fraction were difficult to digest and some big blobs still could be seen at 16 minutes.

Mnase time course study provided interesting trend for the structure of arrays. EPC2 LS fractions showed mainly two types of arrays, open beads-on-a-string arrays and compacted arrays (with higher ratio of open arrays) at t= 2 minutes. With increasing digestion time, both the arrays got shorter and shorter and finally producing small arrays

and predominantly mononucleosomes for t= 16 minutes (1≤ n ≤5). Average height of LS arrays at 2 minutes Mnase digestion was from 2.5 nm (open arrays) to ~10 nm (condensed arrays). EPC2 HS fractions mainly contained the highly condensed arrays at t= 2 minutes. With increasing digestion time, the arrays didn't get as shorter as the LS fraction. Even at 16 minutes, big condensed arrays were visible with slightly more number of mononucleosomes (Figure 36). These observations support the agarose gel data.

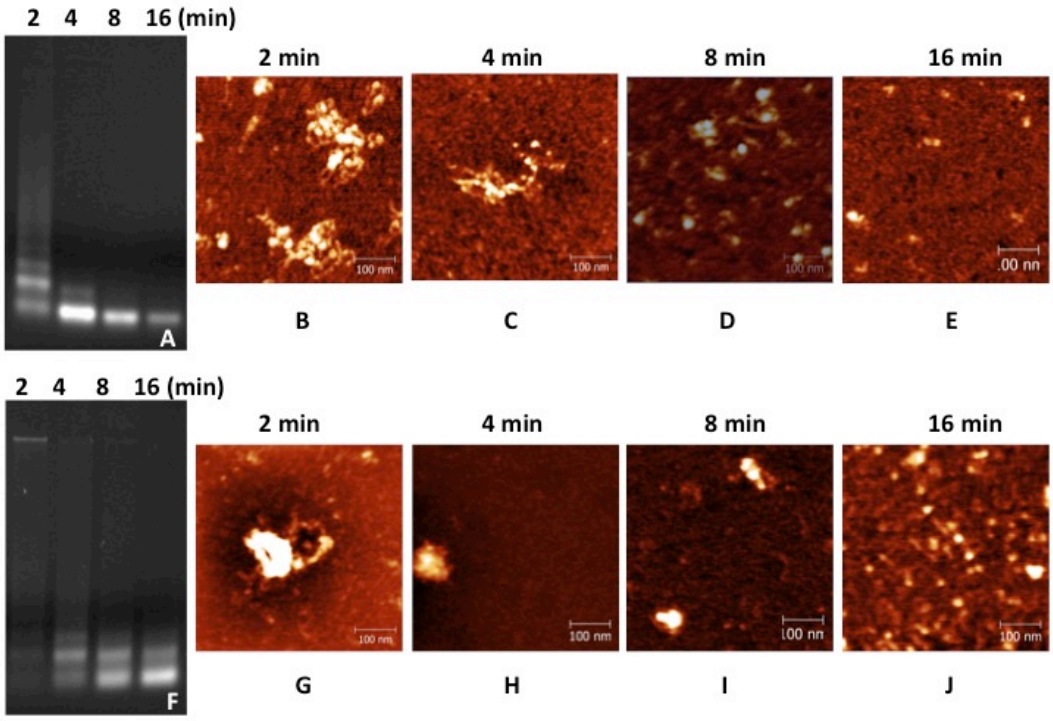

Figure 37. (A) Mnase digestion pattern for LS fraction for CP-D cells, (B, C, D, E) the chromatin fractions, from which the DNA was isolated for the gel, were imaged using AFM for different time of digestion. (F) Mnase digestion pattern for HS fraction for CP-D cells, (G, H, I, J) corresponding chromatin fractions were imaged using AFM for different time of digestion.

The same experiment with CPD cell line produced different outcome (Figure 37). At 2 minutes Mnase digestion, the LS arrays were mainly open structured (with very small amount of condensed arrays). Average height of these arrays was ~2.6 nm. With increasing digestion time, the LS arrays became smaller and smaller and finally producing mainly mononucleosomes at 16 minutes. The HS fraction of CPD produced condensed arrays at t= 2 minutes (average height ~10 nm). Interestingly, with longer exposure to Mnase these condensed arrays broke down to smaller arrays or mononucleosomes making it different from the EPC2 HS arrays (average height was ~2.5 nm). Again, the agarose gel data supports this.

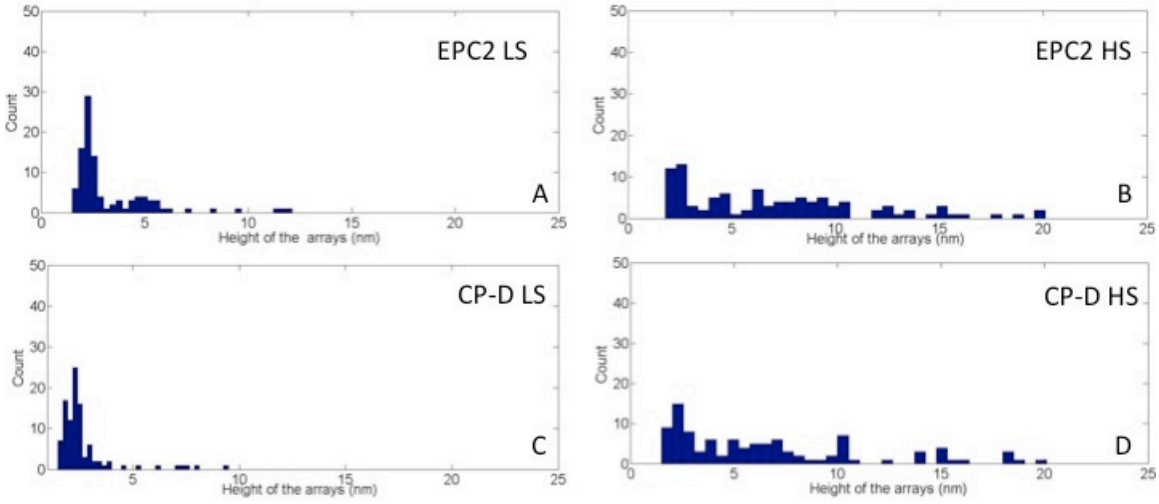

Figure 38. Height distribution for nucleosomal arrays at 2 minutes Mnase digestion. The images are for A) EPC2 low salt, B) EPC2 high salt, C) CP-D low salt, D) CP-D high salt

When we plotted the distribution for the height of the arrays for 2 minutes Mnase digestion, the differences were evident (Figure 38). The low salt fraction for both EPC2 and CP-D were found to have arrays with height mainly around 2.5 nm (which is the expected height for the octameric structures of histone). But the EPC2 had another population of arrays with height ~5 nm which were due to the condensed arrays present

in low salt. This feature was absent in low salt of CP-D. The high salt fractions for both EPC2 and CP-D had a wide distribution of 2-20 nm which indicated the presence of highly compacted arrays. Overall, EPC2 arrays were found to be little more condensed than the CP-D arrays.

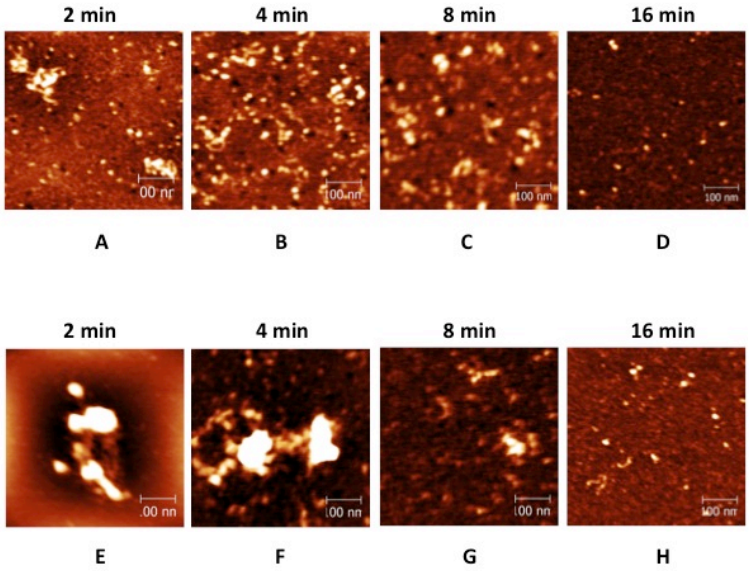

Figure 39. (A, B, C, D) AFM images of the LS chromatin fractions for FHC cell line for different time of digestion. (E. F, G, H) Same for HS fraction for FHC cell line

When AFM imaging was done for LS and HS arrays for FHC and RKO cell lines, the trend in the outcome was little different from the esophageal cell lines (EPC2 and CPD). The HS arrays were still more condensed than the LS arrays (beads-on-string) for both FHC and RKO (Figure 39 and 40). But the arrays obtained for different time periods of Mnase digestion were very similar for FHC and RKO (for same salt fractions). The LS fractions of both FHC and RKO were representing the classical bead-on-a-string structure (t= 2 mins). The average of these arrays were 2.5 nm and they got shorter with Mnase

digestion time and eventually formed mononucleosomes (t= 16 minutes). The HS fractions of both FHC and RKO had highly compacted arrays at t= 2 minutes with the average height being ~8 nm. But unlike EPC2, both FHC and RKO HS arrays were digested more and more with increasing time and at 16 minutes of Mnase digestion, both produced mononucleosomes or very short arrays ((1≤ n ≤5). These digestion pattern of HS fractions of FHC and RKO were similar to the pattern shown by CPD, but drastically different to that of EPC2.

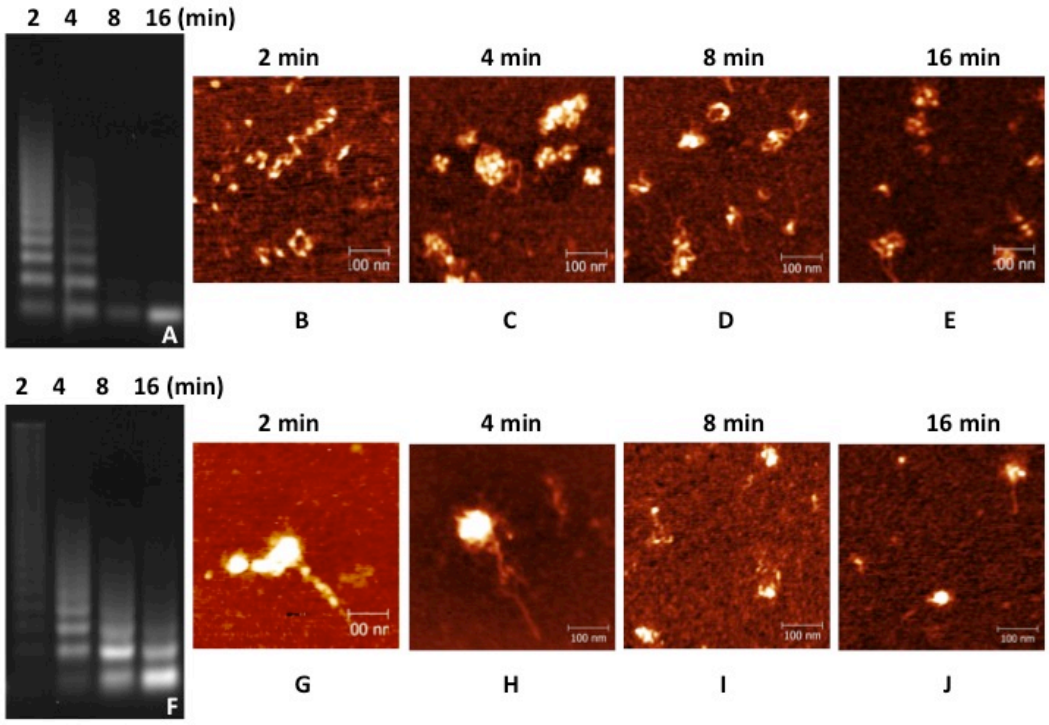

Figure 40. (A) Mnase digestion pattern for LS fraction for RKO cells, (B, C, D, E) the chromatin fractions, from which the DNA was isolated for the gel, were imaged using AFM for different time of digestion. (F) Mnase digestion pattern for HS fraction for CP-D cells, (G, H, I, J) corresponding chromatin fractions were imaged using AFM for different time of digestion.

4.5.3 Partitioning of DNA between the low and high salt soluble fractions in normal and cancer phenotypes

The DNA absorbance of chromatin extracted at various digestion times from all four cell lines in the high and low salt fractions was measured using a Nanodrop spectrophotometer. A fraction of the genome remains in an insoluble pellet, and this was resuspended in TNE buffer and also measured. The amount of DNA in this insoluble fraction was small, so we focus on the relative amounts of DNA in the low and high salt soluble fractions.

When we normalized the concentration of chromatin obtained from different extractions over a long period of time for all the cell lines, we found an interesting trend. The low salt fraction of the normal cell contained more DNA than the high salt. But the amount of DNA in high salt fraction of the cancer cell lines were few times higher than that of low salt in case of the cancer cell lines. The average concentrations are given in Table 4.

Table 4. Average amount of DNA present in different fraction for all cell lines

Mnase digestion	EPC2 LS (ng/μL)	EPC2 HS (ng/μL)	CP-D LS (ng/μL)	CP-D HS (ng/μL)	FHC LS (ng/μL)	FHC HS (ng/μL)	RKO LS (ng/μL)	RKO HS (ng/μL)
2 min	277.1	125.4	216.8	346.1	340	116	276.1	318.7
4 min	258.1	152.5	158.4	244.3	420	168	174.6	307.5
8 min	260.8	114.1	177.6	280.2	480	112	233.9	350.0
16 min	287.0	146.4	191.8	315.5	96	52	184.1	395.3

Figure 41 shows the ratio of the amount of DNA in the high salt fraction to the amount of DNA in the low salt fraction (H/L) for all four cell lines. In order to control for differences in cell population from culture to culture, the cells were grown and processed multiple times (CPD 5 runs, EPC2 7 runs, RKO 9 runs, FHC 1 run). The slow growth of the FHC line has limited the amount of data for that line. Figure 41 shows the value for H/L for all four cell lines. Henikoff et al found that, in the case of Drosophila, the bulk of the genome was found in the high salt fraction. However, it is immediately clear from Figure 41 that the H/L ratio changes enormously between cell lines. Strikingly, the bulk of the genome is contained in the low salt fraction for the two normal cell lines (EPC2 and FHC). Furthermore, this ratio is about the same for both cell lines, though they represent different tissue types. The opposite is true of the two cancer cell lines, where the overwhelming majority of the genome is in the high salt fraction (CPD and RKO). Quite remarkably, the two cancer cell lines are very similar, and very different form their normal counterparts. Thus, at least in these four cell lines, the H/E ratio is a marker of the cancer phenotype.

These data are presented as a function of Mnase digestion time because at least some digestion is required for results to be reproducible. Even at 2 minutes digestion, the spread in the H/E ratio is large. However, very long digestion times will result in mononucleosomes and presumably therefore little difference in the solubility of the chromatin. However that point is not reached in the data shown here.

Table 5. Ratio of DNA in HS and LS for all cell lines

	EPC2 HS/LS	S. D.	CP-D HS/LS	S.D.	FHC HS/LS	S.D.	RKO HS/LS	S.D.
2 min	0.5018	0.1319	6.0652	6.0652	0.3411	-	1.4329	0.6578
4 min	0.5138	0.1342	1.7465	0.8195	0.4000	-	1.9814	0.6924
8 min	0.4551	0.1581	2.1598	1.0656	0.2333	-	2.4227	1.2232
16 min	0.5176	0.1628	2.7568	2.1219	0.5416	-	2.6577	1.2592

The repeated preparations allowed us to characterize the variations in properties of the cells from culture to culture (with the exception of the FHC at this point). The spread in data for the EPC2 is small (error bars are +/- 1 SD). However, the variations in the cancer phenotypes are much larger, indicating a much greater heterogeneity.

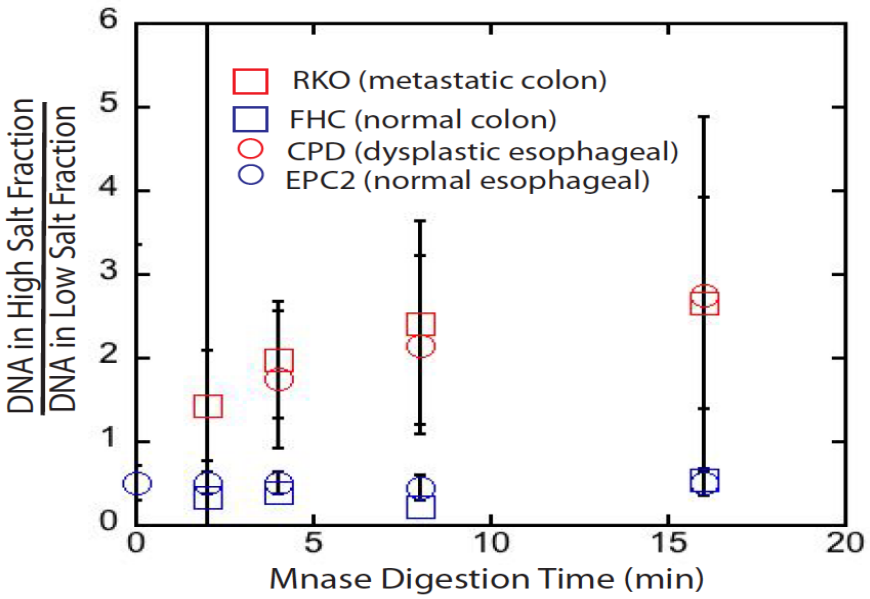

Figure 41. Ratio of the amount of DNA in the high-salt soluble chromatin fraction to that in the low salt soluble fraction for all four cell lines as a function of Mnase digestion time. Cancer phenotypes are red data points, normal are blue. The error bars are the SD obtained from repeated cultures of the cell lines.

4.6 Conclusion

In this research, we have worked with four human cell lines from two different sources, esophagus and colon. We studied one normal and corresponding cancer cell line for each. EPC2 and FHC were the normal cell lines from esophagus and colon respectively and CP-D and RKO were corresponding cancer cell lines. Our goal was to compare the structure and the properties of chromatin extracted healthy and cancer cell lines.

Following salt extraction method, we extracted chromatin arrays from Mnase treated nuclei and investigated them using different tools like atomic force microscopy and gel electrophoresis. Concentration measurement of the chromatin fractions using NanoDrop indicated that low salt fractions extracted higher amount of chromatin for normal cell lines (EPC2 and FHC). But chromatin concentration for high salt fraction was almost two to four times higher than that in low salt fraction in case of cancer cell lines (CP-D and FHC). This gave us indication of higher amount of condensed (inactive) chromatin fraction in case of the cancer cells.

Agarose gel electrophoresis of the DNA extracted for all four cell lines proved that high salt fractions were showing much higher molecular weight bands than corresponding low salt fraction for all the cell lines. Interestingly, it was also found that salt fractions (both LS and HS) of EPC2 were harder to digest compared to that of CP-D.

This indicated even more compacted and condensed chromatin is present in EPC2 nuclei than in CP-D nuclei. But, the gel electrophoresis pattern for FHC and RKO were almost similar (even though more experiments need to be done for FHC cell line before coming to a final conclusion).

Finally, AFM served as a powerful tool to visualize the shape and structure of the arrays immobilized on APTES mica. AFM images excellently correlated with the agarose gel electrophoresis. The high salt arrays were found to be condensed blob like structures and the low salt arrays were classical beads-on-a-string (open) structure. With the increase in Mnase digestion time, more and more smaller arrays and mononucleosomes were observed. The presence of big condensed structures in HS fraction compared to LS fraction even at higher digestion time proved the presence of less accessible condensed structure in HS compared to easily accessible open structure in LS (again in accordance to the gel result).

In future studies, we are interested in profiling the genome of these cell lines according to the salt fractions. In genome-wide profiling of Drosophila S2, it was observed that LS fraction and TNE buffer (insoluble pellet) contained active genes but the HS fraction contained the inactive part. We are interested to if same outcome holds true for the human cell lines we are working with.

Also, elastic properties of whole cells have been studied extensively in relation to the development of the cancer phenotype, but the elastic properties of the nucleus remain controversial with a very wide range of reported values. We are interested in exploring the size difference and elasticity of nuclei for normal and cancer cell lines.

CHAPTER 5

CONCLUSION

5.1. Summary of research

This research described the application of atomic force microscopy in understanding the structure of different biological molecules (proteins, DNA, chromatin etc) and biological interactions (such as DNA aptamer-protein, peptide-protein) at the single molecular level. AFM based topographic imaging, recognition and force spectroscopy were the main techniques used for this study. Agarose gel electrophoresis has been used to study DNA fragments extracted from human cell lines. NMR, mass spectroscopy, HPLC were used to characterize different organic molecules or bioconjugated products synthesized for this study.

In the first study, we have developed a new method for functionalization of AFM tips in aqueous medium using copper-free click chemistry. We detected the presence of human α-thrombin and $\alpha_5\beta_1$-integrin using anti-thrombin aptamer and cyclo-RGDfC functionalized tip respectively using recognition imaging. We also measured the force of interaction between those two systems. We believe this method will solve some common problems associated with AFM tip functionalization and help us to attach different affinity molecules to the AFM tip in a simple, user-friendly way.

After detecting one protein using recognition imaging, we focused on detecting two proteins simultaneously from a mixture of proteins. Many biological processes in nature involve changes in multiple molecules (protein etc) at the same time. To investigate those phenomena, we designed and synthesized a tri-arm linker consisting of two affinity molecules (anti-thrombin aptamer and cyclo-RGDfK peptide). The third arm

of the linker was used for attachment to AFM tip. Using this linker, we detected two binding events simultaneously and detected human α-thrombin and $\alpha_5\beta_1$-integrin in a same experiment. Stepwise blocking experiment proved the specificity of the interaction. Using this technique, many multivalent biological interactions can be studied in future.

In the final chapter, we investigated the structure of chromatin extracted from human cell lines and tried to analyze the difference between their compaction in normal and cancer cell lines using AFM imaging and agarose gel electrophoresis. We used four cell lines, EPC2 (normal), CP-D (late dysplasia), FHC (normal), RKO (carcinoma) and extracted chromatin from them using salt extraction method. EPC2 and CP-D were from human esophagus and FHC and RKO were from colon. We found the chromatin from EPC2 to be more compact than CP-D. Chromatin from RKO cells were also less compact (like CP-D), We have conducted some initial experiments on FHC. But more experiments need to be done before coming to a conclusion regarding FHC cells. We also found that DNA content ratio of high salt fraction to the low salt of the cancer cells were much higher than the normal cells.

5.2 Future studies

Experiments involving the FHC cell line (chromatin extraction, Mnase gel and AFM study) need to be repeated. Few more experiments with chromatin from FHC cell lines will enable us to compare the structure and compaction of chromatin from FHC and RKO cell lines.

Next, we plan to profile different salt fractions of chromatin extracted from normal and cancer cell lines based on gene activity. Henikoff et al already did the genome-wide profiling of different salt fractions extracted from Drosophila S2 cell. Our

experiments will show if we can see the same pattern for human cell lines. Also it will describe if there is any difference between the active gene profiles of normal and cancer cells.

We are planning to perform protein gel and then the Western Blot to check the presence of euchromatin and heterochromatin in the extracted low and high salt fraction. Histone is known to be trimethylated at the lysine 9 position in case of heterochromatin. H3K9Me3 acts as an epigenetic mark for heterochromatin. So, running the Western Blot experiments using anti-H3K9Me3 antibody as the primary antibody, we could detect the presence of heterochromatin in the different salt fraction.

Finally, we would like to compare the elasticity of nuclei extracted from normal and cancer cell. Then we would like to correlate our findings with the nuclei size and compacted chromatin structure obtained from AFM and gel study.

REFERENCES

1. Cheng S, Bryant R, Doerr SH, Rhodri Williams P, Wright CJ. Application of atomic force microscopy to the study of natural and model soil particles. J Microsc. 2008 Sep [cited 2015 Jan 7];231(3):384–94.

2. Müller DJ, Schabert FA, Büldt G, Engel A. Imaging purple membranes in aqueous solutions at sub-nanometer resolution by atomic force microscopy. Biophys J. 1995 May;68(5):1681–6.

3. Jalili N, Laxminarayana K. A review of atomic force microscopy imaging systems: application to molecular metrology and biological sciences. Mechatronics. 2004 Oct;14(8):907–45.

4. Binnig G, Rohrer H, Gerber C, Weibel E. Surface Studies by Scanning Tunneling Microscopy. Phys Rev Lett. 1982 Jul; 49(1):57–61.

5. Binnig G, Quate CF. Atomic Force Microscope. Phys Rev Lett. 1986 Mar;56(9):930–3.

6. Zhong Q, Inniss D, Kjoller K, Elings VB. Fractured polymer/silica fiber surface studied by tapping mode atomic force microscopy. Surf Sci. 1993 Jun; 290(1-2):L688–92.

7. Hansma PK, Cleveland JP, Radmacher M, Walters DA, Hillner PE, Bezanilla M, et al. Tapping mode atomic force microscopy in liquids. Appl Phys Lett. AIP Publishing; 1994 Mar 28; 64(13):1738.

8. Cappella B, Dietler G. Force-distance curves by atomic force microscopy. Surf Sci Rep. 1999 Jan 34(1-3):1–104.

9. Butt H-J, Cappella B, Kappl M. Force measurements with the atomic force microscope: Technique, interpretation and applications. Surf Sci Rep. 2005 Oct; 59(1-6):1–152.

10. Seo Y, Jhe W. Atomic force microscopy and spectroscopy. Reports Prog Phys [Internet]. 2008 Jan; 71(1):016101.

11. Willemsen OH, Snel MM, van der Werf KO, de Grooth BG, Greve J, Hinterdorfer P, et al. Simultaneous height and adhesion imaging of antibody-antigen interactions by atomic force microscopy. Biophys J. 1998 Nov; 75(5):2220–8.

12. Raab A, Han W, Badt D, Smith-Gill SJ, Lindsay SM, Schindler H, et al. Antibody recognition imaging by force microscopy. Nat Biotechnol. Nature America Inc.; 1999 Sep; 17(9):901–5.

13. Lohr D, Wang H, Bash R, Lindsay SM. Recognition imaging of chromatin and chromatin-remodeling complexes in the atomic force microscope. Methods Mol Biol. 2009 Jan; 464:123–38.

14. Kaur P, Qiang-Fu, Fuhrmann A, Ros R, Kutner LO, Schneeweis LA, et al. Antibody-unfolding and metastable-state binding in force spectroscopy and recognition imaging. Biophys J. 2011 Jan; 100(1):243–50.

15. Paulsen J.R., Chromosomes and Chromatin, eLS, 2011. Available from:

http://www.els.net/WileyCDA/ElsArticle/refId-a0005766.html

16. Kalle W, Strappe P. Atomic force microscopy on chromosomes, chromatin and DNA: a review. Micron. 2012; 43(12):1224–31.

17. Cremer T, Cremer C. Chromosome territories, nuclear architecture and gene regulation in mammalian cells. Nat Rev Genet. 2001; 2(4):292–301.

18. Stower H. Gene regulation: from genetic variation to phenotype via chromatin. Nat Rev Genet. Nature Publishing Group, a division of Macmillan Publishers Limited. All Rights Reserved.; 2013; 14(12):824.

19. Schulze SR, Wallrath LL. Gene regulation by chromatin structure: paradigms established in Drosophila melanogaster. Annu Rev Entomol. Annual Reviews; 2007; 52:171–92.

20. Luger K, Mäder AW, Richmond RK, Sargent DF, Richmond TJ. Crystal structure of the nucleosome core particle at 2.8 A resolution. Nature. 1997; 389(6648):251–60.

21. Ramakrishnan V. HISTONE STRUCTURE AND THE ORGANIZATION OF THE NUCLEOSOME. Annu Rev Biophys Biomol Struct., 1997, 26, 83-112

22. Mariño-Ramírez L, Kann MG, Shoemaker BA, Landsman D. Histone structure and nucleosome stability. Expert Rev Proteomics. 2005; 2(5):719–29.

23. Redon C, Pilch D, Rogakou E, Sedelnikova O, Newrock K, Bonner W. Histone H2A variants H2AX and H2AZ. Curr Opin Genet Dev. 2002; 12(2):162–9.

24. Discovery of DNA Double Helix: Watson and Crick [Internet]. [cited 2015 Jan 8]. Available from: http://www.nature.com/scitable/topicpage/discovery-of-dna-structure-and-function-watson-397

25. Griffiths AJ, Gelbart WM, Miller JH, Lewontin RC. The Nature of DNA. W. H. Freeman; 1999. Available from: http://www.ncbi.nlm.nih.gov/books/NBK21261/

26. Bednar J, Horowitz RA, Grigoryev SA, Carruthers LM, Hansen JC, Koster AJ, et al. Nucleosomes, linker DNA, and linker histone form a unique structural motif that directs the higher-order folding and compaction of chromatin. Proc Natl Acad Sci. 1998; 95(24):14173–8.

27. An W, Leuba SH, van Holde K, Zlatanova J. Linker histone protects linker DNA on only one side of the core particle and in a sequence-dependent manner. Proc Natl Acad Sci U S A. 1998; 95(7):3396–401.

28. Felsenfeld G, Groudine M. Controlling the double helix. Nature. 2003; 421(6921):448–53.

29. Eissenberg J. C., Elgin S., Heterochromatin and Euchromatin, eLS, 2001.

30. Horvath JE, Bailey JA, Locke DP, Eichler EE. Lessons from the human genome: transitions between euchromatin and heterochromatin. Hum Mol Genet. 2001; 10(20):2215–23.

31. Tamaru H. Confining euchromatin/heterochromatin territory: jumonji crosses the line. Genes Dev. 2010; 24(14):1465–78.

32. Fussner E, Strauss M, Djuric U, Li R, Ahmed K, Hart M, et al. Open and closed domains in the mouse genome are configured as 10-nm chromatin fibres. EMBO Rep. 2012; 13(11):992–6.

33. Eltsov M, Maclellan KM, Maeshima K, Frangakis AS, Dubochet J. Analysis of cryo-electron microscopy images does not support the existence of 30-nm chromatin fibers in mitotic chromosomes in situ. Proc Natl Acad Sci U S A. 2008; 105(50):19732–7.

34. Joti Y, Hikima T, Nishino Y, Kamada F, Hihara S, Takata H, et al. Chromosomes without a 30-nm chromatin fiber. Nucleus. Taylor & Francis; 2012; 3(5):404–10.

35. Volle C, Dalal Y. Histone variants: the tricksters of the chromatin world. Curr Opin Genet Dev. 2014; 25:8–14,138.

36. Dawson MA, Kouzarides T. Cancer epigenetics: from mechanism to therapy. Cell. 2012; 150(1):12–27.

37. Rodríguez-Paredes M, Esteller M. Cancer epigenetics reaches mainstream oncology. Nat Med. Nature Publishing Group, a division of Macmillan Publishers Limited. All Rights Reserved.; 2011; 17(3):330–9.

38. Sharma S V, Settleman J. Oncogene addiction: setting the stage for molecularly targeted cancer therapy. Genes Dev. 2007; 21(24):3214–31.

39. Jones RG, Thompson CB. Tumor suppressors and cell metabolism: a recipe for cancer growth. Genes Dev. 2009; 23(5):537–48.

40. Rivlin N, Brosh R, Oren M, Rotter V. Mutations in the p53 Tumor Suppressor Gene: Important Milestones at the Various Steps of Tumorigenesis. Genes Cancer. 2011; 2(4):466–74.

41. Lund AH, van Lohuizen M. Epigenetics and cancer. Genes Dev. 2004; 18(19):2315–35.

42. Jones PA, Baylin SB. The fundamental role of epigenetic events in cancer. Nat Rev Genet. 2002; 3(6):415–28.

43. Baylin SB. DNA methylation and gene silencing in cancer. Nat Clin Pract Oncol. 2005; 2 Suppl 1:S4–11.

44. Kulis M, Esteller M. DNA methylation and cancer. Adv Genet. 2010; 70:27–56.

45. Witte T, Plass C, Gerhauser C. Pan-cancer patterns of DNA methylation. Genome Med. 2014; 6(8):66.

46. Archer SY, Hodin RA. Histone acetylation and cancer. Curr Opin Genet Dev. 1999; 9(2):171–4.

47. Cohen I, Poręba E, Kamieniarz K, Schneider R. Histone modifiers in cancer: friends or foes? Genes Cancer. 2011; 2(6):631–47.

48. Ropero S, Esteller M. The role of histone deacetylases (HDACs) in human cancer. Mol Oncol. 2007; 1(1):19–25.

49. Burgers WA, Fuks F, Kouzarides T. DNA methyltransferases get connected to chromatin. Trends Genet. Elsevier; 2002; 18(6):275–7.

50. Fuks F, Burgers WA, Brehm A, Hughes-Davies L, Kouzarides T. DNA methyltransferase Dnmt1 associates with histone deacetylase activity. Nat Genet. 2000; 24(1):88–91.

51. Quina AS, Buschbeck M, Di Croce L. Chromatin structure and epigenetics. Biochem Pharmacol. 2006 Nov 30; 72(11):1563–9.

52. Grunstein M. Histone acetylation in chromatin structure and transcription. Nature. Macmillan Magazines Ltd.; 1997; 389(6649):349–52.

53. Sato MH, Ura K, Hohmura KI, Tokumasu F, Yoshimura SH, Hanaoka F, et al. Atomic force microscopy sees nucleosome positioning and histone H1-induced compaction in reconstituted chromatin. FEBS Lett. 1999; 452(3):267–71.

54. Wang H, Bash R, Yodh JG, Hager GL, Lohr D, Lindsay SM. Glutaraldehyde modified mica: a new surface for atomic force microscopy of chromatin. Biophys J. 2002; 83(6):3619–25.

55. Lohr D, Bash R, Wang H, Yodh J, Lindsay S. Using atomic force microscopy to study chromatin structure and nucleosome remodeling. Methods. 2007; 41(3):333–41.

56. Padinhateeri R, Marko JF. Nucleosome positioning in a model of active chromatin remodeling enzymes. Proc Natl Acad Sci U S A. 2011; 108(19):7799–803.

57. Puntheeranurak T, Neundlinger I, Kinne RKH, Hinterdorfer P. Single-molecule recognition force spectroscopy of transmembrane transporters on living cells. Nat Protoc. Nature Publishing Group; 2011; 6(9):1443–52.

58. Lv Z, Roychaudhuri R, Condron MM, Teplow DB, Lyubchenko YL. Mechanism of amyloid β-protein dimerization determined using single-molecule AFM force spectroscopy. Sci Rep. Nature Publishing Group; 2013; 3:2880.

59. Ebner A, Kienberger F, Kada G, Stroh CM, Geretschläger M, Kamruzzahan ASM, et al. Localization of single avidin-biotin interactions using simultaneous topography and molecular recognition imaging. Chemphyschem. 2005; 6(5): 897–900.

60. You HX, Lau JM, Zhang S, Yu L. Atomic force microscopy imaging of living cells: a preliminary study of the disruptive effect of the cantilever tip on cell morphology. Ultramicroscopy. 2000; 82(1-4):297–305.

61. You HX, Yu L. Atomic force microscopy imaging of living cells: progress, problems and prospects. Methods Cell Sci. Kluwer Academic Publishers; 1999; 21(1):1–17.

62. Müller DJ, Dufrêne YF. Atomic force microscopy: a nanoscopic window on the cell surface. Trends Cell Biol. Elsevier; 2011; 21(8):461–9.

63. Chtcheglova LA, Wildling L, Waschke J, Drenckhahn D, Hinterdorfer P. AFM functional imaging on vascular endothelial cells. J Mol Recognit. 2010; 23(6):589–96.

64. Wang H, Dalal Y, Henikoff S, Lindsay S. Single-epitope recognition imaging of native chromatin. Epigenetics Chromatin. 2008; 1(1):10.

65. Anderson NL, Anderson NG. The human plasma proteome: history, character, and diagnostic prospects. Mol Cell Proteomics. 2002; 1(11):845–67.

66. Archakov AI, Ivanov YD. Analytical nanobiotechnology for medicine diagnostics. Mol Biosyst. 2007; 3(5):336–42.

67. Archakov AI, Ivanov YD, Lisitsa AV, Zgoda VG. AFM fishing nanotechnology is the way to reverse the Avogadro number in proteomics. Proteomics. 2007; 7(1):4–9.

68. Florin E, Moy V, Gaub H. Adhesion forces between individual ligand-receptor pairs. Science. 1994; 264(5157): 415–7.

69. Lin L, Wang H, Liu Y, Yan H, Lindsay S. Recognition imaging with a DNA aptamer. Biophys J. 2006; 90(11):4236–8.

70. Bizzarri AR, Cannistraro S. The application of atomic force spectroscopy to the study of biological complexes undergoing a biorecognition process. Chem Soc Rev. 2010; 39(2):734–49.

71. Hinterdorfer P, Kienberger F, Raab A, Gruber HJ, Baumgartner W, Kada G, et al. Poly(Ethylene Glycol): An Ideal Spacer for Molecular Recognition Force Microscopy/Spectroscopy. Single Mol. 2000; 1(2):99–103.

72. Limansky AP, Shlyakhtenko LS, Schaus S, Henderson E, Lyubchenko YL. Aminomodified Probes for Atomic Force Microscopy. Probe Microsc. Taylor and Francis Ltd; 2002; 2(3-4):227–34.

73. Ebner A, Hinterdorfer P, Gruber HJ. Comparison of different aminofunctionalization strategies for attachment of single antibodies to AFM cantilevers. Ultramicroscopy. 2007; 107(10-11):922–7.

74. Vandenberg ET, Bertilsson L, Liedberg B, Uvdal K, Erlandsson R, Elwing H, et al. Structure of 3-aminopropyl triethoxy silane on silicon oxide. J Colloid Interface Sci. 1991; 147(1):103–18.

75. Guha Thakurta S, Subramanian A. Fabrication of dense, uniform aminosilane monolayers: A platform for protein or ligand immobilization. Colloids Surfaces A Physicochem Eng Asp. 2012; 414:384–92.

76. Riener CK, Kienberger F, Hahn CD, Buchinger GM, Egwim IOC, Haselgrübler T, et al. Heterobifunctional crosslinkers for tethering single ligand molecules to scanning probes. Anal Chim Acta. 2003; 497(1-2):101–14.

77. Ebner A, Wildling L, Kamruzzahan ASM, Rankl C, Wruss J, Hahn CD, et al. A new, simple method for linking of antibodies to atomic force microscopy tips. Bioconjug Chem. 2007; 18(4):1176–84.

78. Limanskii AP. Functionalization of amino-modified probes for atomic force microscopy. Biophysics (Oxf). 2006; 51(2):186–95.

79. Cuatrecasas P, Parikh I. Adsorbents for affinity chromatography. Use of N-hydroxysuccinimide esters of agarose. Biochemistry. 1972; 11(12):2291–9.

80. Chen G, Ning X, Park B, Boons G-J, Xu B. Simple, clickable protocol for atomic force microscopy tip modification and its application for trace ricin detection by recognition imaging. Langmuir. 2009; 25(5):2860–4.

81. Lyubchenko YL, Shlyakhtenko LS, Ando T. Imaging of nucleic acids with atomic force microscopy. Methods. 2011; 54(2):274–83.

82. Riener CK, Stroh CM, Ebner A, Klampfl C, Gall AA, Romanin C, et al. Simple test system for single molecule recognition force microscopy. Anal Chim Acta. 2003; 479(1):59–75.

83. Shlyakhtenko LS, Gall AA, Filonov A, Cerovac Z, Lushnikov A, Lyubchenko YL. Silatrane-based surface chemistry for immobilization of DNA, protein-DNA complexes and other biological materials. 2003; Ultramicroscopy. ; 97(1-4):279–87.

84. Lyubchenko YL, Shlyakhtenko LS, Gall AA. Atomic force microscopy imaging and probing of DNA, proteins, and protein DNA complexes: silatrane surface chemistry. Methods Mol Biol. 2009; 543:337–51.

85. Agard NJ, Baskin JM, Prescher JA, Lo A, Bertozzi CR. A Comparative Study of Bioorthogonal Reactions with Azides. ACS Chem Biol. 2006; 1(10):644–8.

86. Mascini M, Palchetti I, Tombelli S. Nucleic acid and peptide aptamers: fundamentals and bioanalytical aspects. Angew Chem Int Ed Engl. 2012; 51(6):1316–32.

87. Nimmo CM, Shoichet MS. Regenerative biomaterials that “click”: simple, aqueous-based protocols for hydrogel synthesis, surface immobilization, and 3D patterning. Bioconjug Chem. 2011; 22(11):2199–209.

88. Morales-Sanfrutos J, Lopez-Jaramillo J, Ortega-Muñoz M, Megia-Fernandez A, Perez-Balderas F, Hernandez-Mateo F, et al. Vinyl sulfone: a versatile function for simple bioconjugation and immobilization. Org Biomol Chem. 2010; 8(3):667–75.

89. F. Javier Lopez-Jaramillo FH-M and FS-G. Integrative Proteomics. Leung H-C, editor. InTech; 2012, 301-326

90. Loiseau FA, Hii KK, Hill AM. Multigram synthesis of well-defined extended bifunctional polyethylene glycol (PEG) chains. J Org Chem. 2004; 69(3):639–47.

91. Svedhem S, Hollander C-Å, Shi J, Konradsson P, Liedberg B, Svensson SCT. Synthesis of a Series of Oligo(ethylene glycol)-Terminated Alkanethiol Amides Designed to Address Structure and Stability of Biosensing Interfaces. J Org Chem. 2001; 66(13):4494–503.

92. Huang Z, Wang R, Sheng S, Zhou R, Cai M. Preparation of polystyrene-supported vinyl sulfone and its application in the solid-phase organic synthesis of 1-monosubstituted 1,2,3-triazoles. React Funct Polym. 2013; 73(1):224–7.

93. Stenzel MH. Bioconjugation Using Thiols: Old Chemistry Rediscovered to Connect Polymers with Nature's Building Blocks. ACS Macro Lett. 2013; 2(1):14–8.

94. Sinclair AJ, del Amo V, Philp D. Structure-reactivity relationships in a recognition mediated [3+2] dipolar cycloaddition reaction. Org Biomol Chem. 2009; 7(16):3308–18.

95. Alley SC, Benjamin DR, Jeffrey SC, Okeley NM, Meyer DL, Sanderson RJ, et al. Contribution of linker stability to the activities of anticancer immunoconjugates. Bioconjug Chem. 2008; 19(3):759–65.

96. Lin D, Saleh S, Liebler DC. Reversibility of covalent electrophile-protein adducts and chemical toxicity. Chem Res Toxicol. 2008; 21(12):2361–9.

97. Bock LC, Griffin LC, Latham JA, Vermaas EH, Toole JJ. Selection of single-stranded DNA molecules that bind and inhibit human thrombin. Nature. 1992; 355(6360):564–6.

98. Ruoslahti E. RGD and other recognition sequences for integrins. Annu Rev Cell Dev Biol. 1996; 12:697–715.

99. Schelté, P, Boeckler C, Frisch B, Schuber F. Differential Reactivity of Maleimide and Bromoacetyl Functions with Thiols: Application to the Preparation of Liposomal Diepitope Constructs. Bioconjug Chem. 2000; 11(1):118–23.

100. Li L, Tsai S-W, Anderson A-L, Keire DA, Raubitschek AA, Shively JE. Vinyl sulfone bifunctional derivatives of DOTA allow sulfhydryl- or amino-directed coupling to antibodies. Conjugates retain immunoreactivity and have similar biodistributions. Bioconjug Chem. 2002; 13(1):110–5.

101. Zeng X, Xu G, Gao Y, An Y. Surface wettability of (3-aminopropyl)triethoxysilane self-assembled monolayers. J Phys Chem B. 2011; 115(3):450–4.

102. Agard NJ, Prescher JA, Bertozzi CR. A strain-promoted [3 + 2] azide-alkyne cycloaddition for covalent modification of biomolecules in living systems. J Am Chem Soc. 2004; 126(46):15046–7.

103. Lee C-K, Wang Y-M, Huang L-S, Lin S. Atomic force microscopy: determination of unbinding force, off rate and energy barrier for protein-ligand interaction. Micron. 2007; 38(5):446–61.

104. Ge L, Jin G, Fang X. Investigation of the interaction between a bivalent aptamer and thrombin by AFM. Langmuir. 2012; 28(1):707–13.

105. Lehenkari PP, Horton MA. Single integrin molecule adhesion forces in intact cells measured by atomic force microscopy. Biochem Biophys Res Commun. 1999; 259(3):645–50.

106. Müller DJ, Dufrêne YF. Atomic force microscopy as a multifunctional molecular toolbox in nanobiotechnology. Nat Nanotechnol. 2008; 3(5):261–9.

107. Engel A, Müller DJ. Observing single biomolecules at work with the atomic force microscope. Nat Struct Biol. 2000; 7(9):715–8.

108. Alsteens D, Dupres V, Yunus S, Latgé J-P, Heinisch JJ, Dufrêne YF. High-resolution imaging of chemical and biological sites on living cells using peak force tapping atomic force microscopy. Langmuir. 2012; 28(49):16738–44.

109. Rudnev A V., Malinovskii VL, Nussbaumer AL, Mishchenko A, Häner R, Wandlowski T. Cooperative and Noncooperative Assembly of Oligopyrenotides Resolved by Atomic Force Microscopy. Macromolecules. 2012; 45(15):5986–92.

110. Zhang J, Chen P, Yuan B, Ji W, Cheng Z, Qiu X. Real-space identification of intermolecular bonding with atomic force microscopy. Science. 2013; 342(6158):611–4.

111. Embrechts A, Schönherr H, Vancso GJ. Rupture force of single supramolecular bonds in associative polymers by AFM at fixed loading rates. J Phys Chem B. 2008; 112(25):7359–62.

112. Sikora AE, Smith JR, Campbell SA, Firman K. AFM protein–protein interactions within the EcoR124I molecular motor. Soft Matter. 2012; 8(23):6358.

113. Sorci M, Dassa B, Liu H, Anand G, Dutta AK, Pietrokovski S, et al. Oriented covalent immobilization of antibodies for measurement of intermolecular binding forces between zipper-like contact surfaces of split inteins. Anal Chem. 2013; 85(12):6080–8.

114. Ritzefeld M, Walhorn V, Anselmetti D, Sewald N. Analysis of DNA interactions using single-molecule force spectroscopy. Amino Acids. 2013; 44(6):1457–75.

115. Florin EL, Moy VT, Gaub HE. Adhesion forces between individual ligand-receptor pairs. Science. 1994; 264(5157):415–7.

116. Thormann E, Simonsen AC, Nielsen LK, Mouritsen OG. Ligand-receptor interactions and membrane structure investigated by AFM and time-resolved fluorescence microscopy. J Mol Recognit. 2007; 20(6):554–60.

117. Ando T, Uchihashi T, Kodera N. High-speed AFM and applications to biomolecular systems. Annu Rev Biophys. 2013; 42:393–414.

118. Preiner J, Kodera N, Tang J, Ebner A, Brameshuber M, Blaas D, et al. IgGs are made for walking on bacterial and viral surfaces. Nat Commun. 2014; 5:4394.

119. Dufrêne YF. Atomic force microscopy: a powerful molecular toolkit in nanoproteomics. Proteomics. 2009; 9(24):5400–5.

120. Lekka M. Atomic force microscopy: A tip for diagnosing cancer. Nat Nanotechnol [Internet]. Nature Publishing Group, a division of Macmillan Publishers Limited. 2012; 7(11):691–2.

121. Zhu R, Howorka S, Pröll J, Kienberger F, Preiner J, Hesse J, et al. Nanomechanical recognition measurements of individual DNA molecules reveal epigenetic methylation patterns. Nat Nanotechnol. 2010; 5(11):788–91.

122. Gökmen-Polar Y, Badve S. Multiplexed protein analysis. Sci Transl Med. 2014; 6(219):219fs3.

123. Wang H, Bash R, Lohr D. Two-component atomic force microscopy recognition imaging of complex samples. Anal Biochem. 2007; 361(2):273–9.

124. Beal DM, Jones LH. Molecular scaffolds using multiple orthogonal conjugations: applications in chemical biology and drug discovery. Angew Chem Int Ed Engl. 2012; 51(26):6320–6.

125. Viault G, Dautrey S, Maindron N, Hardouin J, Renard P-Y, Romieu A. The first “ready-to-use” benzene-based heterotrifunctional cross-linker for multiple bioconjugation. Org Biomol Chem. 2013; 11(16):2693–705.

126. Chinchilla R, Najera C. The Sonogashira reaction: a booming methodology in synthetic organic chemistry. Chem Rev. 2007; 107(3):874–922.

127. Kienberger F, Ebner A, Gruber HJ, Hinterdorfer P. Molecular recognition imaging and force spectroscopy of single biomolecules. Acc Chem Res. 2006; 39(1):29–36.

128. Martinez-Veracoechea FJ, Leunissen ME. The entropic impact of tethering, multivalency and dynamic recruitment in systems with specific binding groups. Soft Matter. 2013; 9(12):3213.

129. Mas-Moruno C, Rechenmacher F, Kessler H. Cilengitide: the first anti-angiogenic small molecule drug candidate design, synthesis and clinical evaluation. Anticancer Agents Med Chem. 2010; 10(10):753–68.

130. Berezovski M, Nutiu R, Li Y, Krylov SN. Affinity Analysis of a Protein−Aptamer Complex Using Nonequilibrium Capillary Electrophoresis of Equilibrium Mixtures. Anal Chem. 2003; 75(6):1382–6.

131. Bochen A, Marelli UK, Otto E, Pallarola D, Mas-Moruno C, Di Leva FS, et al. Biselectivity of isoDGR peptides for fibronectin binding integrin subtypes α5β1 and αvβ6: conformational control through flanking amino acids. J Med Chem. 2013; 56(4):1509–19.

132. Senapati S, Manna S, Lindsay S, Zhang P. Application of catalyst-free click reactions in attaching affinity molecules to tips of atomic force microscopy for detection of protein biomarkers. Langmuir. 2013; 29(47):14622–30.

133. Debets MF, van Berkel SS, Schoffelen S, Rutjes FPJT, van Hest JCM, van Delft FL. Aza-dibenzocyclooctynes for fast and efficient enzyme PEGylation via copper-free (3+2) cycloaddition. Chem Comm. 2010; 46(1):97–9.

134. Kuzmin A, Poloukhtine A, Wolfert MA, Popik V V. Surface functionalization using catalyst-free azide-alkyne cycloaddition. Bioconjug Chem. 2010; 21(11):2076–85.

135. Lee JK, Jung YH, Tok JB-H, Bao Z. Syntheses of organic molecule-DNA hybrid structures. ACS Nano. 2011; 5(3):2067–74.

136. Xiong H, Leonard P, Seela F. Construction and assembly of branched Y-shaped DNA: “click” chemistry performed on dendronized 8-aza-7-deazaguanine oligonucleotides. Bioconjug Chem. 2012; 23(4):856–70.

137. Prensner JR, Rubin MA, Wei JT, Chinnaiyan AM. Beyond PSA: the next generation of prostate cancer biomarkers. Sci Transl Med. 2012; 4(127):127rv3.

138. Kort SAR, Martens F, Vanpoucke H, van Duijnhoven HL, Blankenstein MA. Comparison of 6 automated assays for total and free prostate-specific antigen with special reference to their reactivity toward the WHO 96/670 reference preparation. Clin Chem. 2006; 52(8):1568–74.

139. Luk E, Ranjan A, Fitzgerald PC, Mizuguchi G, Huang Y, Wei D, et al. Stepwise histone replacement by SWR1 requires dual activation with histone H2A.Z and canonical nucleosome. Cell. 2010; 143(5):725–36.

140. Robertson KD. DNA methylation and human disease. Nat Rev Genet. 2005; 6(8):597–610.

141. Widom J. Role of DNA sequence in nucleosome stability and dynamics. Q Rev Biophys. 2002; 34(03):269–324.

142. Guidotti A, Dong E, Kundakovic M, Satta R, Grayson DR, Costa E. Characterization of the action of antipsychotic subtypes on valproate-induced chromatin remodeling. Trends Pharmacol Sc; 2009; 30(2):55-60.

143. Hansen JC, van Holde KE, Lohr D. The mechanism of nucleosome assembly onto oligomers of the sea urchin 5 S DNA positioning sequence. J Biol Chem. 1991; 266(7):4276–82.

144. Orlando V. Mapping chromosomal proteins in vivo by formaldehyde-crosslinked-chromatin immunoprecipitation. Trends Biochem Sci. 2000; 25(3):99–104.

145. O'Neill LP, Turner BM. Immunoprecipitation of native chromatin: NChIP. Methods. 2003; 31(1):76–82.

146. Yuan G-C, Liu Y-J, Dion MF, Slack MD, Wu LF, Altschuler SJ, et al. Genome-scale identification of nucleosome positions in S. cerevisiae. Science. 2005; 309(5734):626–30.

147. Sabo PJ, Kuehn MS, Thurman R, Johnson BE, Johnson EM, Cao H, et al. Genome-scale mapping of DNase I sensitivity in vivo using tiling DNA microarrays. Nat Methods. 2006; 3(7):511–8.

148. Sanders MM. Fractionation of nucleosomes by salt elution from micrococcal nuclease-digested nuclei. J Cell Biol. 1978; 79(1):97–109.

149. Henikoff S, Henikoff JG, Sakai A, Loeb GB, Ahmad K. Genome-wide profiling of salt fractions maps physical properties of chromatin. Genome Res. 2009; 19(3):460–9.

150. Teves SS, Henikoff S. Salt fractionation of nucleosomes for genome-wide profiling. Methods Mol Biol. 2012; 833:421–32.

151. Dimitriadis EK, Weber C, Gill RK, Diekmann S, Dalal Y. Tetrameric organization of vertebrate centromeric nucleosomes. Proc Natl Acad Sci U S A. 2010; 107(47):20317–22.

152. Stroh C, Wang H, Bash R, Ashcroft B, Nelson J, Gruber H, et al. Single-molecule recognition imaging microscopy. Proc Natl Acad Sci U S A. 2004; 101(34):12503–7.

153. Bash R, Wang H, Anderson C, Yodh J, Hager G, Lindsay SM, et al. AFM imaging of protein movements: histone H2A-H2B release during nucleosome remodeling. FEBS Lett. 2006; 580(19):4757–61.

154. Lin L, Fu Q, Williams BAR, Azzaz AM, Shogren-Knaak MA, Chaput JC, et al. Recognition imaging of acetylated chromatin using a DNA aptamer. Biophys J. 2009; 97(6):1804–7.

155. Laitinen J, Sistonen L, Alitalo K, Holtta E, c-Ha-rasVal 12 oncogene-transformed NIH-3T3 fibroblasts display more decondensed nucleosomal organization than normal fibroblasts. J Cell Biol. 1990; 111(1):9–17.

APPENDIX A

COPYRIGHT PERMISSIONS

Order Completed

Thank you very much for your order.

This is a License Agreement between Subhadip Senapati ("You") and Nature Publishing Group ("Nature Publishing Group"). The license consists of your order details, the terms and conditions provided by Nature Publishing Group, and the payment terms and conditions.

Get the printable license.

License Number	3545280477373
License date	Jan 10, 2015
Licensed content publisher	Nature Publishing Group
Licensed content publication	Nature
Licensed content title	Crystal structure of the nucleosome core particle at 2.8|[thinsp]||[Aring]| resolution
Licensed content author	Karolin Luger,Armin W. Mäder,Robin K. Richmond,David F. SargentandTimothy J. Richmond
Licensed content date	Sep 18, 1997
Type of Use	reuse in a dissertation / thesis
Volume number	389
Issue number	6648
Requestor type	academic/educational
Format	print and electronic
Portion	figures/tables/illustrations
Number of figures/tables/illustrations	1
Figures	Figure 1. Nucleosome core particle
Author of this NPG article	no
Your reference number	None
Title of your thesis / dissertation	Studying Biomolecular Structure and Their Interaction Using Atomic Force Microscopy
Expected completion date	Jan 2015
Estimated size (number of pages)	150
Total	0.00 USD

Using cardboard cutouts representing the individual chemical components of the four bases and other nucleotide subunits, Watson and Crick shifted molecules around on their desktops, as though putting together a puzzle. They were misled for a while by an erroneous understanding of how th , the carbon, nitrogen, hydrogen, and oxygen rings) were configured. Only u did Watson decide to make new cardboard cutouts of the two bases, to see if perh ence. It did. Not only did the complementary bases now fit together perfectly (i.e hydrogen bonds, but the structure also reflected Chargaff's rule (Figure 3

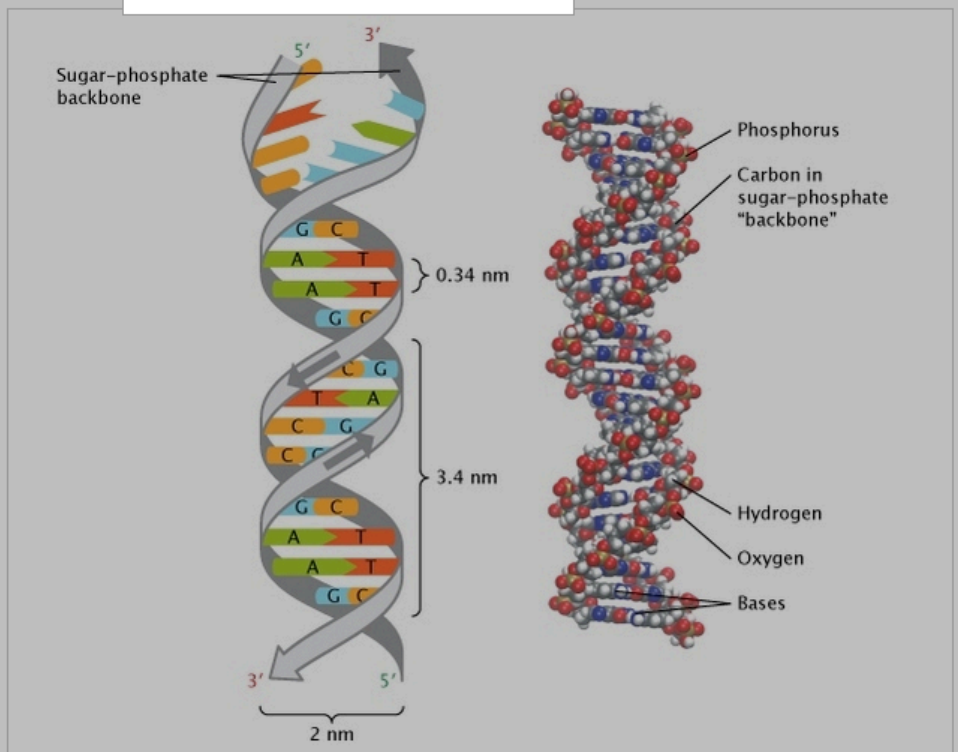

Order Completed

Thank you very much for your order.

This is a License Agreement between Subhadip Senapati ("You") and Nature Publishing Group ("Nature Publishing Group"). The license consists of your order details, the terms and conditions provided by Nature Publishing Group, and the payment terms and conditions.

Get the printable license.

License Number	3547290545139
License date	Jan 13, 2015
Licensed content publisher	Nature Publishing Group
Licensed content publication	Nature
Licensed content title	Controlling the double helix
Licensed content author	Gary Felsenfeld and Mark Groudine
Licensed content date	Jan 23, 2003
Type of Use	reuse in a dissertation / thesis
Volume number	421
Issue number	6921
Requestor type	academic/educational
Format	print and electronic
Portion	figures/tables/illustrations
Number of figures/tables/illustrations	1
High-res required	no
Figures	chromosome dimension
Author of this NPG article	no
Your reference number	None
Title of your thesis / dissertation	Studying Biomolecular Structure and Their Interaction Using Atomic Force Microscopy
Expected completion date	Jan 2015
Estimated size (number of pages)	150
Total	0.00 USD

ORDER MORE... CLOSE WINDOW

Copyright Clearance Center RightsLink®

Home | Account Info | Help | Live Chat

Title: Histone variants: the tricksters of the chromatin world
Publication: Current Opinion in Genetics & Development
Publisher: Elsevier
Date: April 2014
Published by Elsevier Ltd.

Logged in as:
Subhadip Senapati
Account #:
3000877584
LOGOUT

Order Completed

Thank you very much for your order.

This is a License Agreement between Subhadip Senapati ("You") and Elsevier ("Elsevier"). The license consists of your order details, the terms and conditions provided by Elsevier, and the payment terms and conditions.

Get the printable license.

License Number	3547290782950
License date	Jan 13, 2015
Licensed content publisher	Elsevier
Licensed content publication	Current Opinion in Genetics & Development
Licensed content title	Histone variants: the tricksters of the chromatin world
Licensed content author	None
Licensed content date	April 2014
Licensed content volume number	25
Licensed content issue number	n/a
Number of pages	7
Type of Use	reuse in a thesis/dissertation
Portion	figures/tables/illustrations
Number of figures/tables/illustrations	1
Format	both print and electronic
Are you the author of this Elsevier article?	No
Will you be translating?	No
Original figure numbers	figure 1
Title of your thesis/dissertation	Studying Biomolecular Structure and Their Interaction Using Atomic Force Microscopy
Expected completion date	Jan 2015
Estimated size (number of pages)	150
Elsevier VAT number	GB 494 6272 12
Permissions price	0.00 USD
VAT/Local Sales Tax	0.00 USD / 0.00 GBP
Total	0.00 USD

Order Completed

Thank you very much for your order.

This is a License Agreement between Subhadip Senapati ("You") and Nature Publishing Group ("Nature Publishing Group"). The license consists of your order details, the terms and conditions provided by Nature Publishing Group, and the payment terms and conditions.

Get the printable license.

License Number	3562891411696
License date	Feb 06, 2015
Licensed content publisher	Nature Publishing Group
Licensed content publication	Nature Clinical Practice Oncology
Licensed content title	DNA methylation and gene silencing in cancer
Licensed content author	Stephen B Baylin
Licensed content date	Dec 1, 2005
Type of Use	reuse in a dissertation / thesis
Volume number	2
Issue number	0
Requestor type	academic/educational
Format	print and electronic
Portion	figures/tables/illustrations
Number of figures/tables/illustrations	1
High-res required	no
Figures	Figure 2
Author of this NPG article	no
Your reference number	None
Title of your thesis / dissertation	Studying Biomolecular Structure and Their Interaction Using Atomic Force Microscopy
Expected completion date	Feb 2015
Estimated size (number of pages)	150
Total	0.00 USD

ORDER MORE... CLOSE WINDOW

Clearance Center RightsLink

Home | Account Info | Help | Live Chat

Title: DNA methyltransferases get connected to chromatin
Author: Wendy A Burgers,François Fuks,Tony Kouzarides
Publication: Trends in Genetics
Publisher: Elsevier
Date: 1 June 2002

Logged in as:
Subhadip Senapati
Account #:
3000877584
LOGOUT

Order Completed

Thank you very much for your order.

This is a License Agreement between Subhadip Senapati ("You") and Elsevier ("Elsevier"). The license consists of your order details, the terms and conditions provided by Elsevier, and the payment terms and conditions.

Get the printable license.

License Number	3547291109367
License date	Jan 13, 2015
Licensed content publisher	Elsevier
Licensed content publication	Trends in Genetics
Licensed content title	DNA methyltransferases get connected to chromatin
Licensed content author	Wendy A Burgers,François Fuks,Tony Kouzarides
Licensed content date	1 June 2002
Licensed content volume number	18
Licensed content issue number	6
Number of pages	3
Type of Use	reuse in a thesis/dissertation
Portion	figures/tables/illustrations
Number of figures/tables/illustrations	1
Format	both print and electronic
Are you the author of this Elsevier article?	No
Will you be translating?	No
Original figure numbers	HDAC DNMT
Title of your thesis/dissertation	Studying Biomolecular Structure and Their Interaction Using Atomic Force Microscopy
Expected completion date	Jan 2015
Estimated size (number of pages)	150
Elsevier VAT number	GB 494 6272 12
Permissions price	0.00 USD
VAT/Local Sales Tax	0.00 USD / 0.00 GBP
Total	0.00 USD

ORDER MORE... CLOSE WINDOW

Title:	Single-molecule recognition force spectroscopy of transmembrane transporters on living cells
Author:	Theeraporn Puntheeranurak, Isabel Neundlinger, Rolf K H Kinne, Peter Hinterdorfer
Publication:	Nature Protocols
Publisher:	Nature Publishing Group
Date:	Sep 1, 2011

Logged in as:
Subhadip Senapati
Account #:
3000877584

LOGOUT

Order Completed

Thank you very much for your order.

This is a License Agreement between Subhadip Senapati ("You") and Nature Publishing Group ("Nature Publishing Group"). The license consists of your order details, the terms and conditions provided by Nature Publishing Group, and the payment terms and conditions.

Get the printable license.

License Number	3562900333776
License date	Feb 06, 2015
Licensed content publisher	Nature Publishing Group
Licensed content publication	Nature Protocols
Licensed content title	Single-molecule recognition force spectroscopy of transmembrane transporters on living cells
Licensed content author	Theeraporn Puntheeranurak, Isabel Neundlinger, Rolf K H Kinne, Peter Hinterdorfer
Licensed content date	Sep 1, 2011
Type of Use	reuse in a dissertation / thesis
Volume number	6
Issue number	9
Requestor type	academic/educational
Format	print and electronic
Portion	figures/tables/illustrations
Number of figures/tables/illustrations	1
High-res required	no
Figures	Figure 1
Author of this NPG article	no
Your reference number	None
Title of your thesis / dissertation	Studying Biomolecular Structure and Their Interaction Using Atomic Force Microscopy
Expected completion date	Feb 2015
Estimated size (number of pages)	150
Total	0.00 USD

ORDER MORE... CLOSE WINDOW

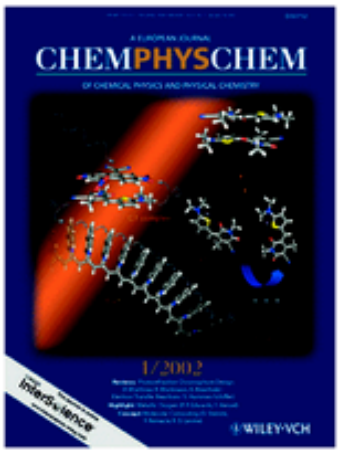

Title: Localization of Single Avidin–Biotin Interactions Using Simultaneous Topography and Molecular Recognition Imaging

Author: Andreas Ebner,Ferry Kienberger,Gerald Kada,Cordula M. Stroh,Manfred Geretschläger,A. S. M. Kamruzzahan,Linda Wildling,W. Travis Johnson,Brian Ashcroft,Jeremy Nelson,Stuart M. Lindsay,Hermann J. Gruber,Peter Hinterdorfer

Publication: ChemPhysChem

Publisher: John Wiley and Sons

Date: Apr 22, 2005

Order Completed

Thank you for your order.

This Agreement between Subhadip Senapati ("You") and John Wiley and Sons ("John Wiley and Sons") consists of your license details and the terms and conditions provided by John Wiley and Sons and Copyright Clearance Center.

Your confirmation email will contain your order number for future reference.

Get the printable license.

License Number	3562900903656
License date	Feb 06, 2015
Licensed Content Publisher	John Wiley and Sons
Licensed Content Publication	ChemPhysChem
Licensed Content Title	Localization of Single Avidin–Biotin Interactions Using Simultaneous Topography and Molecular Recognition Imaging
Licensed Content Author	Andreas Ebner,Ferry Kienberger,Gerald Kada,Cordula M. Stroh,Manfred Geretschläger,A. S. M. Kamruzzahan,Linda Wildling,W. Travis Johnson,Brian Ashcroft,Jeremy Nelson,Stuart M. Lindsay,Hermann J. Gruber,Peter Hinterdorfer
Licensed Content Date	Apr 22, 2005

Licensed Content Pages	4
Type of use	Dissertation/Thesis
Requestor type	University/Academic
Format	Print and electronic
Portion	Figure/table
Number of figures/tables	1
Original Wiley figure/table number(s)	Figure 2
Will you be translating?	No
Title of your thesis / dissertation	Studying Biomolecular Structure and Their Interaction Using Atomic Force Microscopy
Expected completion date	Feb 2015
Expected size (number of pages)	150
Requestor Location	Subhadip Senapati 1023 E University Dr, Apt 303 TEMPE, AZ 85281 United States Attn: Subhadip Senapati
Billing Type	Invoice
Billing address	Subhadip Senapati 1023 E University Dr, Apt 303 TEMPE, AZ 85281 United States Attn: Subhadip Senapati
Total	0.00 USD

ORDER MORE CLOSE WINDOW

Copyright Clearance Center RightsLink®

Home | Account Info | Help | Live Ch

Title: Two-component atomic force microscopy recognition imaging of complex samples
Publication: Analytical Biochemistry
Publisher: Elsevier
Date: 15 February 2007

Logged in as:
Subhadip Senapati
Account #:
3000877584
LOGOUT

Order Completed

Thank you very much for your order.

This is a License Agreement between Subhadip Senapati ("You") and Elsevier ("Elsevier"). The license consists of your order details, the terms and conditions provided by Elsevier, and the payment terms and conditions.

Get the printable license.

License Number	3562910069578
License date	Feb 06, 2015
Licensed content publisher	Elsevier
Licensed content publication	Analytical Biochemistry
Licensed content title	Two-component atomic force microscopy recognition imaging of complex samples
Licensed content author	None
Licensed content date	15 February 2007
Licensed content volume number	361
Licensed content issue number	2
Number of pages	7
Type of Use	reuse in a thesis/dissertation
Portion	figures/tables/illustrations
Number of figures/tables/illustrations	2
Format	both print and electronic
Are you the author of this Elsevier article?	No
Will you be translating?	No
Original figure numbers	Figure 1 and 2
Title of your thesis/dissertation	Studying Biomolecular Structure and Their Interaction Using Atomic Force Microscopy
Expected completion date	Feb 2015
Estimated size (number of pages)	150
Elsevier VAT number	GB 494 6272 12
Permissions price	0.00 USD
VAT/Local Sales Tax	0.00 USD / 0.00 GBP
Total	0.00 USD

ORDER MORE... CLOSE WINDOW

Title: Characterization of the action of antipsychotic subtypes on valproate-induced chromatin remodeling

Author: Alessandro Guidotti,Erbo Dong,Marija Kundakovic,Rosalba Satta,Dennis R. Grayson,Erminio Costa

Publication: Trends in Pharmacological Sciences

Publisher: Elsevier

Date: February 2009

Logged in as:
Subhadip Senapati
Account #:
3000877584

LOGOUT

Order Completed

Thank you very much for your order.

This is a License Agreement between Subhadip Senapati ("You") and Elsevier ("Elsevier"). The license consists of your order details, the terms and conditions provided by Elsevier, and the payment terms and conditions.

Get the printable license.

License Number	3562921245718
License date	Feb 06, 2015
Licensed content publisher	Elsevier
Licensed content publication	Trends in Pharmacological Sciences
Licensed content title	Characterization of the action of antipsychotic subtypes on valproate-induced chromatin remodeling
Licensed content author	Alessandro Guidotti,Erbo Dong,Marija Kundakovic,Rosalba Satta,Dennis R. Grayson,Erminio Costa
Licensed content date	February 2009
Licensed content volume number	30
Licensed content issue number	2
Number of pages	6
Type of Use	reuse in a thesis/dissertation
Portion	figures/tables/illustrations
Number of figures/tables/illustrations	1
Format	both print and electronic
Are you the author of this Elsevier article?	No
Will you be translating?	No
Original figure numbers	figure 1
Title of your thesis/dissertation	Studying Biomolecular Structure and Their Interaction Using Atomic Force Microscopy
Expected completion date	Feb 2015
Estimated size (number of pages)	150
Elsevier VAT number	GB 494 6272 12